Measurements of Gamow-Teller Strength in Medium Mass Nuclei Using (p,n) Reactions at Intermediate Energies.

Douw Steyn

A thesis presented to the Faculty of Science
of the University of Cape Town
for the degree of
Doctor of Philosophy
in Physics

February 1997

Abstract

Charge exchange (p,n) reactions have been performed at the NAC cyclotron at beam energies of E_p = 90, 120, 160, and 200 MeV using time-of-flight (TOF) methods to measure the energies of the ejected neutrons. A stack of six neutron detectors with intrinsic time resolutions of less than 500 ps and flight path lengths of 150 m to 174 m were employed to produce energy resolutions (FWHM) of the order of 300 keV at E_p = 120 MeV and 700 keV at E_p = 200 MeV. Zero degree measurements were made for targets of ^{51}V, ^{54}Fe, and ^{59}Co at all energies, and angular distributions over the limited range of $0° \leq \theta \leq 4°$ were measured at some of these energies. Cross sections were normalised to the known yields for Lithium. All visible structures in the discrete parts of the spectra were examined and Gamow-Teller strengths were obtained for these states. Estimates of GT strengths have also been made for the background regions beneath the GT resonances. Summed strengths up to approximately 15 MeV excitation energy were compared with the predictions of the model-independent sum rule. This represents an addition to currently published data of the 90, 120 and 200 MeV points for ^{51}V, the 90 and 200 MeV points for ^{54}Fe, and the 120, 160 and 200 MeV points for ^{59}Co. The 160 MeV point for ^{51}V represents a significant improvement in resolution to that of published data and the extraction of many discrete states in addition to the ground state and isobaric analog state (IAS) previously studied. The 90 MeV point for ^{59}Co includes an analysis of the whole spectrum up to 20 MeV excitation as well as the IAS previously examined. Comparisons of the results with published calculations have also been made.

GT strengths are a function of nuclear structure and should, therefore, be independent of the incident projectile energy. However, the GT strengths extracted in this work exhibit an apparent energy dependence. This is not expected and is not fully understood. The few previously published points agree with the results obtained here at the higher beam energies, especially at E_p = 160 MeV. It is suspected that some of the approximations used in deriving the strengths from the extracted cross sections may not be valid at the lower beam energies, although the cross sections themselves appear to be unexpectedly small at the lower beam energies. For the ^{51}V and ^{54}Fe targets the maximum strengths, which are obtained at the highest beam energies, are sufficient to account for the minimum strengths predicted by the GT sum rule. For ^{59}Co over 90% of the expected minimum is observed at E_p = 200 MeV. Inclusion of previously measured β^+ strengths from the literature along with the β^- strengths obtained in this analysis satisfies the sum rule at E_p = 200 MeV for ^{51}V and ^{54}Fe and achieves 80% of the sum rule prediction for ^{59}Co. Somewhat smaller fractions of the sum rule prediction are seen at lower beam energies. However, the ^{51}V and ^{59}Co β^- strengths are minimum values due to assumptions made in deriving them. These strengths are extracted up to about 15–20 MeV excitation energy and are, therefore, incomplete. Although the measured β^+ strengths are also incomplete, it is possible that the full GT sum rule prediction may be fulfilled in the visible spectrum without having to resort to non-nucleonic degrees of freedom to explain 'missing' strength.

Acknowledgment

It is necessary to record my gratitude to many people whose help and support along the way were essential to the completion of this thesis. I cannot name them all individually, but a few deserve special mention.

- David Aschman, my supervisor, for his support and encouragement and for all I've learned from him.
- The staff of the National Accelerator Centre (NAC) for the facility to perform the experiments, and for the high quality of service that they provided.
- The University of Cape Town, for financial assistance during this work.
- The staff of the Physics Department of the University of Cape Town for their friendship and helpfulness over many years.
- My parents, for not only contributing the author, but also for a lifetime of support and encouragement.

Contents

1 Introduction **8**

2 Theory **11**

2.1 Nuclear Beta Decay 11

2.2 Direct Nuclear Reactions 12

2.3 Correspondence of the (p,n) Reaction to Beta Decay 14

2.4 Relative Strengths of Gamow-Teller Transitions 16

2.5 Ratio of Gamow-Teller to Fermi Interaction Strengths 16

2.6 Mixed Gamow-Teller and Fermi Transitions 17

2.7 Even-A Targets Without Analog Beta Decays 18

2.8 Odd-A Targets Without Analog Beta Decays 18

2.9 Sum Rules 21

2.10 'Missing' Gamow-Teller Strength 21

3 Experimental Setup **24**

3.1 The Experimental Facility 24

3.2 The Proton Beam 25

3.3 The Targets 26

3.4 The Proton Telescope 26

3.5 The Neutron Detectors 27

3.6 Data Acquisition 28

3.7 Threshold Determination 28

3.8 Detector Resolution 29

3.9 Detector Efficiencies 30

3.10 Temperature Effects On Timing Measurements 31

3.11 Acquisition Electronics 31

3.11.1 Proton Telescope 31

3.11.2 Dead Time and Current Integrator 32

3.11.3 Triggers 32

3.11.4 ADC and TDC Electronics 33

3.12 Gain and Threshold Matching 33
3.13 Energy Resolution 34

4 Methods of Data Analysis **36**
4.1 The TOF Spectra 36
4.2 Wraparound Removal 40
4.3 Peak Fitting and Energy Calibration 41
4.4 The Differential Cross Sections and Transition Strengths 42

5 ^{51}V(p,n)^{51}Cr Analysis **45**
5.1 Fits to the Spectra 45
5.2 Cross Sections 49
5.3 Gamow-Teller Strength 52
5.4 Alternate Gamow-Teller Strength Calculation 57

6 ^{54}Fe(p,n)^{54}Co Analysis **60**
6.1 Fits to the Spectra 60
6.2 Cross Sections 64
6.3 Gamow-Teller Strength 67

7 ^{59}Co(p,n)^{59}Ni Analysis **72**
7.1 Fits to the Spectra 72
7.2 Cross Sections 76
7.3 Gamow-Teller Strength 77
7.4 Alternate Gamow-Teller Strength Calculation 81

8 Summary and Discussion **84**

APPENDIX **90**

A Results of the Spectrum Deconvolutions **90**
A.1 ^{51}V(p,n)^{51}Cr 91
A.2 ^{51}V(p,n)^{51}Cr assuming $f_{GT} = 0$ 93
A.3 ^{54}Fe(p,n)^{54}Co 95
A.4 ^{59}Co(p,n)^{59}Ni 98
A.5 ^{59}Co(p,n)^{59}Ni assuming $f_{GT} = 0$ 100

List of Figures

2.1 The energy dependence of (a) the magnitude of the four central terms of the effective interaction of Love and Franey, and (b) of the ratio of spin-flip to non-spin-flip terms of the central interaction. 14

2.2 Experimental Fermi and Gamow-Teller unit cross sections. 20

2.3 Background calculations of Osterfeld for $^{48}Ca(p,n)^{48}Sc$. 22

3.1 Schematic diagram of the NAC beam swinger. 25

3.2 A beam pulse time profile obtained using the proton telescope. 27

3.3 A typical beam time spectrum. 28

3.4 Typical residuals of the straight line fits to the cosmic ray paths for the six detectors. 29

3.5 Calculated absolute efficiencies. 31

3.6 The proton telescope circuitry. 31

3.7 The dead time and current integrator circuitry. 32

3.8 The neutron trigger. 33

3.9 The cosmic trigger. 33

3.10 The event trigger. 33

3.11 The time and pulse size signals. 33

3.12 A sketch of the neutron pulse size spectrum for one phototube showing its two components. 34

3.13 A typical ^{54}Fe spectrum taken with the transverse detector arrangement showing the resolution of the ground state and first excited state at 0.94 MeV. 35

3.14 A typical ^{54}Fe spectrum taken with the longitudinal detector arrangement showing the resolution of the ground state and first excited state at 0.94 MeV. 35

4.1 The TOF spectra for the six neutron detectors acquired during a typical 0° ^{51}V run at $E_p = 160$ MeV. 36

4.2 A typical pulse size spectrum. 37

4.3 A TOF spectrum and the cosmic events which would be rejected from it. 37

4.4 A scintillator arranged longitudinally to the incoming neutrons. 39

4.5 A typical spectrum of differences in times between the two ends of a detector. 39

4.6 The neutron wraparound removal procedure. 40

4.7 An ^{54}Fe(p,n)^{54}Co spectrum taken at 135 MeV at IUCF using the stripper loop to avoid wraparound background. 41
4.8 An example of a peak fit to the IAS. 42
4.9 An example of the peak fitting and excitation energy calibration procedure. 44

5.1 The ^{51}V(p,n)^{51}Cr TOF spectra at beam energies from 90 to 200 MeV. 46
5.2 The background and peak fits to the ^{51}V(p,n)^{51}Cr TOF spectra at the four beam energies. 47
5.3 Double differential cm cross sections for ^{51}V(p,n)^{51}Cr. 48
5.4 Zero degree cross sections as a function of beam energy for some of the transitions in ^{51}V(p,n)^{51}Cr. 50
5.5 Summed zero degree cross sections of all fitted discrete states for the ^{51}V(p,n)^{51}Cr reaction, excluding the IAS. 51
5.6 The distribution of the various multipole contributions to the ^{51}V 160 MeV spectrum. 51
5.7 Overlays of 0° and scaled 4° ^{51}V(p,n)^{51}Cr spectra. 52
5.8 GT strengths at the measured beam energies for some of the transitions in ^{51}V(p,n)^{51}Cr. 53
5.9 Calculated fraction of GT strength in the IAS transition of ^{51}V(p,n)^{51}Cr. 54
5.10 Double differential cm cross section for 0° ^{51}V(p,n)^{51}Cr at 200 MeV. 54
5.11 Estimated $\Delta L = 0$ component of the zero degree ^{51}V(p,n)^{51}Cr spectra at $E_p = 120$ and 160 MeV. 55
5.12 Summed GT strength in ^{51}V(p,n)^{51}Cr. 55
5.13 The Gamow-Teller sum rule quenching factors Q for ^{51}V(p,n)^{51}Cr. 56
5.14 GT strengths for a few of the peaks fitted to the ^{51}V(p,n)^{51}Cr spectra, assuming that the IAS is a pure Fermi transition. 58
5.15 Summed GT strength in ^{51}V(p,n)^{51}Cr, assuming that the IAS is a pure Fermi transition. 58
5.16 The Gamow-Teller sum rule quenching factors Q for ^{51}V(p,n)^{51}Cr, assuming that the IAS is a pure Fermi transition. 59
5.17 Summed GT strength in ^{51}V(p,n)^{51}Cr, assuming $f_{GT} = 0.5$. 59

6.1 The ^{54}Fe(p,n)^{54}Co TOF spectra at beam energies from 90 to 200 MeV. 61
6.2 The background and peak fits to the ^{54}Fe(p,n)^{54}Co TOF spectra at the four beam energies. 62
6.3 Double differential cm cross sections for ^{54}Fe(p,n)^{54}Co. 63
6.4 Zero degree cross sections as a function of beam energy for some of the transitions in ^{54}Fe(p,n)^{54}Co. 65
6.5 Summed zero degree cross sections of all fitted discrete states except the IAS for the ^{54}Fe(p,n)^{54}Co reaction. 66
6.6 Multipole decomposition of ^{54}Fe(p,n)^{54}Co at 300 MeV. 66
6.7 Overlays of 0° and scaled 4° ^{54}Fe(p,n)^{54}Co spectra. 67
6.8 GT strengths at the measured beam energies for some of the transitions in ^{54}Fe(p,n)^{54}Co. 68

6.9 Summed GT strength in ^{54}Fe(p,n)^{54}Co. 69
6.10 Overlayed spectra of the two ^{54}Fe(p,n)^{54}Co 160 MeV datasets showing the larger continuum background of the one. 70
6.11 Estimated $\Delta L = 0$ component of the zero degree ^{54}Fe(p,n)^{54}Co spectra at $E_p = 120$ and 160 MeV. 70
6.12 The Gamow-Teller sum rule quenching factors Q for ^{54}Fe(p,n)^{54}Co. 71

7.1 The ^{59}Co(p,n)^{59}Ni TOF spectra at beam energies from 90 to 200 MeV. 73
7.2 The background and peak fits to the ^{59}Co(p,n)^{59}Ni TOF spectra at the four beam energies. 74
7.3 Double differential cm cross sections for ^{59}Co(p,n)^{59}Ni. 75
7.4 Zero degree cross sections as a function of beam energy for some of the transitions in ^{59}Co(p,n)^{59}Ni. 76
7.5 Summed zero degree cross sections of all fitted discrete states for the ^{59}Co(p,n)^{59}Ni reaction, excluding the IAS. 77
7.6 Overlays of the 0° and scaled 4° ^{59}Co(p,n)^{59}Ni spectra at $E_p = 200$ MeV. 77
7.7 Estimated $\Delta L = 0$ component of the zero degree ^{59}Co(p,n)^{59}Ni spectrum at $E_p =$ 200 MeV. 78
7.8 GT strengths for a few of the transitions in ^{59}Co(p,n)^{59}Ni. 79
7.9 Calculated fraction of GT strength in the ^{59}Co(p,n)^{59}Ni IAS transition. 79
7.10 Summed GT strength in ^{59}Co(p,n)^{59}Ni. 80
7.11 The Gamow-Teller sum rule quenching factors Q for ^{59}Co(p,n)^{59}Ni. 80
7.12 GT strengths for a few of the transitions in ^{59}Co(p,n)^{59}Ni, assuming that the IAS is a pure Fermi transition. 82
7.13 Summed GT strength in ^{59}Co(p,n)^{59}Ni, assuming that the IAS is a pure Fermi transition. 82
7.14 The Gamow-Teller sum rule quenching factors Q for ^{59}Co(p,n)^{59}Ni, assuming that the IAS is a pure Fermi transition. 82
7.15 Summed GT strength in ^{59}Co(p,n)^{59}Ni, assuming $f_{\mathrm{GT}} = 0.5$. 83

8.1 Comparison of the spectra from the three reactions at 120 MeV. 85
8.2 Total measured GT strength in the three targets. 86
8.3 Estimated GT strength function for ^{59}Co(p,n)^{59}Ni compared with the two shell model calculations of Aufderheide *et al.* 87

Chapter 1

Introduction

The simplicity of the beta decay process makes it a powerful tool for the investigation of the weak interaction and of nuclear structure. The two main operators involved, the Fermi (F) and Gamow-Teller (GT) operators, change just the isospin projection, and the isospin and spin projections of a nucleon respectively. Beta decay studies enable the extraction of the transition matrix elements to high precision. However, most GT transition rates deduced from beta decay measurements turn out to be smaller than the calculated single particle rates [1, 2, 3], a phenomenon that has become known as the *quenching* of GT strength. Beta decay studies are limited to radioactive nuclei in which the transitions are energetically possible. These are invariably between states of low excitation energy, and are also often relatively weak transitions. In addition, the calculation of the beta decay strengths is model-dependent. The model-dependence and uncertainties would be reduced if larger fractions of the total strength were analysed [4]. It is, however, possible to do so with the use of other probes of spin-isospin strength and to compare the results of these to those of beta decay. One such probe is the zero degree (p,n) reaction at intermediate energies [2, 5, 6]. Such a reaction is not subject to some of the limitations of beta decay in that any desired target nucleus may be probed and that the GT strength function may be investigated up to high excitation energies in the final nucleus. The essential similarity of the transition matrix elements of the two processes allows the measured (p,n) strengths to be converted to beta decay strengths.

Although the potential usefulness of the (p,n) reaction has been known for many years, the experimental difficulties involved with high resolution neutron spectroscopy prevented its practical application for a long time. The uncharged nature of neutrons exclude the usual tools for energy determination. The most successful method of accurately measuring neutron energies is by time-of-flight measurement. However, the long flight paths required for sufficient time resolution, with their resultant small solid angles, prevented the effective use of the technique until the development of large volume neutron detectors with sub-nanosecond time resolution [5, 7] in the late 1970s.

Use of the (p,n) reaction allows one to select strong transitions with correspondingly lower uncertainties for use in determining the strengths. In addition there exists a model-independent sum rule [2, 8, 9] relating the difference in β^- and β^+ GT strengths, $B(\mathrm{GT})^{\pm}$, to the neutron-proton difference in the nucleus

$$\sum B(\mathrm{GT})^- - \sum B(\mathrm{GT})^+ = 3(N-Z)$$

where the summation is over all final states. The (p,n) reaction allows one to measure the summed GT^- strength. In many nuclei with a significant neutron excess the GT^+ strength is negligible due to Pauli blocking and the sum rule provides the expected GT^- strength. When the neutron excess is not sufficiently large, GT^+ strength must be measured in an (n,p) experiment or, at least, the sum rule provides a lower limit for the expected GT^- strength. Experiments to date have shown that, in general, quenching of the order of 40%–60% of the expected GT strength is observed in

(p,n) experiments [9, 10, 11, 12]. Attempts to explain this discrepancy have focussed mainly on causes for part of the GT strength to be removed from the observed spectrum into higher energy regions, and on the possibility that some of the strength is in the continuum part of the spectrum where it is just difficult to identify. Possible causes of the former effect include the configuration mixing of 2p2h states or excitations of non-nucleonic degrees of freedom.

The work presented in this thesis is from (p,n) experiments on three medium mass *fp*-shell nuclei, ^{51}V, ^{54}Fe, and ^{59}Co, in the energy range $90 \leq E_p \leq 200$ MeV.

Few measurements have been published for the ^{51}V$(p,n)^{51}$Cr reaction. Anderson *et al.* [13] published an angular distribution of the isobaric analog state (IAS) at $E_p = 14.8$ MeV for angles $\geq 23°$ soon after their discovery of the IAS in (p,n) reactions [14]. Langsford *et al.* [15] also published an angular distribution of the IAS at $E_p = 94$ MeV, as did Jolly *et al.* [16] at $E_p = 22$–40 MeV. The most detailed work published to date on ^{51}V is that of Rapaport *et al.* [17] at 160 MeV. This work included angular distributions for angles up to 20° and a measurement of the ground state cross section which enabled the Gamow-Teller strength function to be normalised to the beta decay strength. Since the beta decay strength is known from the decay $^{51}\mathrm{Cr} \xrightarrow{EC} {}^{51}\mathrm{V}$ [18] the (p,n) transition to the ^{51}Cr ground state is used to calibrate the GT strength in the rest of the spectrum. Some preliminary data were presented by Wang *et al.* [19, 20] at 120 MeV and 160 MeV in a study to extend to higher masses and odd-A nuclei the data on which the empirical ratio of Gamow-Teller to Fermi unit cross sections is based. This data was used by Huang [21] to propose a separate slope parameter for this ratio for odd mass nuclei from that used previously which was based primarily on even-A nuclei.

A low energy study of ^{54}Fe$(p,n)^{54}$Co ($32 \leq E_p \leq 40$ MeV) was done by Orihara *et al.* [22] which identified the IAS as well as two discrete states at 5.32 MeV and 10.23 MeV containing Gamow-Teller strength. Rapaport *et al.* [23] reported a measurement at $E_p = 160$ MeV which included the energy distribution of the $\Delta L = 0$ strength and cross sections for the IAS, the first excited state at 0.94 MeV, and several neutron groups above that energy. They also reported GT strengths for these and the summed strength up to $E_x = 13.5$ MeV. More recently Vetterli *et al.* [24] measured the GT strength at $E_p = 300$ MeV summed up to $E_x = 15$ MeV. Anderson *et al.* [25] published cross sections and GT strengths obtained from a measurement at $E_p = 135$ MeV which had a far better energy resolution than any obtained previously. They observed the fragmentation of the GT strength into more than 30 discrete states.

The work on ^{59}Co$(p,n)^{59}$Ni consists only of angular distributions of the IAS at $E_p = 14.8$ MeV by Anderson *et al.* [13] and at $E_p = 94$ MeV by Langsford *et al.* [15]. The reason for this lack of data is the difficulty in extracting the GT strengths from the measured cross sections. Unlike the ^{51}V case there is no beta decay against which to calibrate the strengths. The same applies to the ^{54}Fe case but since that is an even-even nucleus the IAS is a pure Fermi transition and the empirically derived ratio of GT to F unit cross sections [6, 26] may be used to obtain the GT strengths relative to the Fermi strength in the IAS. However, ^{59}Co is an odd-A nucleus and the IAS contains a mixture of GT and F strengths. The only available means of obtaining the GT strengths is by using the unit cross sections from the DWIA calculations of Taddeucci *et al.* [6]. However, there is a large uncertainty associated with these values. An alternate, independent means of obtaining the ratio of GT and F components of the IAS cross section is based on the transverse spin polarisation transfer coefficient, D_{NN}, measured with a polarised beam [21, 27]. Knowledge of this factor enables the calibration of the GT strengths relative to the F component of the IAS as for the ^{54}Fe case. Such an experiment is a very desirable proposition for future work.

Much work has also been done in attempting to calculate Gamow-Teller strengths. For *fp*-shell nuclei reasonable agreement with experiment is obtained for the total GT^- strength while the calculations appear consistently to overestimate the GT^+ strength [28]. A quenching factor of

approximately 0.7 brings the results back into line with the Ikeda sum rule [28]. Calculations on ^{54}Fe show that the GT$^+$ strength may be reduced by increasing the configuration space of the calculation [29, 30]. Aufderheide *et al.* [31] calculated GT strength functions for the three *fp*-shell nuclei in the mass range $50 < A < 60$ for which the GT$^+$ strength has been measured. These are the same three nuclei studied in this work. Their shell model calculations were in fair agreement with previously published measurements for the (p,n) direction but the strength measured in the (n,p) direction is only about 35% of the calculated amount. The GT$^-$ strength in ^{59}Co is the only point of comparison with these calculations for which no measurement has yet been published.

Chapter 2

Theory

2.1 Nuclear Beta Decay

Nuclear beta decay is the spontaneous conversion of a neutron to a proton within the nucleus accompanied by the emission of an electron and an antineutrino, or the conversion of a proton to a neutron with the emission of a positron and a neutrino. Very similar to the latter is the electron capture process in which an atomic electron combines with a proton in the nucleus to create a neutron while emitting a neutrino. They can be classified as follows (for bound nucleons):

$$\begin{aligned} \beta^- &: \quad n \rightarrow p + e^- + \bar{\nu} \quad \text{or} \quad (Z,N) \rightarrow (Z+1, N-1) + e^- + \bar{\nu} \\ \beta^+ &: \quad p \rightarrow n + e^+ + \nu \quad \text{or} \quad (Z,N) \rightarrow (Z-1, N+1) + e^+ + \nu \\ EC &: \quad p + e^- \rightarrow n + \nu \quad \text{or} \quad (Z,N) + e^- \rightarrow (Z-1, N+1) + \nu \end{aligned}$$

The simplest beta transitions are those for which no orbital angular momentum is carried away ($\Delta L = 0$). These transitions are known as *allowed* transitions and are heavily favoured over the so-called *forbidden* transitions, for which $\Delta L > 0$. If the initial and final states are such that allowed transitions can occur, then the higher order terms of the beta decay transition operator, which involve spherical harmonics of order greater than zero and are responsible for the forbidden transitions, may be neglected leaving two terms which correspond to the two types of allowed transitions which exist. These two types differ in whether the spin of the nucleus remains the same ($\Delta S = 0$) or is reversed ($\Delta S = 1$) during the transition and are called Fermi and Gamow-Teller transitions respectively. The nuclear part of the beta decay transition operator may then be written as [32]

$$\boldsymbol{O}(\beta) = g_V \sum_{k=1}^{A} \boldsymbol{\tau}_k^{\pm} + g_A \sum_{k=1}^{A} \boldsymbol{\sigma}_k \boldsymbol{\tau}_k^{\pm} \tag{2.1}$$

where the first term results in Fermi transitions and contains the isospin raising and lowering operator, $\boldsymbol{\tau}^{\pm}$. The second term, involving $\boldsymbol{\tau}^{\pm}$ and the spin operator, $\boldsymbol{\sigma}$, is responsible for Gamow-Teller transitions. g_V and g_A are the vector and axial vector coupling constants respectively.

Beta decay is a well understood process and provides reliable information related to the corresponding nuclear transition matrix elements [33]. The beta decay rates may be related to the Fermi and Gamow-Teller matrix elements according to [34]

$$(g_V)^2 B(\mathrm{F}) + (g_A)^2 B(\mathrm{GT}) = \frac{K}{ft} \tag{2.2}$$

where K is a constant that is obtained empirically and the Fermi and Gamow-Teller strengths,

$B(\mathrm{F})$ and $B(\mathrm{GT})$ respectively, are the squares of the transition matrix elements defined as

$$B(\mathrm{F})^{\pm} = \frac{1}{(2J_i+1)}|\langle f||\sum_k \tau_k^{\pm}||i\rangle|^2 \tag{2.3}$$

$$B(\mathrm{GT})^{\pm} = \frac{1}{(2J_i+1)}|\langle f||\sum_k \sigma_k\tau_k^{\pm}||i\rangle|^2 \tag{2.4}$$

and the $\pm$ indicates the β^+ and β^- directions, and J_i the spin of the initial state. Values of the coupling constants used in this thesis are obtained from ref. [35]

$$\frac{g_V}{(\hbar c)^3} = (1.14939 \pm 0.00065) \times 10^{-5} \ \mathrm{GeV}^{-2}$$

$$\frac{K}{(\hbar c)^6} = (8.120270 \pm 0.000012) \times 10^{-7} \ \mathrm{GeV}^{-4}\,\mathrm{s}$$

so that

$$\frac{K}{(g_V)^2} = 6146.6 \pm 3.5 \ \mathrm{s}$$

and from ref. [36]

$$\frac{g_A}{g_V} = 1.264 \pm 0.002$$

For a pure Gamow-Teller beta decay $B(\mathrm{F})^{\pm} = 0$ and

$$B(\mathrm{GT})^{\pm} = \left(\frac{g_V}{g_A}\right)^2 \frac{K/(g_V)^2}{ft} \tag{2.5}$$

The Fermi and Gamow-Teller matrix elements lead to certain selection rules [32] which may be summarised as follows:

	Fermi	Gamow-Teller
total ang. mom.	$\Delta J = 0$	$\Delta J = 0, \pm 1$, except $J_i = J_f = 0$
orbital ang. mom.	$\Delta L = 0$	$\Delta L = 0$
intrinsic ang. mom.	$\Delta S = 0$	$\Delta S = \pm 1$
isospin	$\Delta T = 0$, except $T_i = T_f = 0$	$\Delta T = 0, \pm 1$, except $T_i = T_f = 0$
isospin projection	$\Delta T_z = \pm 1$	$\Delta T_z = \pm 1$
parity	$\Delta \pi = 0$	$\Delta \pi = 0$

(2.6)

where the total angular momentum $\mathbf{J} = \mathbf{L} + \mathbf{S}$, and the change in isospin projection reflects the change in nucleon charge.

The primary restriction in beta decay studies is that it only occurs for a limited number of transitions. The complement of beta decay, a charge exchange reaction, can be used to probe any target nucleus and at energies far above those accessible to beta decay. As shown below, there is a strong correspondence between these two similar processes.

2.2 Direct Nuclear Reactions

Nuclear reactions such as the (p,n) reaction involve a projectile interacting with the many nucleons which make up the target nucleus. In general this problem cannot be solved exactly and the usual approach at the intermediate energies applicable to this thesis is to use the *Distorted Wave Impulse Approximation* (DWIA).

As the projectile approaches the target, and before it is close enough to interact with any one of the target nucleons, it is affected by the nuclear *optical potential* which models the average potential due to all the target nucleons. The optical potential parameters are determined by fits to elastic scattering data. The effect of this potential is to alter the wavefunction of the incoming projectile. If the projectile energy is sufficiently high it will then probably interact with a single target nucleon. The scattered nucleon is again affected by the optical potential as it leaves the nucleus causing the ejectile wavefunction also to be distorted [10, 32].

For single nucleon projectiles with energies above ~ 100 MeV the de Broglie wavelength is small compared to the mean free path inside the target nucleus and it essentially interacts with a single nucleon inside the nucleus [11, 37, 38, 39]. The interaction between the projectile and the bound nucleon is then approximated by the interaction between two free nucleons. This is known as the *Impulse Approximation.* In practice this is done by assuming that the $\boldsymbol{\tau}$-matrix (where $\boldsymbol{\tau}_i$ is the transition operator that describes the scattering of the projectile from the ith target nucleus in the presence of the other $(A-1)$ nucleons) is the same as the $\boldsymbol{t}$-matrix (where $\boldsymbol{t}_i$ is the free NN transition operator).

The target and projectile nucleons interact via the two-nucleon interaction, V_{ij}. The interaction, V, of target and projectile is then the sum of V_{ij} over all the nucleons in the target and projectile. In general this leads to the need to solve an infinite set of coupled equations. Usually the problem is reformulated to solving a reduced, finite set of coupled equations with a modified or *effective* interaction that takes into account in an average way the states excluded from the reduced set [11, 37, 38]. It is usual to use the form of the $\boldsymbol{t}$-matrix and effective interaction as determined by Love and Franey [40, 41].

The effective interaction of Love and Franey, V_{ip}, for each NN channel is represented by the sum of central (C), spin-orbit (LS), and tensor (T) terms [40, 41]

$$V_{ip} = V^C(r_{ip}) + V^{LS}(r_{ip})\mathbf{L}\cdot\mathbf{S} + V^T(r_{ip})S_{ip} \tag{2.7}$$

where the subscripts i and p refer to the ith target nucleon and the projectile respectively. The central part of V is itself comprised of four components

$$V^C = V_o^C + V_\sigma^C \boldsymbol{\sigma}_i\cdot\boldsymbol{\sigma}_p + V_\tau^C \boldsymbol{\tau}_i\cdot\boldsymbol{\tau}_p + V_{\sigma\tau}^C \boldsymbol{\sigma}_i\cdot\boldsymbol{\sigma}_p\boldsymbol{\tau}_i\cdot\boldsymbol{\tau}_p$$

while the LS and T parts each have two components

$$V^{LS} = V_o^{LS} + V_\tau^{LS}\boldsymbol{\tau}_i\cdot\boldsymbol{\tau}_p$$

$$V^T = V_o^T + V_\tau^T\boldsymbol{\tau}_i\cdot\boldsymbol{\tau}_p$$

The (p,n) reaction proceeds via the isovector terms of the interaction. At low momentum transfer, q, the LS and T terms are negligible and the effective interaction reduces to just the isovector components of the central part

$$V_{ip} = V_\tau^C\boldsymbol{\tau}_i\cdot\boldsymbol{\tau}_p + V_{\sigma\tau}^C\boldsymbol{\sigma}_i\cdot\boldsymbol{\sigma}_p\boldsymbol{\tau}_i\cdot\boldsymbol{\tau}_p \tag{2.8}$$

The energy dependence of the four central terms is shown in figure 2.1a. The isoscalar terms, V_o^C and V_σ^C, are not selected in (p,n) reactions. In the energy region of this work (100 – 200 MeV) the spin-flip term is nearly constant and dominates over the rapidly decreasing non-spin-flip term. This ratio is shown explicitly in figure 2.1b, and shows how useful this energy range is for investigating the spin-flip process. Indeed, it was only when proton bombarding energies reached 45 MeV that the giant Gamow-Teller resonance was first seen by Doering *et al.* [42], whereas the spin-independent transition to the IAS had been observed for some time at lower energies since its discovery by Anderson and Wong [14].

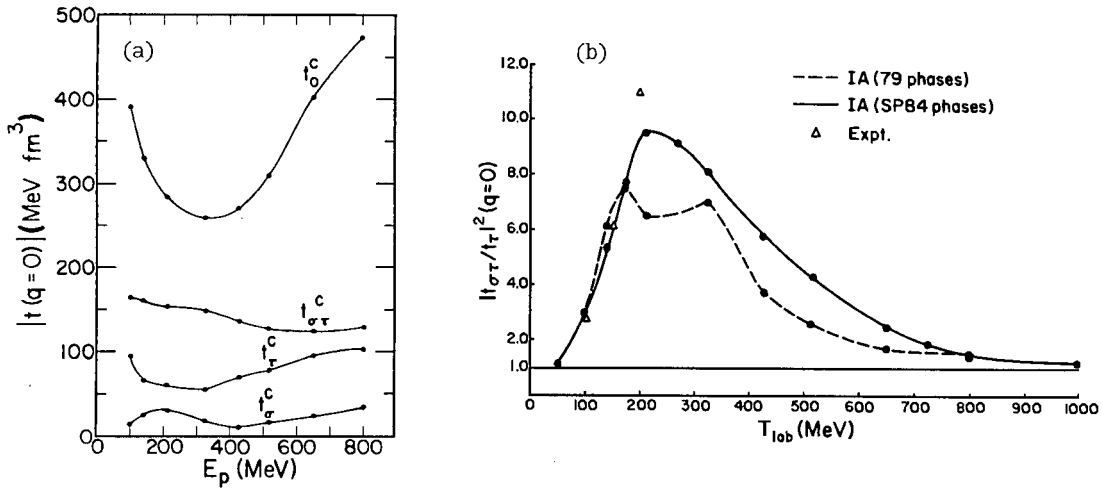

Figure 2.1: The energy dependence of (a) the magnitude of the four central terms of the effective interaction of Love and Franey (from ref [40]), and (b) of the ratio of spin-flip to non-spin-flip terms of the central interaction (from ref [41]).

2.3 Correspondence of the (p, n) Reaction to Beta Decay

The (p,n) reaction selects only isovector transitions. In the low momentum transfer limit where only the central part of the effective interaction is significant, the effective interaction is reduced to just the two terms which mediate low momentum transfer spin-flip ($\Delta S = 1$) and non-spin-flip ($\Delta S = 0$) transitions (from eq. 2.8)

$$\sum_i V_{\sigma\tau}(r_{ip})\boldsymbol{\sigma}_i \cdot \boldsymbol{\sigma}_p \boldsymbol{\tau}_i \cdot \boldsymbol{\tau}_p \qquad \text{and} \qquad \sum_i V_\tau(r_{ip})\boldsymbol{\tau}_i \cdot \boldsymbol{\tau}_p$$

These are similar to the corresponding beta decay operators from eq. 2.1

$$g_A \sum_k \boldsymbol{\sigma}_k \boldsymbol{\tau}_k^\pm \qquad \text{and} \qquad g_V \sum_k \boldsymbol{\tau}_k^\pm$$

so the reduced matrix elements of eq. 2.3 and eq. 2.4 are expected to be the same for beta decay and (p,n). This is a reflection of the fact that, although the reaction mechanism differs, the nuclear structure part of the two processes is very similar since they occur between two very similar states. If the (p,n) reaction occurs in the inverse direction to the beta decay, then the two strengths are related by

$$B(\mathrm{GT})_{pn} = \frac{(2J_i+1)_\beta}{(2J_i+1)_{pn}} B(\mathrm{GT})_\beta \tag{2.9}$$

The same relationship holds between the beta decay and (p,n) Fermi strengths but according to the selection rules of eq. 2.6 the J_i of the two states are always the same and the proportionality is unity.

For the (p,n) reaction to simulate the beta decay conditions it has to be performed at as small a momentum transfer as possible, since the allowed beta decays occur at essentially zero momentum transfer ($q = 0$). These conditions are best met at 0° and at high bombarding energies where the impulse approximation is valid. In the present experiment q varied (as a function of beam energy $90 \leq E_p \leq 200$ MeV, target $51 \leq A \leq 59$, and final state excitation energy $0 \leq E_x \leq 20$ MeV) between $0.01\,\mathrm{fm}^{-1}$ and $0.36\,\mathrm{fm}^{-1}$.

Taddeucci *et al.* [6, 26] developed a simple parameterization of the (p,n) cross section in order to assist in relating it to the beta decay transition strengths. The parameterization consists of the

product of three terms (assuming a pure Fermi or GT transition)

$$\sigma(q,\omega) = \hat{\sigma}(E_p, A)_\alpha F(q,\omega)_\alpha B(\alpha) \tag{2.10}$$

where α = F or GT. The *unit cross section* $\hat{\sigma}$ contains the target dependence. The factor $F(q,\omega)$ accounts for the non-zero momentum (q) and energy (ω) transfer of the (p,n) reaction and is used to extrapolate the cross section to $q = \omega = 0$. $F(q,\omega)$ approaches unity as $(q,\omega) \rightarrow (0,0)$. The extrapolated cross section is then

$$\sigma(0,0) = \frac{\sigma(q,\omega)}{F(q,\omega)} \tag{2.11}$$

In the distorted wave impulse approximation assuming only $\Delta L = 0$ transitions and central interactions the cross section is parameterized as

$$\sigma(q,\omega) = K(E_p,\omega)\exp[-\frac{1}{3}q^2 <r^2>]\exp[-xA^{1/3} + p(\omega)]|J_\alpha|^2 B(\alpha) \tag{2.12}$$

Then

$$\sigma(0,0) = K(E_p,0)\exp[-xA^{1/3} + a_o]|J_\alpha|^2 B(\alpha) \tag{2.13}$$

and factor $F(q,\omega)$ becomes

$$F(q,\omega) = \frac{K(E_p,\omega)}{K(E_p,0)}\exp[-\frac{1}{3}q^2 <r^2>]\exp[p(\omega) - a_o] \tag{2.14}$$

where J_α is the volume integral of the central non-spin-flip or spin-flip part of the effective NN interaction and $<r^2>=<r^2>_\rho + <r^2>_t + <r^2>_D$ is the sum of mean square radii of the transition density and effective interaction plus a correction for distortion. $p(\omega) = a_o + a_1\omega + a_2\omega^2$ is a polynomial expansion in the energy loss ω. The factor $K(E_p,\omega)$ is a kinematic factor given by

$$K(E_p,\omega) = \frac{E_i E_f}{(\hbar^2 c^2 \pi)^2}\frac{k_f}{k_i} \tag{2.15}$$

where E_i, k_i and E_f, k_f are the initial (projectile) and final (ejectile) reduced energies and wavenumbers in the cm frame.

Comparison with another parameterization by Goodman *et al.* [43]

$$\sigma(q,\omega) = K(E_p,\omega)N_\alpha|J_\alpha|^2 B(\alpha) \tag{2.16}$$

where N_α is a 'distortion factor' defined by the ratio of plane waves to distorted waves cross sections

$$N(q,\omega) = \frac{\sigma(\mathrm{DW};q,\omega)}{\sigma(\mathrm{PW};0)}$$

results in the relation

$$N(q,\omega) = \exp[-\frac{1}{3}q^2 <r^2>]\exp[-xA^{1/3} + p(\omega)]$$

Generally $F(q,\omega)$ is determined with a full DWIA calculation including non-central interactions and $\Delta L \neq 0$ amplitudes using a computer code such as DW81 [44]. Taddeucci *et al.* [6] demonstrated good agreement between the simple parameterization of eq. 2.12 and full DWIA calculations for targets with $A \leq 90$ (ie. including the targets used in this work) and in the range of momentum and energy transfer applicable to this work. This parameterization is, therefore, used in the current analysis.

2.4 Relative Strengths of Gamow-Teller Transitions

In the DWIA the (p,n) cross section for a purely central interaction in the limit of low momentum transfer is given by eq. 2.16 [6, 43]. For pure GT transitions this is

$$\sigma(q,\omega)_{\rm GT} = K(E_p,\omega) N_{\sigma\tau} |J_{\sigma\tau}|^2 B({\rm GT})$$

and, therefore, for two GT transitions, 1 and 2, originating in the same target

$$\frac{\sigma(q,\omega)_1}{\sigma(q,\omega)_2} = \frac{K(E_p,\omega)_1}{K(E_p,\omega)_2} \frac{N^1_{\sigma\tau} |J^1_{\sigma\tau}|^2}{N^2_{\sigma\tau} |J^2_{\sigma\tau}|^2} \frac{B({\rm GT})_1}{B({\rm GT})_2}$$

$N_{\sigma\tau} |J_{\sigma\tau}|^2$ is expected to be state-independent [6, 10] for transitions in the same nucleus. Therefore, if one GT transition strength in a spectrum is known, any other GT transition strength in that spectrum may be obtained by

$$B({\rm GT})_2 = \frac{\sigma(q,\omega)_2}{\sigma(q,\omega)_1} \frac{K(E_p,\omega)_1}{K(E_p,\omega)_2} B({\rm GT})_1 \tag{2.17}$$

Although not used in this analysis, the use of equation 2.10 instead of equation 2.16 would have resulted in a relation similar to equation 2.17, except with the approximation $K(E_p,\omega)$ replaced by $F(q,\omega)$.

2.5 Ratio of Gamow-Teller to Fermi Interaction Strengths

Based on data from a variety of mostly even-A targets, Taddeucci *et al.* [6, 26] noticed a proportionality between F and GT cross sections and the corresponding strengths which led them to define the following empirical ratio

$$R(E_p,A)^2 = \frac{\hat{\sigma}(E_p,A)_{\rm GT}}{\hat{\sigma}(E_p,A)_{\rm F}} \tag{2.18}$$

where the unit cross sections are defined in eq. 2.10 by (α = F or GT)

$$\hat{\sigma}_\alpha = \frac{\sigma(q=0)_\alpha}{B(\alpha)} \tag{2.19}$$

so that

$$R(E_p,A)^2 = \frac{\sigma(q,\omega)_{\rm GT}/B({\rm GT})F(q,\omega)_{\rm GT}}{\sigma(q,\omega)_{\rm F}/B({\rm F})F(q,\omega)_{\rm F}} \tag{2.20}$$

This can be interpreted in terms of the quantities in eq. 2.16 as

$$R(E_p,A)^2 = \frac{K(E_p,\omega)_{\rm GT}}{K(E_p,\omega)_{\rm F}} \frac{F(q,\omega)_{\rm F}}{F(q,\omega)_{\rm GT}} \frac{N_{\sigma\tau}}{N_\tau} \left|\frac{J_{\sigma\tau}}{J_\tau}\right|^2 \tag{2.21}$$

$$\simeq \frac{N_{\sigma\tau}}{N_\tau} \left|\frac{J_{\sigma\tau}}{J_\tau}\right|^2 \tag{2.22}$$

for momentum transfer $q \simeq 0$ and GT and F transitions not widely separated in energy. DWIA calculations then indicate that the ratio of distortion factors is close to unity ($N_{\sigma\tau}/N_\tau = 1.2 \pm 0.1$) [6, 26], so that this empirical and model-independent ratio, R, closely represents the ratio of interaction strengths $|J_{\sigma\tau}/J_\tau|$.

The data show that for energies above ~50 MeV R has a linear dependence on E_p

$$R(E_p,A) = \frac{E_p}{E_o}, \qquad E_o = 55.0 \pm 0.4\,{\rm MeV} \tag{2.23}$$

The target dependence below ~50 MeV is a result of the DWIA no longer being a good approximation so that eq. 2.22 is no longer valid.

The unit cross sections appear to have some target mass dependence with large variations between neighbouring nuclei. This is not expected from DWIA calculations and is still not understood [10]. However, the smooth A-dependence of the ratio of unit cross sections shows that both the F and GT unit cross sections have the same mass dependence and suggests that the cause of this effect is in the reaction dynamics rather than in the nuclear structure. Use of the ratio rather than the unit cross sections separately avoids this uncertainty.

It has been noted by several authors [20, 21] that the value for E_o is based almost exclusively on data from light, even-A targets. Some evidence that E_o may differ from the value 55.0 ± 0.4 MeV for odd-A targets is presented by Wang *et al.* [19, 20]. They present values of R obtained from four odd-A targets (^{51}V, ^{87}Rb, ^{113}In, ^{141}Pr) at beam energies of 120 and 160 MeV. The results are preliminary since the cross sections have not yet been corrected for the momentum transfer. The mean value for E_o obtained from these data is $E_o = 44.2 \pm 1.8$ MeV.

An independent means of obtaining R is through the use of the transverse spin polarisation transfer coefficient, $D_{\rm NN}$, obtained in polarised $(\vec{p},\vec{n})$ experiments [9, 21, 27]. This quantity is the ratio of transverse polarisations of the outgoing and incoming particles and can be related to the ratio of GT cross section to the total cross section in the mixed IAS (assuming purely central forces) according to [21]

$$f_{\rm GT} \equiv \frac{\sigma_{\rm GT}}{\sigma_{\rm IAS}} = \frac{3}{4}[1 - D_{\rm NN}(IAS)]$$

This may then be related back to R for transitions for which B(GT) may be obtained from an analog beta decay. Using data from his work and from references [19, 20, 27], Huang [21] obtained a value of E_o for odd-A targets of 45.0 ± 0.6 MeV.

More recently, Goodman [45] has cast doubt on this alternate value of E_o. Preliminary spin transfer data on odd mass targets in the range $89 \leq A \leq 97$ yield results consistent with $E_o = 55$ MeV. He believes that non-GT contributions to the cross sections of the states which were used to normalise the spectra were responsible for the effect described above.

The value of E_o as stated in eq. 2.23 is, therefore, adopted in this work.

2.6 Mixed Gamow-Teller and Fermi Transitions

The Fermi strength is assumed concentrated in the IAS [9, 46, 47]. Odd-A nuclei have ground states of $J > 0$. The transition to the IAS of the target ground state has $\Delta J = 0$, and by the selection rules of eq. 2.6 it may be reached by either a Fermi or a GT transition. The IAS cross section will therefore be a mixture of the two

$$\sigma(q,\omega)_{\rm IAS} = \sigma(q,\omega)_{\rm F} + \sigma(q,\omega)_{\rm GT}$$

The fraction of the cross section that is GT is

$$f_{\rm GT} \equiv \frac{\sigma(q,\omega)_{\rm GT}}{\sigma(q,\omega)_{\rm IAS}}$$

so that

$$\sigma(q,\omega)_{\rm F} = (1 - f_{\rm GT})\sigma(q,\omega)_{\rm IAS}$$

Substituting this into eq. 2.20 gives

$$R(E_p, A)^2 = \frac{1}{(1 - f_{\rm GT})} \frac{\sigma(q,\omega)_{\rm GT}}{\sigma(q,\omega)_{\rm IAS}} \frac{F(q,\omega)_{\rm F}}{F(q,\omega)_{\rm GT}} \frac{B({\rm F})}{B({\rm GT})}$$

Since $R(E_p,A)^2$ contains the unit cross sections which are expected to be state-independent, the ratio $\sigma(q,\omega)_{\rm GT}/(F(q,\omega)_{\rm GT}B({\rm GT}))$ can be that of any GT state in the spectrum. Rearranging this gives

$$f_{\rm GT} = 1 - \frac{1}{R(E_p,A)^2}\frac{\sigma(q,\omega)_{\rm GT}}{\sigma(q,\omega)_{\rm IAS}}\frac{F(q,\omega)_{\rm F}}{F(q,\omega)_{\rm GT}}\frac{B({\rm F})}{B({\rm GT})} \tag{2.24}$$

which allows calculation of the fraction of GT cross section in the IAS if we have another GT transition whose strength is known from beta decay. Now the $B({\rm GT})$ of one transition relative to another GT transition of known $B({\rm GT})$ is given by eq. 2.17, so that

$$B({\rm GT})_{\rm IAS} = \frac{\sigma(q,\omega)_{\rm GT,IAS}}{\sigma(q,\omega)_{\rm GT}}\frac{K(E_p,\omega)_{\rm GT}}{K(E_p,\omega)_{\rm IAS}}B({\rm GT})_{\rm GT}$$

and so

$$B({\rm GT})_{\rm IAS} = f_{\rm GT}\frac{\sigma(q,\omega)_{\rm IAS}}{\sigma(q,\omega)_{\rm GT}}\frac{K(E_p,\omega)_{\rm GT}}{K(E_p,\omega)_{\rm IAS}}B({\rm GT})_{\rm GT} \tag{2.25}$$

2.7 Even-A Targets Without Analog Beta Decays

In the low momentum transfer limit the DWIA cross section is given by eq. 2.16. For pure Fermi and Gamow-Teller transitions this becomes

$$\sigma(q,\omega)_{\rm F} = K(E_p,\omega)N_\tau\,|J_\tau|^2\,B({\rm F})$$

and

$$\sigma(q,\omega)_{\rm GT} = K(E_p,\omega)N_{\sigma\tau}\,|J_{\sigma\tau}|^2\,B({\rm GT})$$

In even-A targets the transition to the IAS is pure Fermi, and so the ratio of cross sections of any GT transition and the IAS transition is

$$\frac{\sigma(q,\omega)_{\rm GT}}{\sigma(q,\omega)_{\rm F}} = \frac{K(E_p,\omega)_{\rm GT}}{K(E_p,\omega)_{\rm F}}\frac{N_{\sigma\tau}|J_{\sigma\tau}|^2}{N_\tau|J_\tau|^2}\frac{B({\rm GT})}{B({\rm F})}$$

Then

$$\begin{aligned}\frac{\sigma(0,0)_{\rm GT}}{\sigma(0,0)_{\rm F}} &= \frac{F(q,\omega)_{\rm F}}{F(q,\omega)_{\rm GT}}\frac{K(E_p,\omega)_{\rm GT}}{K(E_p,\omega)_{\rm F}}\frac{N_{\sigma\tau}|J_{\sigma\tau}|^2}{N_\tau|J_\tau|^2}\frac{B({\rm GT})}{B({\rm F})}\\ &= R(E_p,A)^2\frac{B({\rm GT})}{B({\rm F})}\end{aligned}$$

from eq. 2.21, and therefore

$$B({\rm GT}) = \frac{B({\rm F})}{R(E_p,A)^2}\frac{\sigma(0,0)_{\rm GT}}{\sigma(0,0)_{\rm F}} \tag{2.26}$$

For targets such as ^{54}Fe no analog beta decay exists from which to obtain the Gamow-Teller strength for any particular transition. In these cases one has to obtain the GT strength relative to the F strength in the IAS using the proportionality relation of Taddeucci (eq. 2.18) where E_o is taken from eq. 2.23.

2.8 Odd-A Targets Without Analog Beta Decays

Odd mass targets have their Fermi strength mixed together with some Gamow-Teller strength in the IAS. Ideally one would like to use Taddeucci's [6, 26] proportionality relation of section 2.5

and the procedure outlined in section 2.6 to extract the GT strengths relative to the F strength. However, this requires knowledge of the strength of one other pure GT transition which is usually obtained from an analog beta decay.

If no analog beta decay exists, one is forced to extract the GT unit cross sections from the plots of $\hat{\sigma}$ vs. A published in ref. [6] and reproduced in figure 2.2. The unit cross section can then be used to obtain $B(\mathrm{GT})$ for the pure GT transitions in the spectrum according to eq. 2.10

$$B(\mathrm{GT}) = \frac{\sigma(q,\omega)_{\mathrm{GT}}}{F(q,\omega)_{\mathrm{GT}}\hat{\sigma}_{\mathrm{GT}}} \tag{2.27}$$

Noting that

$$R(E_p,A)^2 = \frac{\hat{\sigma}_{\mathrm{GT}}}{\hat{\sigma}_{\mathrm{F}}} = \hat{\sigma}_{\mathrm{GT}}\frac{F(q,\omega)_{\mathrm{F}}B(\mathrm{F})}{\sigma(q,\omega)_{\mathrm{F}}}$$

so that

$$\frac{\sigma(q,\omega)_{\mathrm{F}}}{\hat{\sigma}_{\mathrm{GT}}} = \frac{F(q,\omega)_{\mathrm{F}}B(\mathrm{F})}{R(E_p,A)^2}$$

the Gamow-Teller strength in the mixed IAS transition can be obtained

$$\begin{aligned} B(\mathrm{GT}) &= \frac{\sigma(q,\omega)_{\mathrm{IAS}} - \sigma(q,\omega)_{\mathrm{F}}}{F(q,\omega)_{\mathrm{GT}}\hat{\sigma}_{\mathrm{GT}}} \\ &= \frac{\sigma(q,\omega)_{\mathrm{IAS}}}{F(q,\omega)_{\mathrm{GT}}\hat{\sigma}_{\mathrm{GT}}} - \frac{\sigma(q,\omega)_{\mathrm{F}}}{F(q,\omega)_{\mathrm{GT}}\hat{\sigma}_{\mathrm{GT}}} \\ &= \frac{\sigma(q,\omega)_{\mathrm{IAS}}}{F(q,\omega)_{\mathrm{GT}}\hat{\sigma}_{\mathrm{GT}}} - \frac{F(q,\omega)_{\mathrm{F}}}{F(q,\omega)_{\mathrm{GT}}}\frac{B(\mathrm{F})}{R(E_p,A)^2} \end{aligned} \tag{2.28}$$

This is a very unsatisfactory procedure because, not only do the DWIA calculations fail to reproduce the data very well (esp. at 200 MeV), but there is considerable variation in the experimental values of $\hat{\sigma}_{\mathrm{GT}}$ (and $\hat{\sigma}_{\mathrm{F}}$). In fact, there are variations in $\hat{\sigma}_{\mathrm{GT}}$ of up to 50% from isotope to isotope [6]. Extraction of $\hat{\sigma}_{\mathrm{GT}}$ therefore leads to large uncertainties. As discussed in section 2.5 these variations appear to be the same for $\hat{\sigma}_{\mathrm{GT}}$ and $\hat{\sigma}_{\mathrm{F}}$ so it would be preferable to be able to use the ratio of the two if that were possible.

Anderson *et al.* [48, 49] attempted to determine a 'universal' relationship between a 0° (p,n) cross section and $B(\mathrm{GT})$. They derived the relation

$$B(\mathrm{GT})_{pn} = \frac{\sigma_{\mathrm{GT}}(q=0)}{N_D}C_{\mathrm{GT}}$$

where C_{GT} is an energy dependent proportionality factor obtained by comparison with analog beta decay and N_D is a distortion factor calculated with a DWIA code. This would allow the determination of the GT strength for any pure GT transition in the spectrum and hence the strength of the GT component of the IAS by eq. 2.25. However, this relation was, once again, obtained from comparisons of relatively strong transitions from even-A target nuclei, and it is suspect for odd-A nuclei [49].

Ideally, measurement of the transverse spin polarisation transfer coefficient, D_{NN}, from a polarised beam experiment would be used to obtain an independent value of the fraction f_{GT} from which the GT strengths could then be determined. However, the present experiment was an unpolarised one and this value is not available.

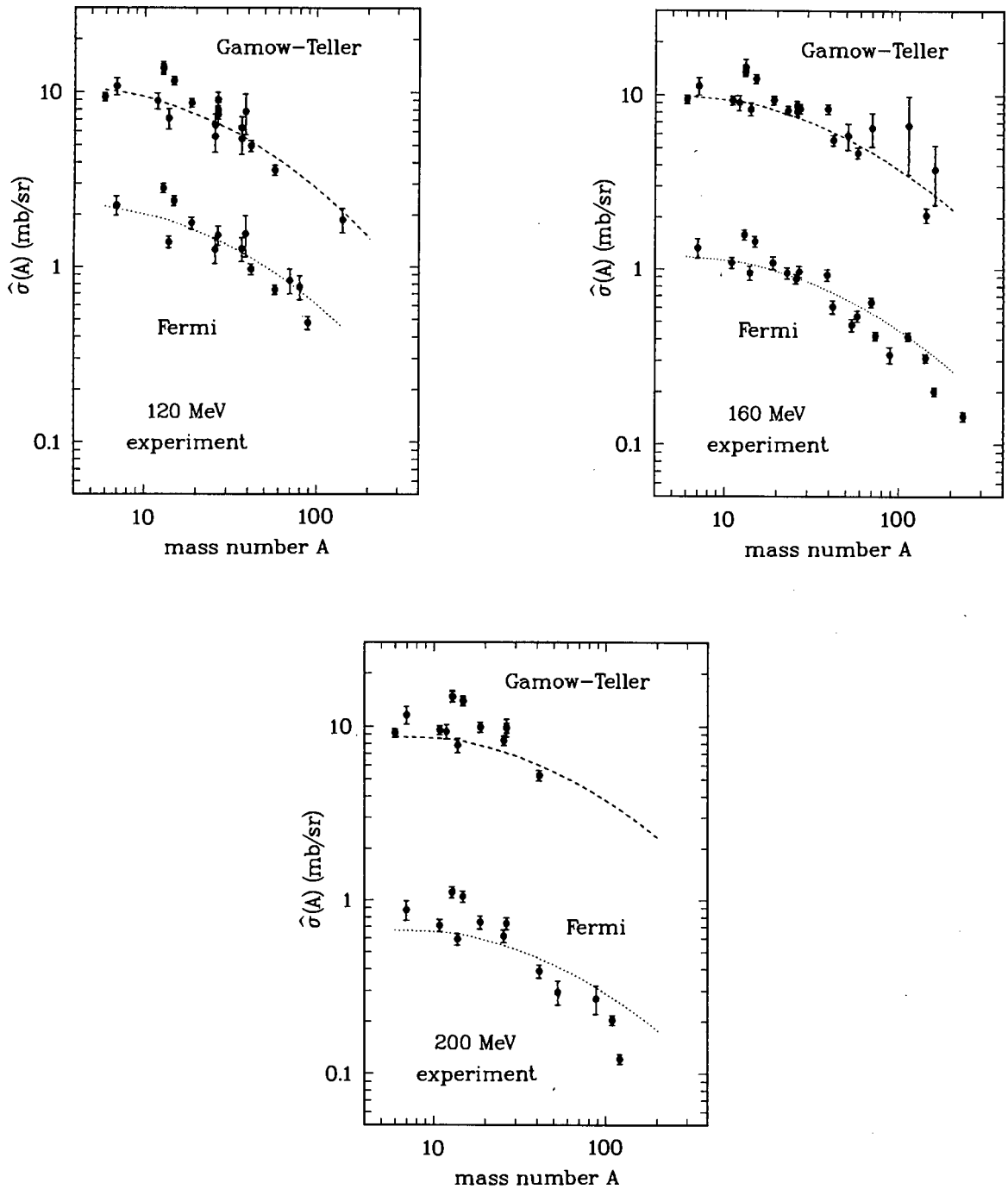

Figure 2.2: Experimental Fermi and Gamow-Teller unit cross sections reproduced from Taddeucci *et al.* [6]. The dashed line corresponds to the parameterization of eq. 2.12 and the dotted line is the dashed line divided by $(E_p/55)^2$.

2.9 Sum Rules

It is useful to consider the sum of all strength of a particular type, $S(\alpha)^{\pm}$, where α is F or GT and the $\pm$ corresponds to the β^+ or (n,p) and β^- or (p,n) direction respectively. Then

$$S(\alpha)^{\pm} = \sum B(\alpha)^{\pm}$$

where the summation is over all of the final states. In the case of a free neutron $B(\mathrm{F})^- = 1, B(\mathrm{F})^+ = 0, B(\mathrm{GT})^- = 3, B(\mathrm{GT})^+ = 0$. The factor 3 comes from the summation over the three spin directions in the GT case. In a simple argument by Goodman [2, 10] the nucleus is considered to consist of N neutrons and Z protons arranged in such a way that no Pauli blocking of transitions occur. Then all the nucleons would be able to decay and the sum of strengths would be $S(\mathrm{F})^-= N$, $S(\mathrm{F})^+= Z$, $S(\mathrm{GT})^-= 3N$, $S(\mathrm{GT})^+= 3Z$. The sum rules gives the differences between the two summed strengths

$$S(\mathrm{F})^- - S(\mathrm{F})^+ = N - Z \tag{2.29}$$

$$S(\mathrm{GT})^- - S(\mathrm{GT})^+ = 3(N - Z) \tag{2.30}$$

As the nucleons become arranged in a more realistic way with protons and neutrons in the same shells, transitions in both directions become blocked by the same amount but the difference in strengths remains the same. Formal derivations and discussions of the sum rules are given in references [8, 9, 11, 24].

The Fermi transition involves just a change of isospin, and as such it proceeds between two nearly identical states. In other words, the overlap of the two wavefunctions will be almost complete and the transition matrix element will be unity. The Fermi transition strength will therefore be concentrated in the transition to the IAS [9, 46, 47] so that

$$S(\mathrm{F})^{\pm} = B(\mathrm{F})^{\pm}$$

In neutron rich nuclei the Pauli exclusion principle forbids β^+ decay to low lying states. Therefore, the strength $B(\mathrm{F})^+ = 0$ and the Fermi sum rule reduces to

$$B(\mathrm{F})^- = N - Z \tag{2.31}$$

The Pauli exclusion principle also reduces the GT^+ strength in neutron rich nuclei. In nuclei with large neutron excesses the Pauli blocking may be sufficient to render the GT^+ strength negligible. Even when this is not the case the GT sum rule leads to a useful limiting relation [2, 50]

$$B(\mathrm{GT})^- \geq 3(N - Z) \tag{2.32}$$

2.10 'Missing' Gamow-Teller Strength

Most experiments to date have found that only about 40%–60% of the minimum strength expected from the GT sum rule is observed [9, 10, 11, 12]. Since the sum rule is derived from the properties of the nucleon isospin raising and lowering operators, it is an exact operator relationship and therefore model-independent. The problem of the 'missing' strength is thus not a problem of an insufficiently good model. However, if non-nucleonic degrees of freedom are important then the sum rule will be modified [9, 51].

It may simply be that some of the strength in the experimental spectra lies in a background below the discrete structure or in the continuum at high excitation energy. Any such strength would be very difficult to identify experimentally, and hence to extract from other components, because

of the lack of structure in the spectra in this region and because the large momentum transfers at high excitation energy result in low cross sections per unit GT strength. Osterfeld [52, 53] has performed calculations of the background of ^{48}Ca$(p,n)^{48}$Sc (see figure 2.3) which show that almost all the cross section below the discrete states is GT. Much of this is routinely discarded by experimentalists as part of a smooth 'background' curve drawn through the $\Delta L = 1$ resonance just above the discrete structure in the spectrum. It may also be the case that some of the strength is pushed up in excitation energy beyond the measured energy range. Configuration mixing of two-particle–two-hole states would achieve this [54]. A review of measured and calculated GT strengths in light nuclei ($A < 40$) by Rapaport [12] showed that the quenching of GT strength decreases as A increases in a given shell. It reached a minimum of ~0.4 for nuclei with a closed shell minus one particle, and jumped up to ~0.6 for nuclei with a closed shell plus one particle. This shell-closure effect could be interpreted as increased quenching when configuration mixing becomes important. Summarising the theoretical situation, Osterfeld [9] claims that 20%–30% of the GT strength may be shifted up to excitation energies from 30 to 70 MeV.

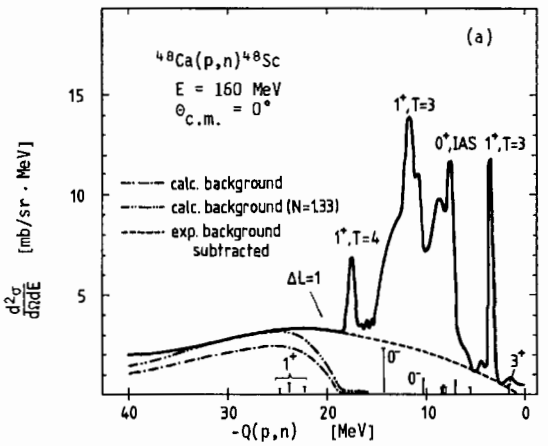

Figure 2.3: Background calculations (dash-dotted lines) of Osterfeld for ^{48}Ca$(p,n)^{48}$Sc compared to the usual experimental background (dashed line) (from ref. [53]).

Goodman *et al.* [55] have attempted to test this experimentally by subtracting a ^{40}Ca$(p,n)^{40}$Sc spectrum from a ^{42}Ca$(p,n)^{42}$Sc spectrum. Since ^{40}Ca should have essentially zero GT strength because $N = Z$, it was assumed to provide a reference point for the background in ^{42}Ca. Their results led them to conclude that most of the background is not due to GT strength, although Osterfeld [9] claims that their results could be consistent with up to 80% of the sum rule being present. Goodman and Bloom [4] later employed a revised procedure to analyse the background in ^{42}Ca. They used the difference between 0° and 2.5° ^{42}Ca spectra to model the $\Delta L \neq 0$ part of the 0° spectrum and subtracted this from the 0° spectrum. They believe their results to be in agreement with the previous results from reference [55]. In view of the experimental difficulties, theoretical calculations incorporating these effects are still necessary to test their importance. Unfortunately in many cases, and in particular for the middle *fp*-shell nuclei, the number of nucleons is too large for full shell model calculations to be done at present.

The review of the quenching of GT strength in light nuclei by Rapaport [12], referred to above, noted that quenching was observed to occur even in nuclei for which configuration mixing is expected to be least important. This would suggest that more than one effect is competing to reduce the amount of GT strength observed in (p,n) reactions. A candidate which has received much attention is the excitation of non-nucleonic degrees of freedom such as the delta isobar [2, 9, 11, 47]. Such an effect would push some of the strength up into the 300 MeV region, well above that observed in current charge exchange experiments. The magnitude of this effect is dependent on the delta-

nucleon interaction which is still not known with great confidence [11]. Osterfeld [9] summarises the current situation by stating that 5%–20% of the GT strength may be shifted up into the delta region, although there is, as yet, no decisive experimental test of this [9, 11]. In nuclear physics in general there is almost no need to invoke sub-nucleonic degrees of freedom [32] and, if shown to be important in the quenching of GT strength, this would be one of the very few cases in nuclear physics in which nucleon structure has a visible effect. As such it would be a very interesting and exciting development.

As implied by the above discussion, and particularly by recent reviews on the subject (see for example references [9, 33]), the question of the quenching of GT strength is still very much an open question and one of the primary motivations for further charge exchange work.

Chapter 3

Experimental Setup

A study of the (p,n) charge exchange reaction at intermediate energies requires the detection of neutrons and the measurement of their kinetic energies. The usual tools of charged particle spectroscopy are of little use for this purpose. The most successful method of accurately measuring neutron energies is by time-of-flight (TOF) measurement. Originally employed by Alvarez [56], it is the method used in this experiment. The time taken to travel a certain distance from target to detector is measured. From this the velocity and hence the kinetic energy may be calculated. This requires accurate measurement of the time taken by a neutron to travel the distance between the target and the detector, whereas crude energy measurement suffices for the setting of energy thresholds to cut out background noise and low energy wraparound. The time-of-flight method requires long flight paths for good energy resolution, which has the disadvantage that very small detection solid angles are covered.

3.1 The Experimental Facility

The neutron time-of-flight (NTOF) experiment described in this work was performed at the $k = 200$ cyclotron at the National Accelerator Centre (NAC) at Faure near Cape Town. Protons from the light-ion injector cyclotron, SPC1, were accelerated by the separated-sector cyclotron, SSC, to energies of up to 200 MeV. The protons were transported along beamline 'N' to the beam swinger (figure 3.1) positioned just in front of the target. The beam swinger consists of two dipole magnets which deflect the beam away from its original direction and then back on to the target at various angles. This allowed an angular distribution of reaction products to be measured without having to move the neutron detectors or the shielding and collimating material. A third dipole positioned just downstream of the target deflected all non-interacting beam protons and charged reaction products away from the detectors and into a beam dump. This setup allows angular distributions of 0° to 30° to be measured while the neutron detectors remain at 0° to the incoming beamline. The detectors can be moved to positions at 30°, 60°, and 90° to the beamline if measurements of larger angular distributions are desired. A ΔE-E proton telescope was situated just next to the target to detect elastically scattered protons for monitoring of the beam pulse width and stability with respect to the machine RF signal. The beam swinger and target were situated next to the wall of the cyclotron building. The neutron detectors were situated in a small hut in a field next to the building allowing for flight paths of up to 200 m at angles of up to 90° with respect to the incoming proton beam. The reaction products left the building via a hole in the wall, passing through a collimator which could be set to illuminate the detectors and shield the experimenters and the acquisition electronics.

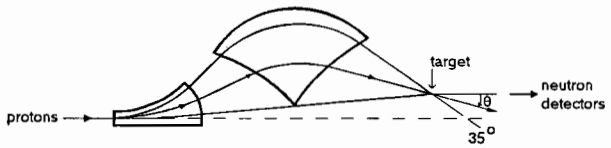

Figure 3.1: Schematic diagram of the NAC beam swinger showing the two deflecting magnets and three possible trajectories including the zero degree path and the path of greatest angle on target..

3.2 The Proton Beam

Beam currents on target of up to 2000 nA at 120 MeV and 600 nA at 200 MeV were obtained although most data were acquired using beam currents between 200 nA and 500 nA. The protons were produced in short, widely separated pulses. Due to the long flight path from the target to the detector the fast neutrons from a particular pulse would catch up with the slower neutrons from a previous pulse causing a 'wraparound' of the time-of-flight spectrum. This was largely eliminated by using pulse selection on the incident beam. Selection ratios of 1:5 to 1:7 were employed to increase the time between successive beam pulses on target. Despite the use of pulse selection, some wraparound still occurred and had to be treated offline in software (see section 4.2).

There was a small spread in proton energy within each beam pulse which depended on the width of collimator slits at a bending magnet close to the extraction point from the cyclotron. These were set [57] to give an energy resolution of 0.075% corresponding to 90 keV at $E_p = 120$ MeV and 150 keV at $E_p = 200$ MeV. As they traversed the beamline to the target protons of different energies followed slightly different paths resulting in a time spread within each pulse at the target.

This time spread was one of the largest contributors to the uncertainty in the time-of-flight of the neutrons to the detectors. It was of critical importance for the cyclotron operators to keep this spread to a minimum, and during the data acquisition described here the pulse width was kept between 400 ps and 800 ps (see figure 3.2).

The proton pulses left the cyclotron and pulse selector in phase with a radio frequency signal (PSRF) which was used to time the arrival of the beam pulses at the target. However, after traveling from the cyclotron to the target the pulses might no longer have been exactly in phase with the PSRF signal. A ΔE-E proton telescope (described below) was installed next to the targets to monitor this effect. A phase compensation unit was installed in an attempt to compensate for any slow drifts in the beam phase. The signal from the proton telescope was used to start a TAC which was stopped by the PSRF signal. The output voltage was monitored by the phase compensator which tried to maintain it at a fixed value. If the phase drifted the voltage changed and the phase compensator adjusted the PSRF time to bring the output voltage back to the same value. However, the low data rates combined with a long integration time of the phase compensation unit resulted in time jitter of $\sim$1 ns in the phase compensated PSRF signal and no better time resolution than before. Sufficient phase drift compensation was achieved by splitting the acquisition runs into short sections and adding them up in software after shifting them into phase with each other.

3.3 The Targets

The targets were mounted on a remotely controlled ladder with space for six targets at a time. Each target consisted of a circular disk 25 mm in diameter, except for the ^{51}V target which was a 20 mm wide rectangular strip. The beam spot on target was usually of the order of 1 cm in diameter. One of the target positions was always occupied by a quartz viewer to enable the cyclotron operators to aim the proton beam accurately. Another position was always taken up by a lithium target which was used for determining the detector efficiencies (see section 3.9). The lithium target consisted of a pressed disk of natural lithium (92.5% ^{7}Li, 7.5% ^{6}Li) mounted between two 2.5 μ Havar foils. Several thicknesses between 28.3 mg/cm^2 and 71.2 mg/cm^2 were employed. The iron target consisted of a 99.8% pure ^{54}Fe foil of surface density 15.45 mg/cm^2. The cobalt target was a ^{59}Co foil of 44.0 mg/cm^2 and the vanadium target was a ^{51}V foil of 48.8 mg/cm^2.

The thickness of the target caused another uncertainty in the projectile energy. As the charged protons moved through the target they lost energy. This energy loss could be calculated if it were known where the interactions occurred. Because this was not known, it was assumed that all interactions occurred in the centre of the targets, which lead to uncertainties in projectile energy of up to 80 keV for the ^{54}Fe target and 270 keV for the ^{59}Co target.

3.4 The Proton Telescope

A proton telescope consisting of two NE102A scintillators each coupled to a Hamamatsu H2431 photomultiplier tube was installed approximately 1 m away from the target and at an angle of 30° with respect to the beam direction. A coincidence between the two scintillators ensured that only charged particles originating in the target were observed. At high beam energies a 1" thick copper energy degrader was installed between the two scintillators to ensure that high energy protons were stopped inside the E detector. Tight pulse height windows were set on the signals to ensure that only the high energy, elastically scattered protons were considered. These were used to start a TAC. The TAC was stopped by the PSRF signal. Since the elastically scattered protons from different parts of the beam pulse took the same time to reach the telescope, their time structure with respect to the PSRF signal was the same as the time structure of the beam pulse. A typical pulse width of between 400 ps and 800 ps FWHM was measured and proved sufficiently narrow to ensure acceptable overall time resolution for the experiment (figure 3.2).

By continuously monitoring the beam time spectrum to see how much the peak shifted during a run it was possible to monitor phase shifts between the PSRF signal and the beam pulse. During many runs this was negligible. In those runs where shifts of 0.5 ns or more were observed, software corrections were made in later offline analysis by splitting the runs into short sections and shifting the sections into phase with other before adding them back together. An example is shown in figure 3.3 of a run during which such a phase shift took place. Part (a) shows the beam time spectrum (as in figure 3.2) and part (b) the same spectrum as a function of time with time running up the vertical axis. It can be seen that a phase shift took place just less than halfway through the run. The data would have been split at this point into two sections, shifted back into phase, and recombined. Also evident is a short period near the end of the run during which the beam disappeared, leaving zeros in both spectra. This section would have been omitted from the analysis.

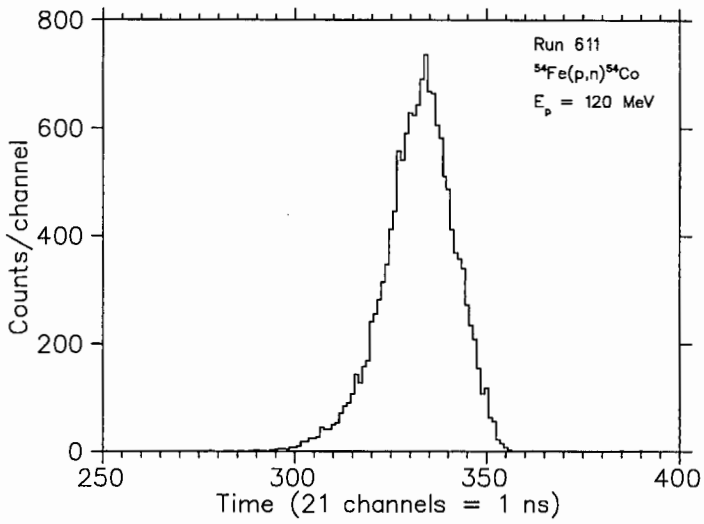

Figure 3.2: A beam pulse time profile obtained using the proton telescope. During this run the pulse had a width of approximately 800 ps.

3.5 The Neutron Detectors

The long flight paths (typically $\geq$100 m) necessary for good energy resolution result in small solid angles. Large detectors help to increase the solid angle but have poorer intrinsic time resolution. The solution employed in this experiment was to have an array of six detectors, each of which with adequate time resolution, which put together had sufficient solid angle to achieve a reasonable detection rate. Each detector consisted of a large slab of NE102A scintillator of dimensions 10 cm by 10 cm and length 60 cm coupled at each end by a tapered perspex light-guide to Hamamatsu R329 photomultiplier tubes with E934 bases. The entire detector was sealed inside a light-tight aluminium box. Two anode signals were taken from each photomultiplier tube, one for timing information and the other for pulse size information. The detectors were stacked on top of each other into a wall which could be orientated either transversly or longitudinally to the incoming neutrons. The former arrangement presented the larger solid angle to the incoming neutrons, but allowed more neutrons to pass through undetected or to deposit only a tiny fraction of their energy in the detector. The longitudinal arrangement presented a smaller solid angle but had a greater efficiency of detection for a neutron that entered it. Section 3.13 discusses the resolution achieved by these two geometries.

The detector hut was a converted shipping container large enough to contain the detectors, racks of NIM and CAMAC electronic modules, a computer terminal and two to three experimenters. It was equipped with airconditioning to keep the internal temperature from rising to the level where signal processing time was significantly affected. Although it was stationed at a fixed location during acquisition, it could be lifted onto a trailer and moved to a new location at a different flight path length or angle to the incoming proton beam. During acquisition of the data presented in this work the hut was situated at distances from 90 m to 174 m from the target and at 0° to the incoming proton beam and the beam swinger was used to achieve the whole measured angular distribution. Also inside the hut were the NIM electronic modules used to process the detector signals and the CAMAC interface. The time and pulse size information as well as register bits detailing which detectors had fired and the event trigger information were fed via the CAMAC interface to the acquisition computers in the data room inside the main cyclotron building.

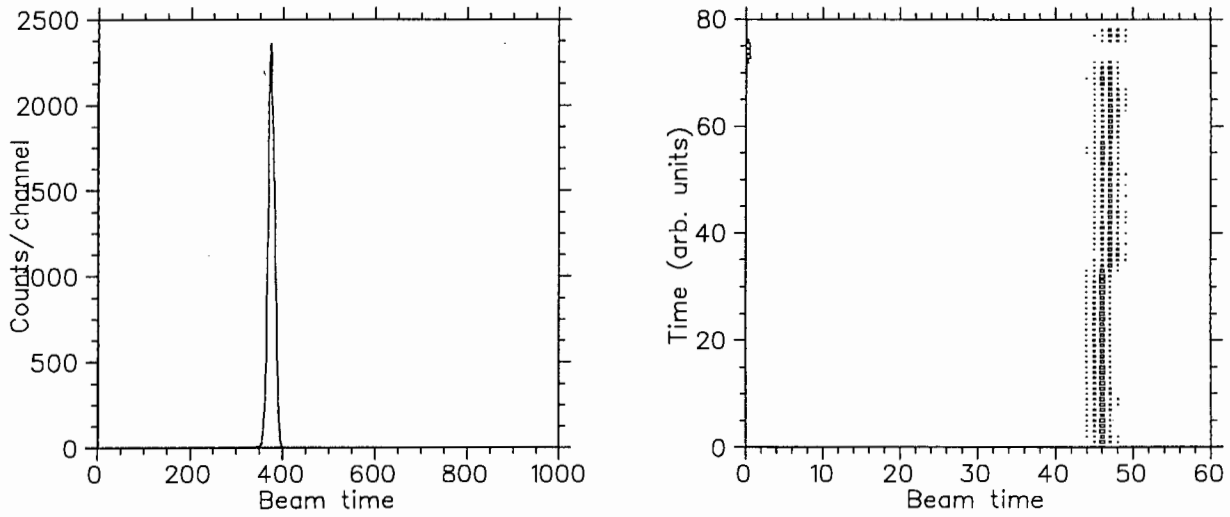

Figure 3.3: A typical beam time spectrum (a) acquired during a run and (b) plotted as a function of run time. The right hand figure shows a phase shift approximately halfway through the run and a short period near the end of the run during which the beam went off.

3.6 Data Acquisition

After electronic signal processing (described below) the data signals were fed via CAMAC through a Micro-programmable Branch Driver (MBD-11) to a VAX 11/730 acquisition computer running the XSYS [58] data acquisition software under the VMS operating system. Later, offline data analysis was done using the XSYS software and custom-written FORTRAN analysis programs. Data were stored on 9 track 6250 bpi magnetic tapes. Typical 4 hour runs filled between 5% and 30% of a tape depending on the beam current on target. The data presented in this work were acquired over a period from November 1990 to March 1993.

ADC conversion and computer processing of each event were the largest contributors to system 'dead time' during which valid events could not be recorded. This had to be taken into account or reaction cross sections would appear smaller than they really were. A busy signal was produced by the hardware during these periods and was used to inhibit data acquisition and to veto the current integrator. The accumulated charge recorded for any particular run was thus automatically corrected for hardware dead time. A monitor of this effect was also established by recording a pulser with and without a veto from the busy signal. During most of the acquisition dead time amounted to less than 1%. During the runs with the lithium target, where a much greater data rate was recorded, the dead time was between 2% and 5%.

3.7 Threshold Determination

Most neutrons detected in the detectors deposited very little of their full energy in the scintillator. This was the reason that time-of-flight rather than energy deposition was used to measure their energies. It meant, though, that the energy threshold had to be set rather low in order not to exclude most of the neutrons of interest. It was necessary to know where this threshold had been set in order to know the cutoff neutron energy visible in the recorded data. This was important for the later removal of low-energy wraparound neutrons from the high energy spectra. The ever-present cosmic ray muon background was utilised for this purpose. At sea level these muons have a mean energy of 2 GeV and are minimum ionizing particles which deposit 2.23 MeV/cm

inside the detectors [59]. The muons passed through the detectors in straight lines which could be reconstructed from the recorded information and the total energy deposited inside the detectors could then be calculated and used to calibrate the pulse size spectra. Assuming a linear response of the scintillator this could be extrapolated to the neutron threshold. Doing so gave threshold values ranging from ~35±5 MeVee to ~55±5 MeVee.

3.8 Detector Resolution

The intrinsic time resolution of the detectors was also obtained from the cosmic ray muon data. These high energy particles passed through the detectors in virtually straight lines. The position of interaction in each detector was obtained from the difference in times between the signals observed by the phototubes at each end of the detector. An unknown time offset for each detector, caused by unequal cable lengths and electronic module processing times, resulted in the muon path through the detector stack appearing not to be a straight line. In addition, any small physical misalignment of the detectors relative to one another would also have result in apparent non-straight paths. A large number of such events were combined in a fitting procedure in which the time offsets were allowed to vary as parameters, and the values of these offsets which allowed the best reconstruction of the straight line paths were determined. The difference between the reconstructed paths and straight lines was then a measure of the intrinsic resolution of the detectors. For each such fit these differences were accumulated into histograms. The width of these histograms, obtained by the fitting of a gaussian curve to each, was then the intrinsic time resolution of the detectors. A typical example, shown in figure 3.4, has a mean FWHM of 450 ps. Best values of as little as 300 ps were obtained at times. Variations in the resolution reflect degradation of the optical contacts within the detectors and the subsequent re-greasing thereof, as well as changes in cables and electronic modules between sets of runs.

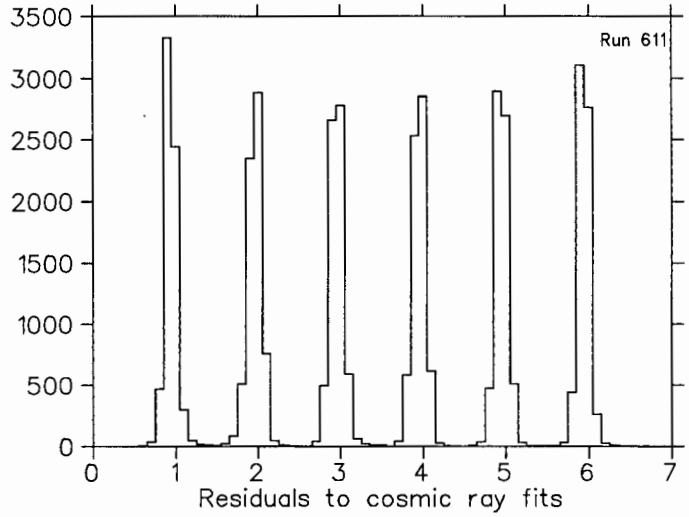

Figure 3.4: Typical residuals of the straight line fits to the cosmic ray paths for the six detectors during run 611. Fits of gaussian curves to these residuals give the widths which are the measure of the intrinsic detector resolution. The bin width of the histograms is 250 ps giving a mean FWHM for the residuals shown here of 450 ps.

3.9 Detector Efficiencies

Because the cross section for electrically neutral particles to scatter a charged particle in the detectors is low, very few of the reaction neutrons impinging on the detector were actually observed. The efficiencies of the detectors for neutron detection need to be well known if the reaction cross sections are to be calculated from the observed yields.

The ^{7}Li(p,n)^{7}Be (gs + 0.43 MeV) reaction provided reference cross sections (see Table 3.1; values are from ref [60] and references therein) as well as a good rate of neutrons. A short (~5 min) run with the lithium target before and after every long run on the targets of interest provided a neutron yield which could be compared with the known cross section to enable calculation of the absolute detector efficiencies at all times during data acquisition. For each lithium run the summed yields of the ground state and first excited state were used to calculate the ratio $Ye_0A/Q\Delta\Omega\delta N_A$ from eq. 4.2. The efficiency, ϵ, was then this ratio divided by the reference cross section. A full treatment of the detector efficiency is given in reference [59]. Because the neutron thresholds were not reset at every energy change there was considerable variation in the detector efficiencies with beam energy. With the transverse detector orientation the efficiencies ranged from 1% to 3%. The longitudinal detector arrangement had a higher efficiency because of the greater depth presented to an incoming neutron. Typical efficiencies for this arrangement were between 10% and 12%. These efficiencies

E_p (MeV)	$d\sigma/d\Omega$ (mb/sr)
90	33.2 ± 3.0
120	37.7 ± 3.1
160	38.2 ± 3.4
200	38.8 ± 2.7

Table 3.1: Reference 0° laboratory cross sections for ^{7}Li(p,n)^{7}Be (gs + 0.43 MeV).

are the absolute detection efficiencies at the neutron energies corresponding to the mean energy of the lithium ground state and first excited state. Because of differences in Q–values between lithium and the other targets of interest, and because the analyses extend up to excitation energies of the order of 20 MeV, it is necessary to know the efficiencies as a function of incident neutron energy. The importance of such energy dependent corrections to the efficiencies has been emphasised by several workers in this field [61]. The absolute efficiencies are comprised of the intrinsic detector efficiencies and the fraction of neutrons which are not absorbed by the various media between the target and detector. Both of these are energy dependent. The former was modelled with the Monte Carlo code of Cecil, Anderson and Madey [62] to generate intrinsic detector efficiency curves as a function of incident neutron energy for the two detector geometries at various pulse size threshold values. The transmission factors were calculated as a function of neutron energy and flight path length for the various absorbtive media through which the neutrons had to pass using neutron cross sections from McLane *et al.* [63]. The calculated absolute efficiencies, which are the product of these two effects and are plotted in figure 3.5, were then normalised to the measured ^{7}Li(p,n)^{7}Be (gs + 0.43 MeV) points before being used to calculate cross sections from the extracted neutron yields. It was found that the exact value of the pulse size threshold had little effect on the shape of the energy dependence of the efficiency. Because of the normalisation to the lithium points the uncertainty in the particular pulse size threshold settings was thus of relatively minor importance. Over the excitation energy range of interest the efficiencies displayed a variation of just a couple of percent for the 200 MeV incident proton energy, but a variation of up to 55% for the 90 MeV points.

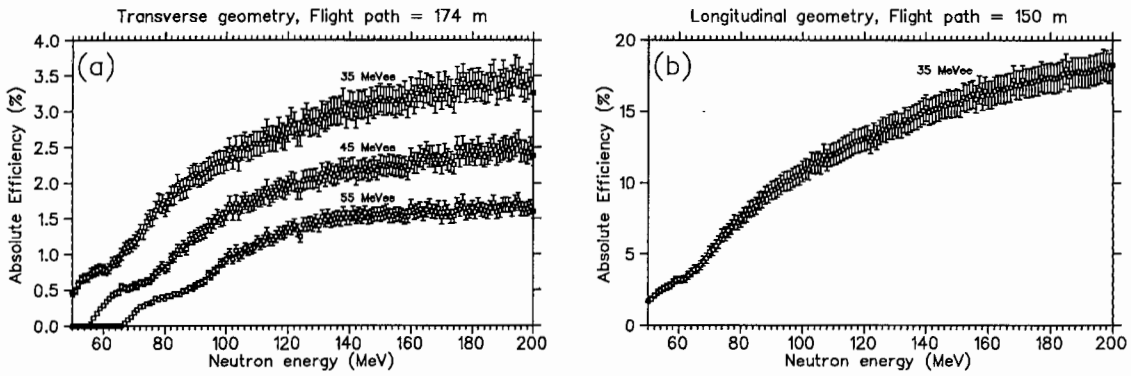

Figure 3.5: Calculated efficiencies for (a) the transverse detector orientation at pulse size threshold values of 35, 45, and 55 MeVee, and (b) for the longitudinal detector orientation at a neutron threshold of 35 MeVee.

3.10 Temperature Effects On Timing Measurements

The signal cables between the detector hut and the acquisition hardware and computer inside the cyclotron building were of the order of 200 m long and lay above ground on the field outside the building. It was noticed that the temperature variation between night and day affected the signal propagation speed in the cables. The variation in propagation times was of the order of a couple of nanoseconds; enough to affect the time resolution of the experiment. To correct for this affect the data runs were split into short sections (especially during the morning and evening periods when the effect was greatest) for which the effect was negligible. These sections were then overlapped and added in the later software analysis.

3.11 Acquisition Electronics

Schematic diagrams of the signal processing electronics are presented in figures 3.6 to 3.11. For simplicity various fan-out modules and delays are not included in the diagrams.

3.11.1 Proton Telescope

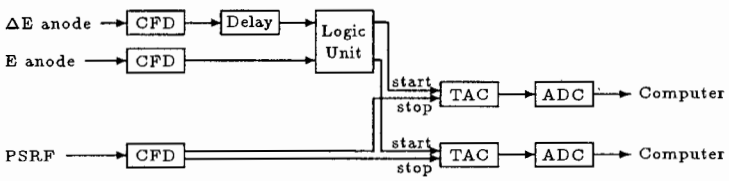

Figure 3.6: The proton telescope circuitry.

The proton telescope consisted of a ΔE and an E detector. The anode signals from each were fed through constant fraction discriminators to a logic unit which ensured a coincidence between the two detectors, thus eliminating all events not originating in the target (figure 3.6). The CFD units allowed energy windows to be set on the anode signals thereby selecting only the fastest, high energy, elastically scattered protons. A small delay in the ΔE signal ensured that it arrived at the logic unit after the E signal, thus setting the timing of the coincidence. This was done

because a tighter window could be set around the ΔE signal than around the E signal. The beam proton signal from the coincidence then started a TAC which was stopped by the discriminated PSRF signal. The TAC output was fed out to an ADC and then into the acquisition computer producing a time spectrum which reflected the time structure of the beam pulses. A second TAC was operated in the same manner but with a longer time range (greater than the interpulse period). This produced a low resolution time spectrum which showed whether any breakthrough occurred in the pulse selector. The event trigger which caused the computer to read the beam time data was independent of the beam time signal. The data simply sat and waited in the ADC for the next trigger which came from a pulser set to generate triggers at a convenient rate. A typical, fixed sampling rate of 1 Hz was employed.

3.11.2 Dead Time and Current Integrator

A measure of the system dead time was obtained by feeding the output of a pulser into two scalers (figure 3.7). One scaler counted continuously while the other was vetoed by the computer busy signal. The difference in scaler counts was then proportional to the dead time. This was used merely as a monitor of the effect. Actual correction for dead time was done by vetoing the current integrator output by the same computer busy signal before being read by a scaler. In this way the accumulated charge was automatically corrected for dead time while being acquired. In retrospect, it may have been better to have counted the number of event signals generated and thoses counted by the computer, and to have inferred the dead time from the difference. This would have eliminated any possible time correlations.

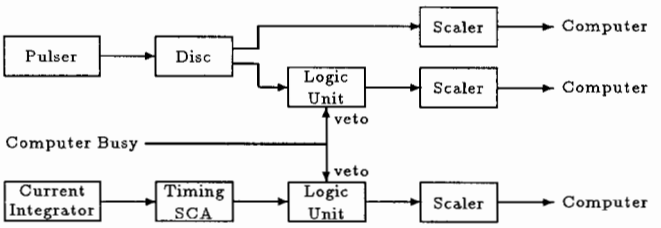

Figure 3.7: The dead time and current integrator circuitry.

3.11.3 Triggers

Two different types of events were observed in the neutron detectors; neutrons from the target and background cosmic ray muons. The latter were recorded because they were of great use in calibrating the detectors and the continuous monitoring of detector performance. Each type of event had to generate a distinguishable trigger so that they could be separated during the data analysis. The neutron trigger (figure 3.8) was generated by fanning in the two anode signals from the ends of each detector. The resulting signals from the six detectors were then fed into a 6-channel discriminator and the sum was fed to another discriminator, the output of which was the neutron trigger. A neutron event was then defined by an event in any one of the six detectors whose amplitude was above the discriminator threshold described in section 3.7. Cosmic background events of interest, on the other hand, were restricted to muons which pass through all six detectors. These events deposited much less energy in each detector than most neutron events and so the cosmic threshold was set much lower than the neutron threshold. The anode signals from the two ends of each detector were fed through constant fraction discriminators and into a meantimer (figure 3.9). The six meantimer outputs corresponding to the six detectors were fed into a 6-fold

coincidence to select only those muons which passed through all six detectors. The output of the coincidence was then the cosmic trigger. The event trigger, which caused the computer to read in an event, was the logical 'OR' of these two triggers. It was formed (figure 3.10) by feeding the two triggers into a logic unit which was set to a coincidence level of one and which was also vetoed by the computer busy signal. The resultant event trigger signal was also used as the common start for the TDCs and as the gate for the ADCs.

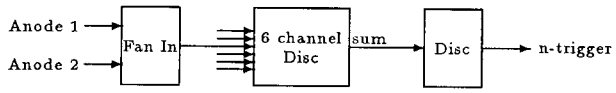

Figure 3.8: The neutron trigger.

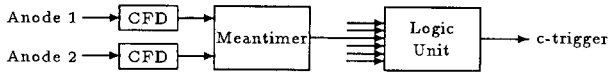

Figure 3.9: The cosmic trigger.

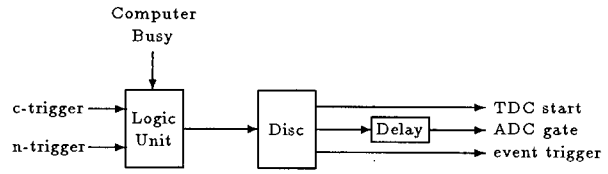

Figure 3.10: The event trigger.

3.11.4 ADC and TDC Electronics

The anode signal from the detectors went via a 0–10.5 dB attenuator to the ADCs from where it was read by the computer (figure 3.11). LeCroy 2249A charge sensitive ADCs were used and the term 'pulse size' used here thus refers to the charge in a pulse within the ADC gate. A 200 ns delay allowed the ADC gate to be created before the signals reached the ADCs. The TDCs, which were set to a range of 250 ps/channel, had a common start which was taken from the event trigger, thus ensuring that they only operated on a valid event. They were stopped by the delayed timing signals from each detector phototube and one channel was stopped by the beam time (PSRF) signal. The neutron time-of-flight was then calculated from these times.

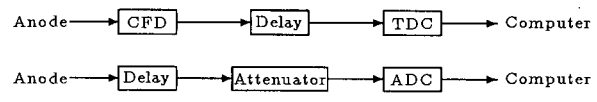

Figure 3.11: The time (top) and pulse size (bottom) signals.

3.12 Gain and Threshold Matching

As described in section 3.11 the neutron trigger was obtained by summing the anode signals from the two ends of each detector in a fan-in module and feeding this signal to a discriminator at which

the neutron threshold was set. Since the neutron could interact anywhere in the scintillator, one of the two anode signals could well be small while the other one was large. In practice this meant that the neutron trigger could come from just one of the two phototubes. As a result the pulse size spectrum from each phototube looks like the solid curve in figure 3.12. It is composed of two separate parts, shown by the dashed curves. If this represents the pulse size spectrum for phototube 1, say, then the narrower dashed curve represents neutrons detected in the detector for which the trigger comes from phototube 1. These neutrons all have pulse sizes in phototube 1 which are above the threshold which is the left hand edge of the narrower dashed curve. The broad dashed curve is comprised of neutrons for which the trigger essentially comes from phototube 2. In this case the pulse size measured in phototube 1 may be above or below the threshold.

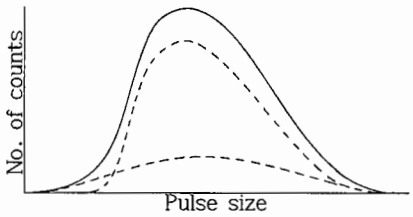

Figure 3.12: A sketch of the neutron pulse size spectrum for one phototube showing its two components.

The phototube gain and neutron threshold matching were therefore done together. The first step was to let phototube 1 be the standard to which the other gains were matched and detector 1's threshold be the standard to which the other detectors were matched. The anode signal from phototube 2 was then removed from the fan-in and a pulse size spectrum for phototube 1 was acquired. This looked like the narrower dashed curve of figure 3.12 and clearly showed the position of the threshold. Then spectra for the other detectors were acquired, each with only one phototube input to their respective fan-in modules. Their threshold settings were then visible and could be adjusted to match that of detector 1. Once the thresholds had been matched, it was possible to match the phototube gains. The anode signal from phototube 1 was removed from the fan-in and replaced by the anode signal from phototube 2. The pulse size spectrum for phototube 2 was then acquired for an equal time to that of phototube 1 previously and should have contained approximately the same number of events if the gains were matched. If not, the high voltage to the phototube was adjusted and the process repeated until they were matched. This was then repeated for the other phototubes in the detector stack.

3.13 Energy Resolution

The ultimate check on the resolution of the experiment was by looking at the data itself, and specifically at the width and separation of peaks of known energy. Two examples are shown in figures 3.13 and 3.14. These spectra, taken at a beam energy of 120 MeV, both show a resolution (FWHM) of ~300 keV for the clearly separated low energy states. The spectrum in figure 3.13 was taken with the detectors in the transverse orientation and the spectrum in figure 3.14 was taken using the longitudinal orientation. In general, no significant differences in energy resolution were observed between the two arrangements. The flight path length was a little shorter for the longitudinal arrangement to partially compensate for the reduced solid angle (150 m vs 174 m). Slightly better resolution would be expected from the longitudinal setup with identical flight paths. At beam energies of 200 MeV the resolution deteriorated to ~700 keV.

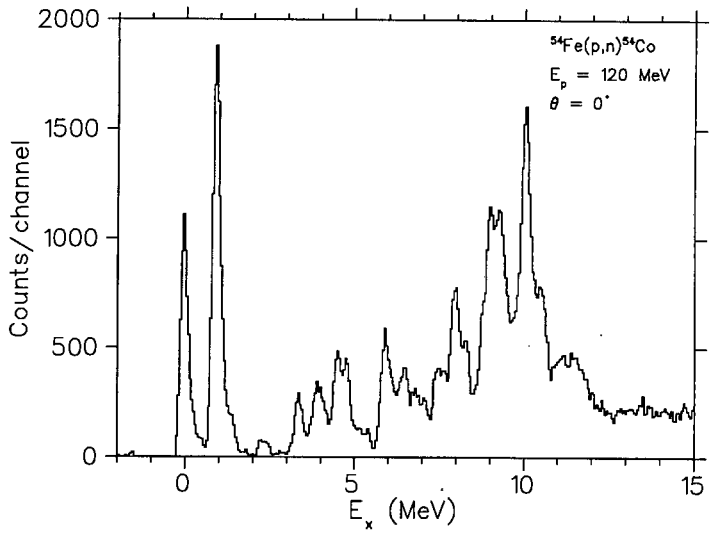

Figure 3.13: A typical ^{54}Fe spectrum taken with the transverse detector arrangement. The ground state and first excited state at 0.94 MeV have a FWHM resolution of about 250 keV.

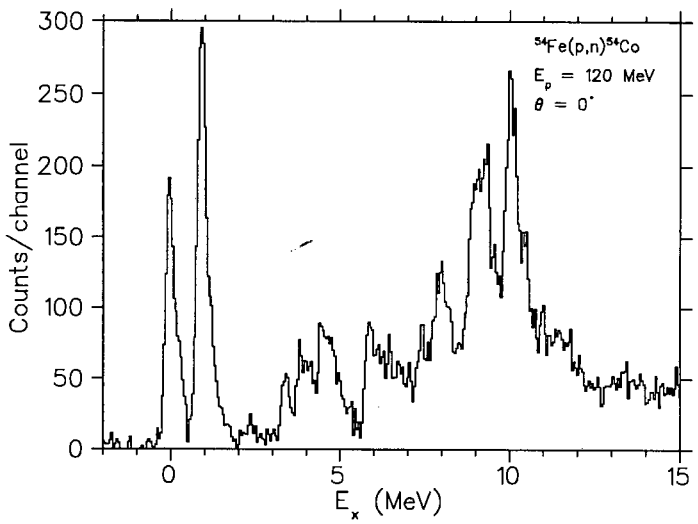

Figure 3.14: The same as figure 3.13 except acquired using the longitudinal detector orientation. The FWHM of the low energy peaks is about 300 keV.

Chapter 4

Methods of Data Analysis

4.1 The TOF Spectra

The first step in the analysis of the neutron data was to compile the complete time-of-flight (TOF) spectrum for each beam energy and detection angle. Data acquisition runs were usually no longer than four hours each to minimise the effects of signal propagation speed due to temperature fluctuations and phase drifts with respect to the machine RF signal. Despite this restriction on the length of the runs, some did have noticeable phase drifts or were subject to RF phase adjustments by the cyclotron operators and were later split up into shorter sections for which the drifts were negligible. A few runs also had bad sections during which problems with the proton beam were experienced. These sections were omitted from the analysis. In addition, the detector stack was comprised of six independent detectors, each of which had a slightly different electronic processing time and whose times were recorded by different TDCs with slightly different calibration factors (see figure 4.1). Each of the many TOF spectra were therefore first normalised to a common scale of 4.00 ch/ns and then shifted into alignment with each other before being added together into a single spectrum comprising all the data for a particular beam energy and detection angle.

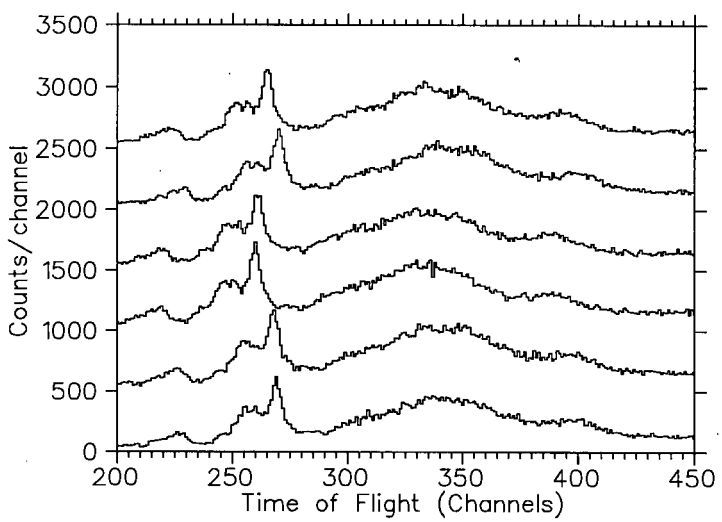

Figure 4.1: The TOF spectra for the six neutron detectors acquired during a typical 0° ^{51}V run at $E_p = 160$ MeV. The spectra have been shifted vertically relative to each other. The horizontal scale is in channels where 4 ch $\approx$ 1 ns. The different time offsets and TDC scales are apparent.

A pulse size cut was applied to the data comprising the TOF spectra in an attempt to eliminate cosmic events. Since the cosmic muons deposited a characteristically smaller amount of energy in the detectors than the neutrons (see figure 4.2) a software cut safely rejected most of the cosmics without rejecting neutrons. In practice this resulted in the rejection of <2% of the total number of events. Examination of the rejected events (see figure 4.3) showed a flat time distribution as expected of cosmic events which have no relation to the beam PSRF signal. This also demonstrated that these events would, even if not rejected, have had little effect on the yield of the discrete states since they would be removed along with the wraparound background (see section 4.2).

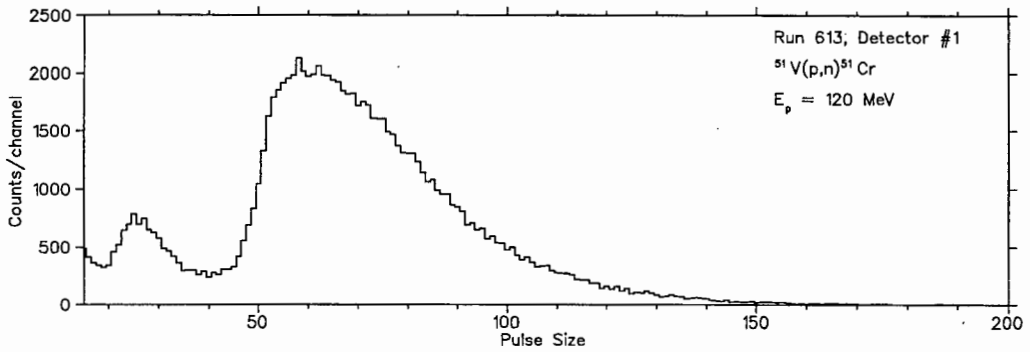

Figure 4.2: A typical pulse size spectrum showing the cosmic events in the left peak and the neutron events in the right peak. A pulse size cut of 40 channels would be applied here to separate them. The neutron threshold corresponds to ~channel 50.

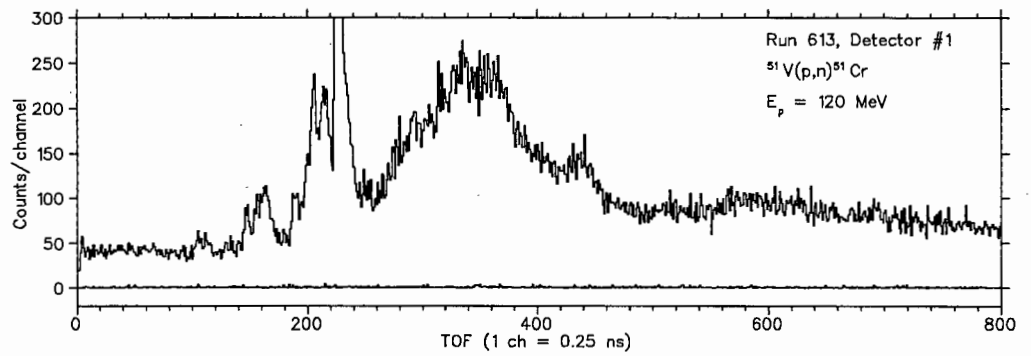

Figure 4.3: A TOF spectrum (upper curve) and the cosmic events which would be rejected from it (lower curve) either by them firing the cosmic trigger or by having pulse sizes below the cut indicated in figure 4.2. The rejected cosmics show the expected uniform time distribution. The upper curve has been shifted vertically by 20 counts for clarity.

The neutron flight times between the target and detector were not measured directly. Rather they had to be calculated from the time an event was seen in the detector and from the beam PSRF signal. Since the flight times were of the order of a microsecond or two and the interpulse period was of the order of a quarter of a microsecond, there was no way of telling from exactly which beam pulse any particular event originated. Instead it was only possible to measure a relative time between the detection of an event and the closest PSRF signal. This was not a problem because what was of interest was the relative difference in speeds (and hence kinetic energies) of neutrons from the transitions to the various states in the residual nucleus. With the knowledge of at least one or two known peaks in the spectrum, it was possible to convert the time-of-flight spectrum to an energy spectrum even though it was on a relative time scale.

The calculation of the neutron flight times depended on the detector arrangement. For the transverse arrangement, where the neutrons arrived in a direction perpendicular to the long axis of the detectors, the arrival time was taken to be the mean time from the two phototubes at either end of the detectors. This eliminated any time variation due to the position of an event along the scintillator's long axis. There was still a time uncertainty due to the lack of knowledge of the depth in the scintillator at which the interaction occurred. This was effectively an uncertainty of 10 cm in the flight path length and corresponded to a time uncertainty of ~0.5 ns for the fastest neutrons and ~0.8 ns for the slower neutrons. However, the latter make up the continuum of the spectrum where the resolution is not so important.

The calculation of the flight times for when the detectors were placed longitudinally to the beam was more complex. Since the flight path length to the point of interaction then varied by up to the scintillator length of 60 cm, all the times were reduced to times to the middle of the detector. Consider a neutron interacting at a distance x from the centre of the scintillator (figure 4.4). The time, t_i', from the neutron leaving the target to when the scintillation is seen by phototube i is

$$t_i' = t_i - t_{psrf}$$

where t_i is the detection time measured by phototube i. This can be expressed in terms of t_x, the flight time of the neutron to the point of interaction, t_d, the light transit time across the length of the scintillator, and v_e, the effective light speed in the detector

$$\begin{aligned} t_1' &= t_1 - t_{psrf} = t_x + \frac{1}{2}t_d - \frac{x}{v_e} \\ t_2' &= t_2 - t_{psrf} = t_x + \frac{1}{2}t_d + \frac{x}{v_e} \end{aligned}$$

Subtracting one from the other yields

$$x = \frac{v_e}{2}(t_2 - t_1)$$

while adding them gives

$$\begin{aligned} t_x &= \frac{1}{2}(t_2 + t_1) - \frac{1}{2}t_d - t_{psrf} \\ &= \frac{1}{2}(t_2 + t_1) - \frac{x_0}{v_e} - t_{psrf} \end{aligned}$$

where x_0 is half the length of the scintillator. Reducing the interaction point to the middle of the scintillator at position $x = 0$, the neutron flight time becomes

$$\begin{aligned} t_0 &= t_x - \frac{x}{\beta_n c} \\ &= \frac{1}{2}(t_2 + t_1) - \frac{x_0}{v_e} - t_{psrf} - \frac{v_e}{2\beta_n c}(t_2 - t_1) \end{aligned}$$

where β_n is the neutron speed divided by c. All times are recorded in channels which have been normalised to 4.00 ch/ns. Therefore the second term must be multiplied by 4 to convert it to channels. Doing this, and replacing v_e by $\beta_e c$ gives

$$t_0 = \frac{1}{2}(t_2 + t_1) - \frac{4x_0}{\beta_e c} - t_{psrf} - \frac{\beta_e}{2\beta_n}(t_2 - t_1) \tag{4.1}$$

This calculation was done for each event as it was read in, in order to assign it to its proper position in the time-of-flight spectrum. At the time it was done, therefore, it was not known exactly what

Figure 4.4: A scintillator arranged longitudinally to the incoming neutrons.

β_n for each event was. Therefore it was assumed for all events to be equal to the value of β_n for neutrons arising from the transition to the ground state of the residual nucleus. This approximation was very good for the high energy neutrons which populate the discrete states of the spectrum and for which it was important to have good time resolution. Since the term involving β_n is small, it was found that t_0 was in any case rather insensitive to the exact value of β_n.

The effective light speeds inside the detector varied slightly from detector to detector and with time. This was largely due to the quality of the optical coupling between detector components, the quality of the wrapping of the scintillators in reflective foil, and the phototube response time. The values of the effective light speeds, from which the β_e values are obtained, came from information contained in the differences between the times measured at the two ends of each detector. For events occurring at all positions along the length of the scintillator the time differences gave rise to spectra which look like a box. The width of this box was equal to twice the effective light travel time across the detector since it varied from $(t_1 - t_2)$ to $(t_2 - t_1)$. Figure 4.5 shows an example of a time difference spectrum for a detector taken while orientated longitudinally to the incoming neutrons. The rectangular box was the shape fitted to the spectrum and its width was used to calculate the β_e for that detector. Little variation between detectors was found in these values. The average value was found to be $\beta_e = 0.533 \pm 0.018$ which corresponds to a speed of 15.9 cm/ns. Tests also showed that the resolution of the time-of-flight spectra was not very sensitive to the exact value of β_e.

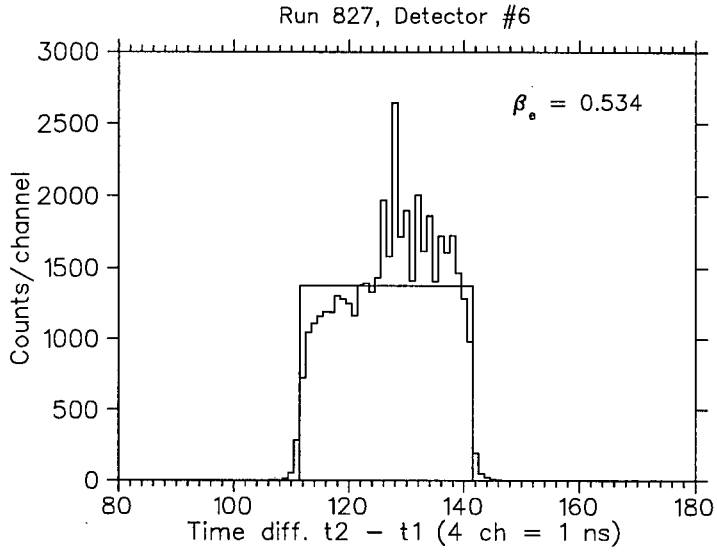

Figure 4.5: A typical spectrum of differences in times between the two ends of a detector. The fitted rectangular box gives the width of the spectrum which is used to calculate the effective beta, β_e, of light in the detector. The non-flat top of the spectrum is due to more neutrons being absorbed near the front end of the detector than at the back end.

4.2 Wraparound Removal

Once the time-of-flight spectrum had been created, it was possible to attempt to remove the contribution from slow, wraparound neutrons from previous beam pulses. The estimated neutron threshold (see section 3.7) corresponded to neutrons moving slowly enough to arrive at the target simultaneously with fast neutrons from two beam pulses later. A spectrum of three consecutive pulses was therefore created by shifting a copy of the TOF spectrum by exactly one and two times the interpulse period (figure 4.6a). The vertical arrow at the right hand side of figure 4.6a represents the approximate position of the neutron threshold for neutrons originating in the first (left hand) beam pulse spectrum. Therefore the removal procedure had to consider wraparound components from the previous two pulses. Examination of figure 4.6a shows neutrons in the excitation region below the ground state (for example between channels 2000 and 2250). Since no neutrons could have traveled faster than those from the transition to the ground state, these must be slow neutrons from previous pulses. It is also clear that this region of the spectrum joins smoothly with the tail of the previous pulse (channels 1700 to 1900). The wraparound contribution was then estimated by fitting a curve through the data in these two regions. This curve was comprised of three components; a curve representing the shape of the tail of the spectrum (curve c) plus two identical curves from the previous two pulses (curves b and a). The sum of these three components (curve d) was then required to fit the data in the abovementioned two intervals. It was found that a decaying exponential curve shape resulted in good fits to the data.

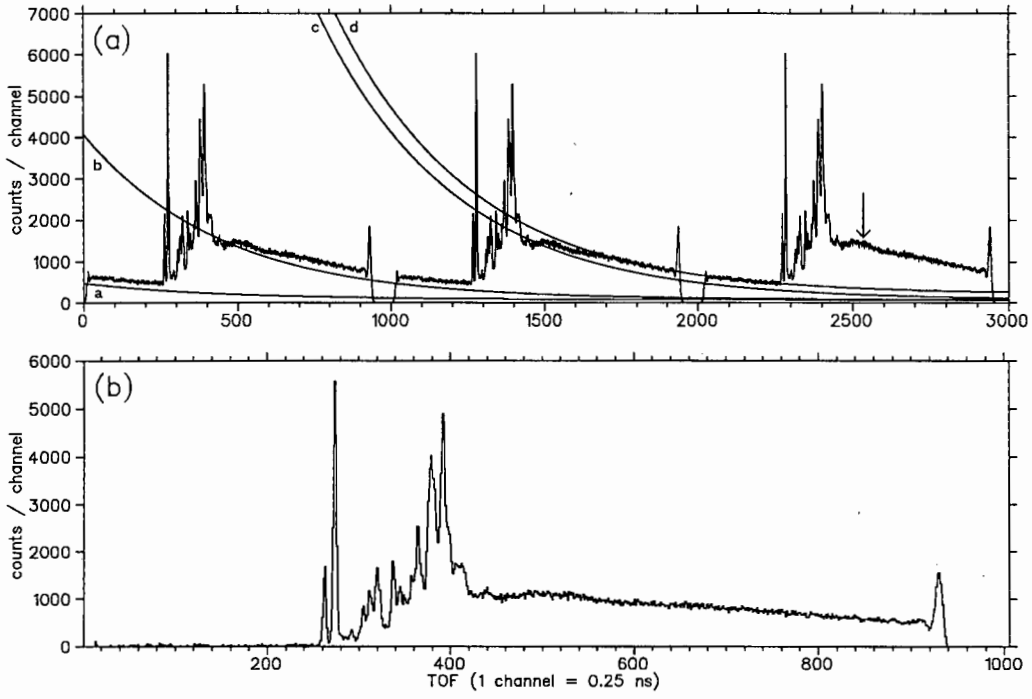

Figure 4.6: (a) TOF spectra for three consecutive beam pulses. See the text for an explanation of the curves fitted for wraparound removal. (b) The TOF spectrum after removal of the wraparound neutron contribution. The data shown are for ^{54}Fe(p,n)^{54}Co at 0° and $E_p = 160$ MeV.

Once the fit had been determined the wraparound contribution (curve d) was subtracted from the TOF spectrum. Figure 4.6b shows the TOF spectrum after removal of the wraparound. It corresponds to the right hand spectrum of figure 4.6a minus curve d. As expected, there is now effectively no data to the left of the ground state peak at ~channel 260. Previous experiments done at the Indiana University Cyclotron Facility (IUCF) employed a storage ring known as the 'stripper

loop' to increase the interpulse period to approximately 2 μs [10]. With this long period very clean spectra were obtained. A comparison of the spectrum in figure 4.6b with, for example, figure 4.7 which is an ^{54}Fe(p,n)^{54}Co spectrum taken at $E_p = 135$ MeV at IUCF (figure 1 of reference [25]) shows that the wraparound removal procedure described above produced spectra comparable to those obtained using the stripper loop.

In the above figure the peaks at the right hand end of the spectra (~channel 930 in figure 4.6b) are spurious and result from the finite width of electronic pulses in a coincidence unit. They were ignored in the matching of the two fitting regions.

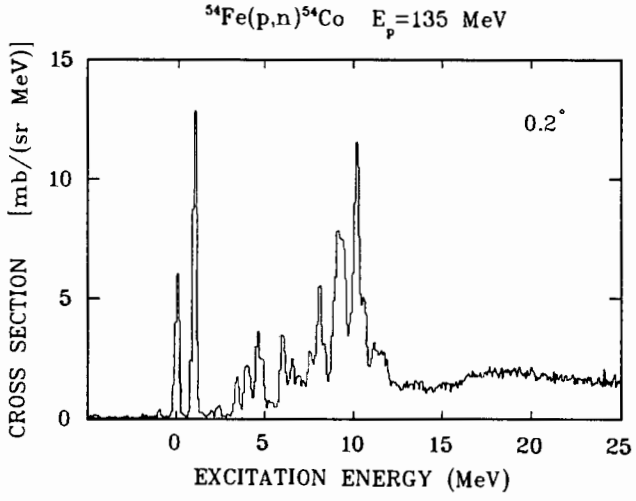

Figure 4.7: An ^{54}Fe(p,n)^{54}Co spectrum taken at 135 MeV at IUCF using the stripper loop to avoid wraparound background (from ref [25]).

4.3 Peak Fitting and Energy Calibration

The deconvolution of the discrete states in the spectra was done in several steps. For ^{51}V and ^{59}Co the IAS sits on top of a number of GT peaks at an excitation energy of approximately 7 MeV. A 'background' was fitted to a small region on either side of the IAS and a single gaussian curve to the IAS itself. An example of this fit is shown in figure 4.8. This peak shape was then fixed for the rest of the fitting procedure. The next step was to fit a cubic polynomial which modeled the continuum part of the spectrum (figure 4.9a). It was constrained to fit the data in two regions; below the ground state peak where the data was effectively zero after subtraction of the wraparound contribution, and to the continuum just above the last visible discrete peaks. Once this had been done this background curve was fixed and retained during successive fits. Examination of the low excitation energy peaks revealed an asymmetric peak shape in some runs. In practice this only applied to ^{54}Fe(p,n)^{54}Co spectra in which the first couple of states are clearly separated and to beam energies of less than 200 MeV for which the resolution was good enough. The low excitation energy peaks in the ^{51}V(p,n)^{51}Cr and ^{59}Co(p,n)^{59}Ni spectra were not strong enough or adequately separated to display an asymmetric shape, even though they are expected to have a low energy tail as in the ^{54}Fe(p,n)^{54}Co case. Once the background curve had been determined, a fit was done to just the first few discrete states to determine the peak shape (figure 4.9b). For most spectra a single, symmetric gaussian shape was assumed, but for those spectra which required asymmetric peak shapes a main gaussian curve plus a smaller gaussian curve on the side was employed. The size and width of the second gaussian relative to the main one and the separation of the two were the main parameters determined by this fit. These were then fixed for the further fit to all the

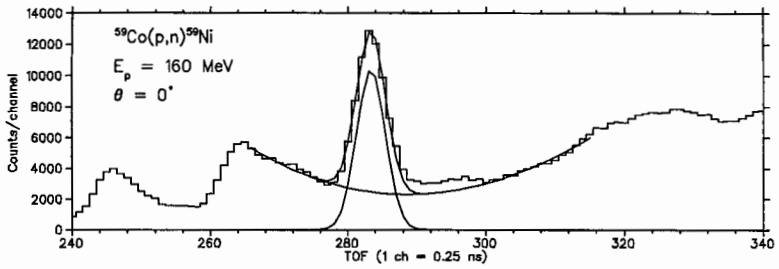

Figure 4.8: An example of a peak fit to the IAS. The data are from ^{59}Co(p,n)^{59}Ni at $E_p = 160\,\mathrm{MeV}$ and $\theta = 0°$.

discrete states, since most of them were too convoluted for accurate shape determination. The final fit used this peak shape for all the discrete state peaks (figure 4.9c).

It was attempted to fit the same peaks, corresponding to the same set of transitions, to the spectra at all angles and beam energies for a particular target nucleus. For most spectra the peak positions were allowed to vary freely and were determined by the fitting procedure. However, for the 200 MeV spectra the resolution was not usually good enough for the discrete states to be distinct from one another and the fitting procedure did not always place the peaks in reasonable positions. In these cases the peak positions, as determined from the lower beam energy spectra, were not allowed to vary during the fit. As long as one peak of known energy could be clearly identified the kinematics allowed the relative positions of the other peaks to be calculated. The peak widths were usually constrained to be the same for all the discrete states in a particular fit, and allowed to vary freely for each peak in the continuum region of the spectrum. It was noticed, though, that in some spectra where the first few discrete states were well separated from the other peaks, they tended to be a little narrower that the rest. The above method enabled good fits to be obtained to all the spectra.

Once the positions of the discrete state peaks had been found it was possible to determine the time-of-flight to excitation energy calibration and to produce an excitation energy spectrum (figure 4.9d). A fit was done in which the excitation energy calibration was varied until it best reproduced the peak positions. The fit was based on a set of distinct peaks visible in each spectrum of a set of spectra taken at different angles but with the same target and beam energy. Two peaks, usually the ground state and one other, were assumed to have well known energies taken from the literature and these were fixed in the fit. The energies of the other peaks were allowed to vary, but with the constraint that they had to be the same for all of the spectra since they corresponded to the same transitions in the target nucleus irrespective of the angle of detection. The peak positions were then calculated from the energies and compared with the positions determined in the peak fitting procedure described above. The energy calibration that gave the best correspondence to the fitted positions of the spectra was then used to produce the final excitation energy spectra for each angle and beam energy.

4.4 The Differential Cross Sections and Transition Strengths

The deconvolution of the discrete states described above also gave the yield of neutrons from each particular transition. This yield, Y, which was the area of each fitted peak and corresponded to the number of neutrons counted in that peak, was then used to obtain the differential cross section for that particular transition. It was combined with the accumulated charge, Q, the solid angle subtended by the detector stack, $\Delta\Omega$, the target surface density, δ, and the detector efficiency, ϵ, to

give

$$\frac{d\sigma}{d\Omega} = \frac{Ye_0A}{Q\Delta\Omega\delta N_A\epsilon} \tag{4.2}$$

where e_0 is the unit charge, A is the atomic weight of the target nucleus, and N_A is Avogadro's number. This quantity is the differential cross section in the laboratory frame and was transformed into the cm differential cross section by multiplying by the relativistic Jacobian $d\Omega_{lab}/d\Omega_{cm}$.

The Fermi transition strength was always assumed to be concentrated in the transition to the IAS and equal to $N-Z$. The Gamow-Teller strengths were calculated from the cross sections as detailed in chapter 2.

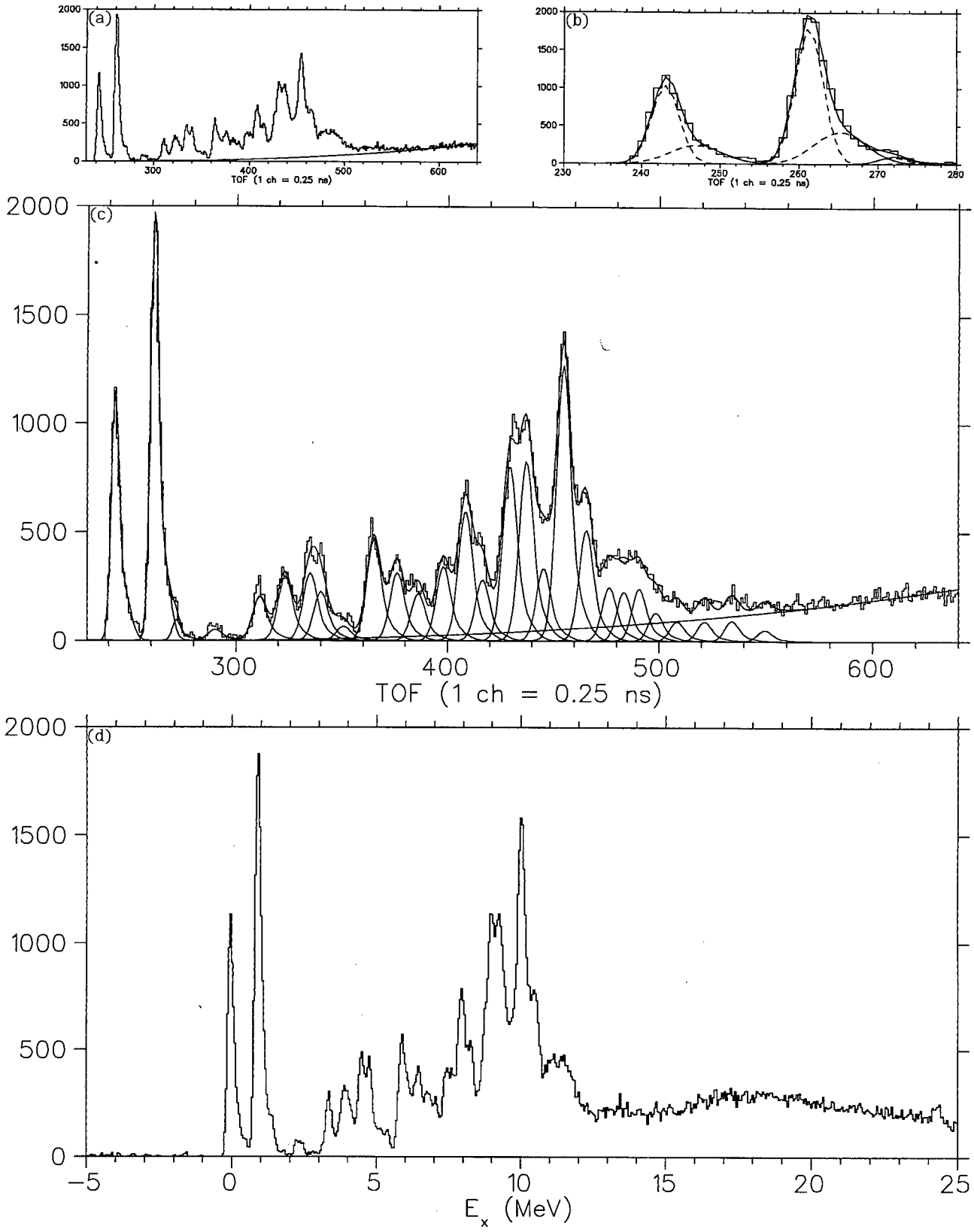

Figure 4.9: An example of the peak fitting and excitation energy calibration procedure. The polynomial fit to the continuum below the discrete states is shown in (a). Figure (b) shows the fit to the first few discrete states for peak shape determination, while (c) shows the final fit to all the discrete states in the spectrum. Figure (d) shows the resulting excitation energy spectrum. The data are for ^{54}Fe(p,n)^{54}Co at 0° and $E_p = 120$ MeV.

Chapter 5

^{51}V(p,n)^{51}Cr Analysis

5.1 Fits to the Spectra

Zero degree time-of-flight spectra for ^{51}V(p,n)^{51}Cr at the four measured beam energies are presented in figure 5.1. These spectra are the complete TOF spectra for a particular dataset. They comprise the sum of all runs in that dataset after those runs had been normalised to a common time scale and each section shifted into alignment with each other as described in section 4.1.

After accumulation into the TOF spectra, the slow neutron wraparound background was removed as described in section 4.2 and a fit was made to the discrete states as described in section 4.3. The IAS of the ^{51}V ground state sits on top of a number of Gamow-Teller states at 6.61 MeV [17, 64] and was fitted first according to the prescription given at the beginning of section 4.3. As can be seen in the spectra, and particularly at 120 MeV (figure 5.2b), the IAS peak has a shoulder on its right hand side which is attributed to a smaller GT peak which is not resolved from the IAS. Any error in the deconvolution of these two states would have resulted in some Fermi strength being attributed to GT strength or vice versa. The IAS peak was fitted to the symmetric region of the peak, excluding the right hand shoulder, and resulted in good fits with small reduced chi squares in all cases. Thus it is believed that any error in the deconvolution of Fermi and GT cross sections was small, and would in any case have had a very small effect on the total GT cross section. The possible systematic error in the IAS fit would be due to incorrect determination of the background GT yield. This was determined by fitting a polynomial to a small region on either side of the IAS peak. Since the spectrum is not completely smooth on the two sides of the IAS peak, there is some uncertainty in the shape of this background. This uncertainty is small at low beam energies where the IAS peak is a large peak on a small GT background but larger at higher beam energies where the situation is reversed. At the higher beam energies the IAS peak yield is smaller which results in a larger fractional error, but the decreased resolution results in a smoother spectrum and consequently less uncertainty in the determination of the GT background. Combining these effects it is estimated that the systematic error on the extracted yield of the IAS peak ranges from 5% at 90 MeV to about 20% at 200 MeV. This would translate to an uncertainty of at most 1% in the total GT cross section. Once fitted, the IAS peak fit was fixed while all the other peaks were fitted. Selection of the peaks to fit was made on the principle of using as few peaks as possible to adequately reproduce the discrete part of the spectra. The same set of peaks was used to fit the spectra up to E_x = 18 MeV at all angles and beam energies for the particular target. In order to obtain good fits to the ^{51}V spectra it was necessary to fit 22 peaks to the data. The results of the wraparound removal and the fits to the 0° data are shown in figure 5.2. The ground state peak and the IAS at 6.61 MeV were then used to determine the time-to-energy calibration and to convert the TOF spectra to excitation energy spectra as described in section 4.3. The uncertainty in the energy calibration is estimated to be less than 100 keV.

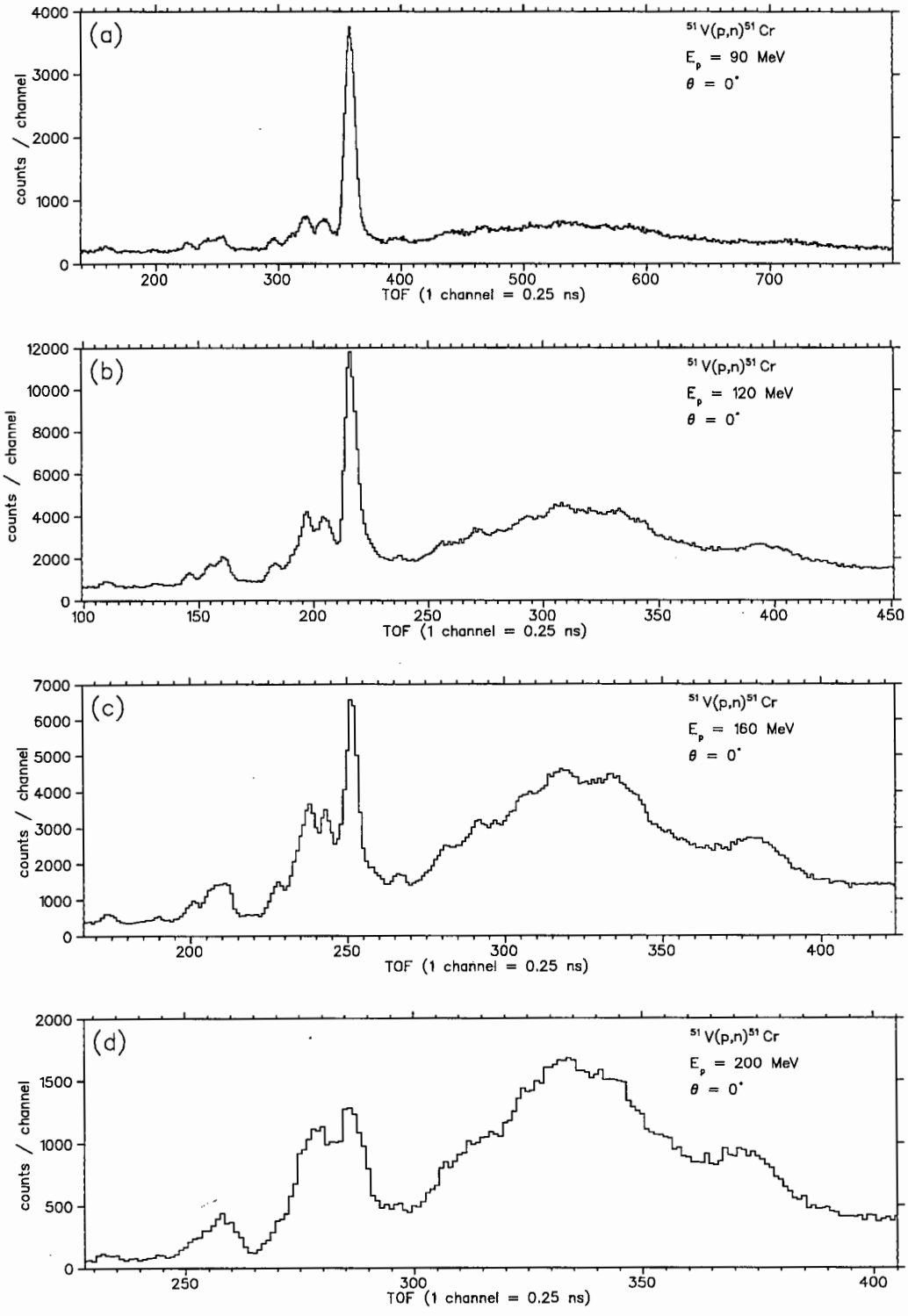

Figure 5.1: The ^{51}V(p,n)^{51}Cr TOF spectra at beam energies from 90 to 200 MeV.

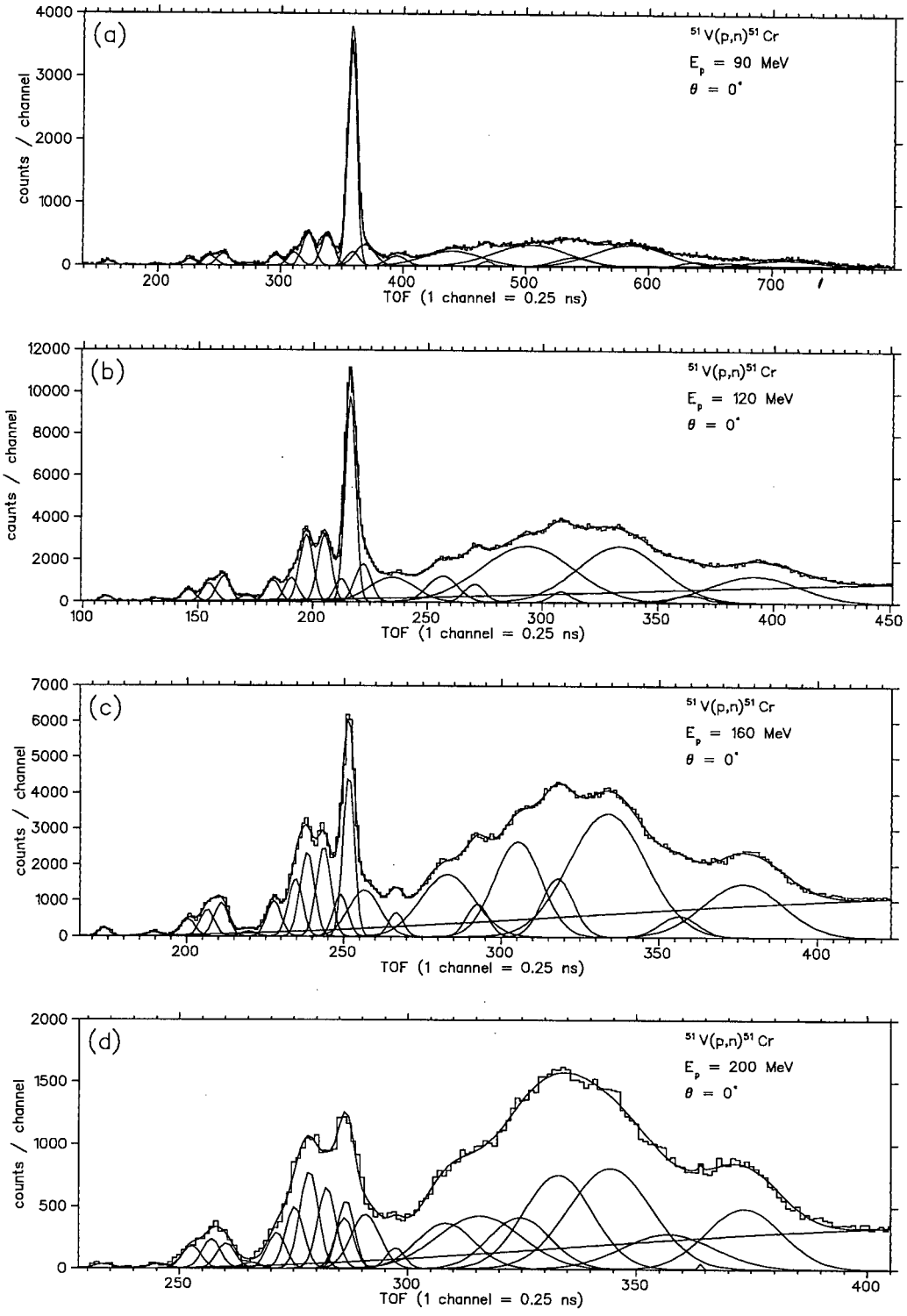

Figure 5.2: The background and peak fits to the ^{51}V(p,n)^{51}Cr TOF spectra at the four beam energies.

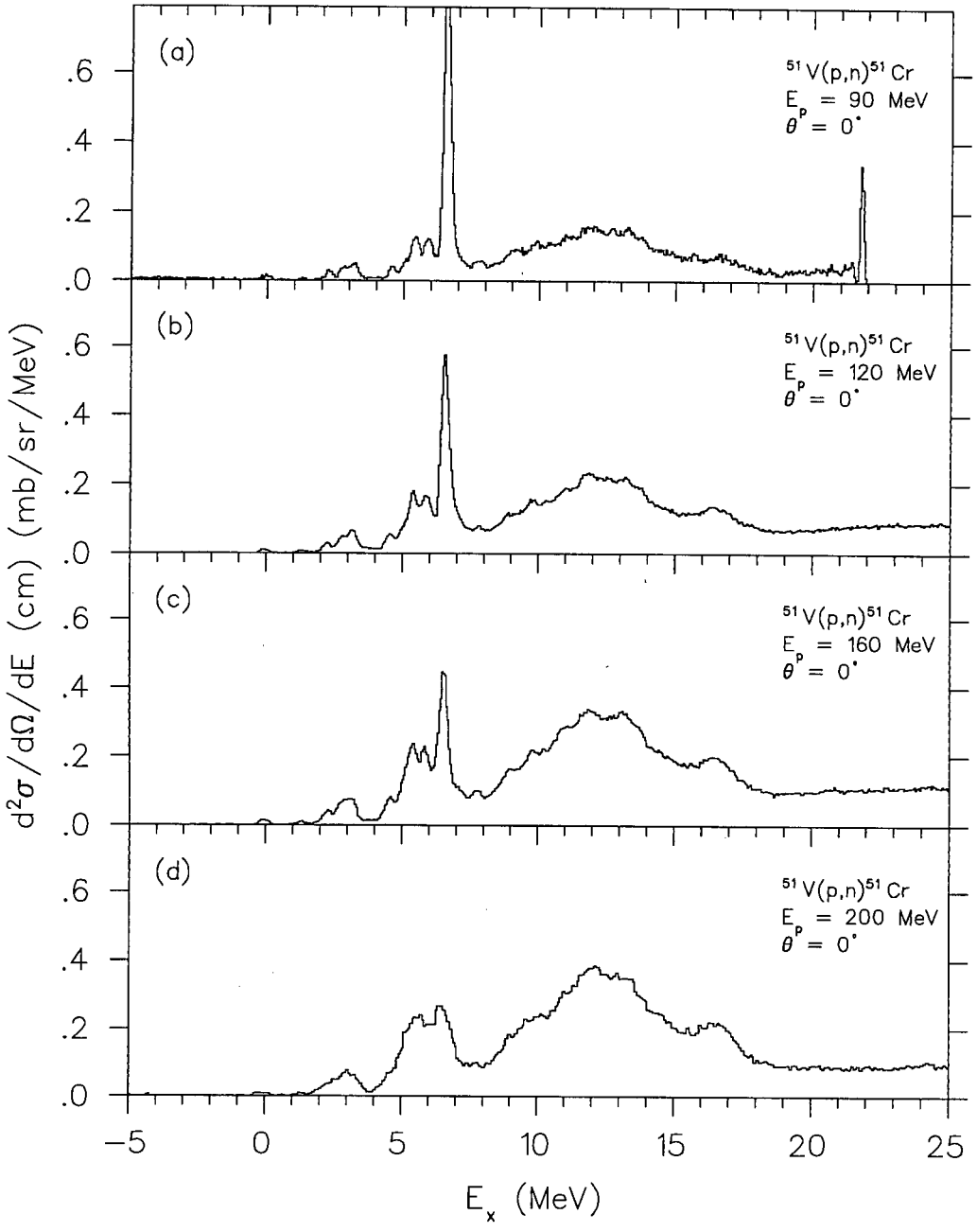

Figure 5.3: Double differential cm cross sections for ^{51}V$(p,n)^{51}$Cr as a function of excitation energy of the residual nucleus. The sharp peak at $E_x \sim 21.8$ MeV in (a) is spurious (see the text for details).

The differential cross section was then calculated for each transition as described in section 4.4 and also for each bin in the excitation energy spectra. The resulting double differential cross sections are plotted in figure 5.3.

Several features are noticeable in the spectra. They include the relatively weak transition to the ground state in ^{51}Cr at ~channel 160 in figure 5.1a, and the strong transition to the isobaric analog of the ^{51}V ground state at ~channel 358 in figure 5.1a. At low beam energy this peak is the dominant feature in the spectrum, but its cross section decreases sharply as the incident proton energy increases. The other discrete states, comprised mostly of GT transitions, are located in two groups at ~3 MeV and ~5.5 MeV and in the giant GT resonance centered at ~12 MeV. The cross sections for transitions to these states are observed to increase with increasing beam energy. This is exactly what is expected from the ratio of the spin-flip to the non-spin-flip components of the effective interaction as shown in figure 2.1b. Above the IAS peak very little confidence can be placed in the assignment of peaks to individual states. In this giant GT resonance region the assignment of peaks was made merely to use as few peaks as possible to give good fits to the data. The peaks were allowed to have large widths where the fitting program deemed necessary. As can be seen in figure 5.2 some of these peaks were made small and narrow by the fitting program to reproduce the small bumps in the spectrum while others were made large and wide to account for the broad resonance structure. No meaningful information can, therefore, be extracted from any individual one of these peaks. Rather, they represent a large number of unresolved states, and the only meaningful information is to be had from the sum of them. The sharp peak at the right hand end ($E_x \sim 21.8$ MeV) of the spectrum in figure 5.3a is an artifact of the electronic signal processing and should be ignored. It was caused by the finite width of a logic timing signal in a coincidence unit. For a range of times equal to the width of the pulse the same (long) time-of-flight was measured resulting in a peak at the far end of the spectrum.

Full results of the fits to the individual transitions, including excitation energies, cross sections, and GT strengths, are tabulated in appendix A.

5.2 Cross Sections

The cross sections for some of the more prominent transitions are plotted as a function of incident proton energy in figure 5.4. More than one dataset was acquired for each beam energy ≥ 120 MeV. These datasets consist of data taken at different times. Some of these were separated by a year or more during which time the experimental apparatus was dismantled and reconstructed. Although it was set up each time in a very similar manner, the agreement between datasets at the same energy gives confidence that there were no major systematic flaws in the experimental setup. Points at the same beam energy have been separated by 1 MeV in the plots of figure 5.4 for clarity. The top left graph in figure 5.4 shows the variation of cross section with beam energy of the IAS transition. It falls by nearly a factor of four as the beam energy increases from 90 to 200 MeV. This matches the behaviour of the non-spin-flip term of the effective interaction and indicates that most of the cross section in the IAS represents Fermi strength. If a significant portion of the cross section were GT then one would expect this drop to be much reduced. The ground state cross section at $E_p = 160$ MeV is approximately 40% larger than the previously published value of 0.08 ± 0.02 mb/sr [17]. That point, however, came from a spectrum with significantly poorer resolution than those in this work, and it is quite possible that some of the strength in the earlier spectrum was subtracted out along with the cosmic background. For the most part the points from different datasets at the same energy are in good agreement with each other. The few points of disagreement are mostly at the higher beam energies where the differences can be ascribed to the energy resolution. For example, the two points at $E_p = 160$ MeV for the peaks at $E_x = 5.11$ MeV

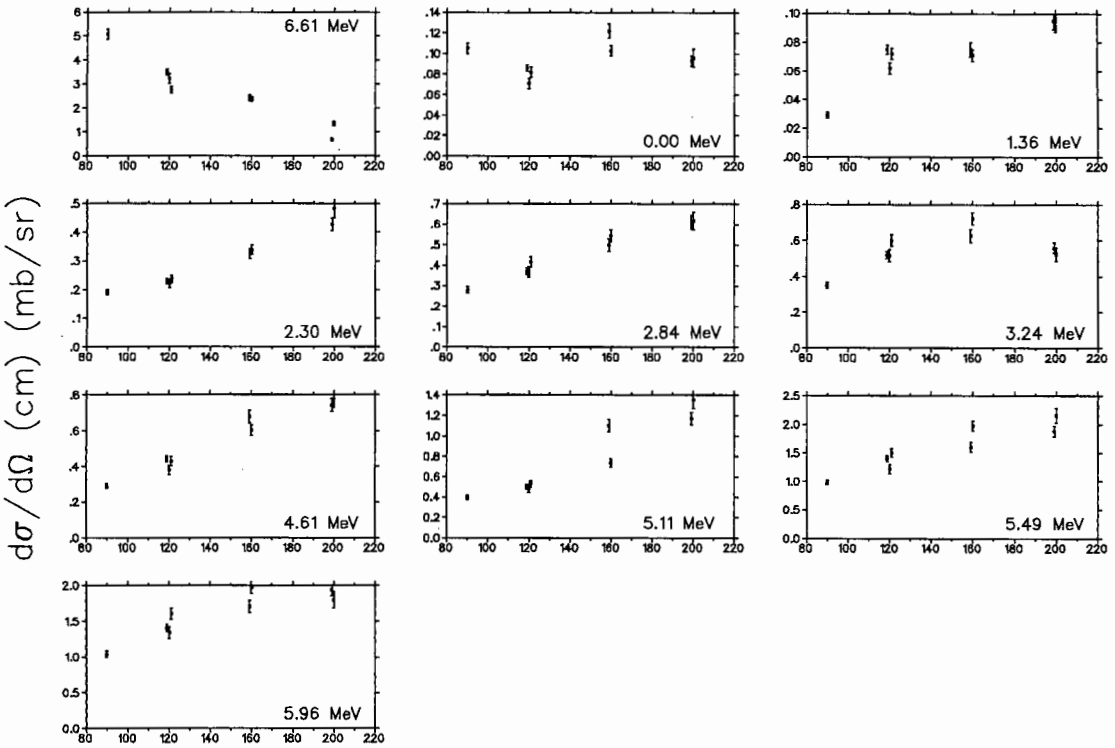

Figure 5.4: Zero degree cross sections as a function of beam energy (in MeV) for some of the transitions in ^{51}V(p,n)^{51}Cr. The top left graph shows the cross section of the IAS transition, and the other plots are for various GT transitions. The excitation energy of the residual nucleus corresponding to each transition is printed in each graph.

and $E_x = 5.49$ MeV differ by approximately 0.4 mb/sr. The two fits, therefore, merely distributed the same cross section slightly differently between the two transitions. In figure 5.5 is plotted the summed cross section of all the fitted discrete states except for the IAS. As discussed below, this is thought to be almost entirely GT cross section. As is seen in the cross sections of the individual GT transitions, the summed cross section rises smoothly by approximately a factor of three with the increasing beam energy. This rise is not quite linear but appears to level off slightly at the higher energies. The points from the different datasets are all in good agreement with each other, with the exception of one point at $E_p = 120$ MeV. This point is about 15% higher than the other two at the same energy and may be taken to indicate the maximum systematic error in the procedure to extract the cross section of the discrete part of the spectrum. This is the systematic error from the removal of the cosmic and wraparound contribution to the spectrum and the shape of the background curve which is fitted to the continuum part of the spectrum. Judging by the agreement of the other points, as well as those for the other two targets (discussed in the next chapters), this is probably an overestimate of the systematic error in the fitting procedure. The uncertainty is probably closer to 10%.

At the time this analysis was carried out, the expertise to run DWIA calculations was not locally available. Angular distributions in the limited range of $0° \leq \theta \leq 4°$ only had been acquired. These two factors meant that the identification of the various ΔL components of the spectrum by comparison of the angular distribution with DWIA calculations was not possible. It was decided to use a procedure devised by Goodman and Bloom [4] to estimate the amount of $\Delta L = 0$ strength in a zero degree spectrum from the difference between the zero degree spectrum and one at a larger angle. They scaled a 2.5° spectrum to the zero degree spectrum by a known GT part. The 0° spectrum is then subtracted from this. Because of the scaling the GT part subtracts out and

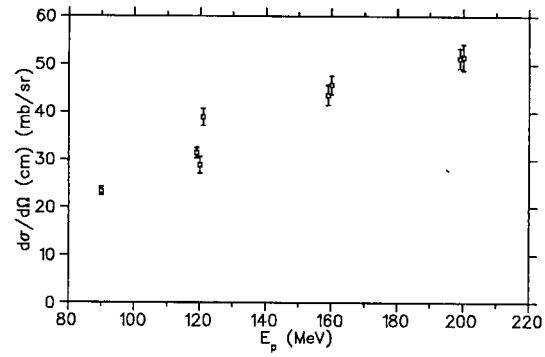

Figure 5.5: Summed zero degree cross sections of all fitted discrete states for the ^{51}V$(p,n)^{51}$Cr reaction, excluding the IAS.

what is left is assumed to be $\Delta L > 0$. This is then scaled by the cross section ratio in the region of the $\Delta L = 1$ resonance and subtracted from the 0° spectrum. What is left is assumed to be just the $\Delta L = 0$ part of the 0° spectrum. In the absence of more complete angular distributions and DWIA calculations in this analysis it was attempted to estimate the $\Delta L = 0$ distribution by comparison of the 0° and 4° spectra. Figure 5.7 shows zero degree spectra overlayed with scaled 4° spectra at beam energies of 120 and 160 MeV. The scaling has been done by the cross section in the $\Delta L = 0$ IAS. A check on the use of this part of the spectrum for the scaling was done by also scaling the spectra to the (assumed $\Delta L = 0$) group of peaks in the range $2 \leq E_x \leq 4$ MeV, which produced identical results. As the plots show, the shapes of the spectra at the two angles are almost identical in the discrete region. The 120 MeV spectra differ only above $E_x = 17$ MeV and the 160 MeV spectra only above $E_x = 12$ MeV. In both cases it appears that the continuum is the only part of the spectrum that differs. In the 160 MeV case the difference between the two angles is more pronounced and the effect is felt down to lower excitation energy. This appears to indicate that almost all the discrete structure fitted above the continuum 'background' according to the procedure of section 4.3 is $\Delta L = 0$ and, hence, assumed to be GT or Fermi strength. A multipole decomposition performed by Rapaport *et al.* [17] on the earlier 160 MeV data yielded similar results (see figure 5.6).

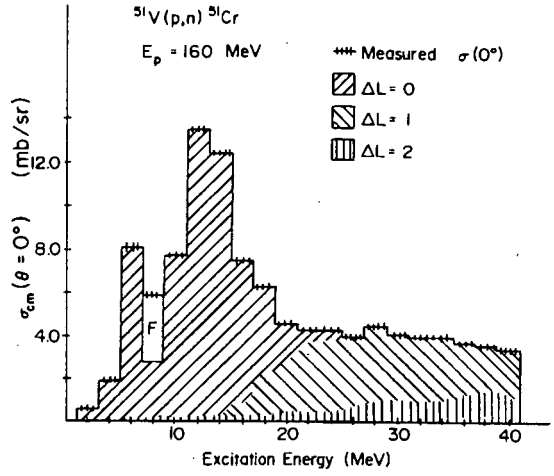

Figure 5.6: The distribution of the various multipole contributions to the ^{51}V 160 MeV spectrum. The figure is from reference [17].

There remains the question of how much of this continuum represents $\Delta L = 0$ strength. The Goodman procedure [4] would take the difference between the two spectra in each plot of figure 5.7,

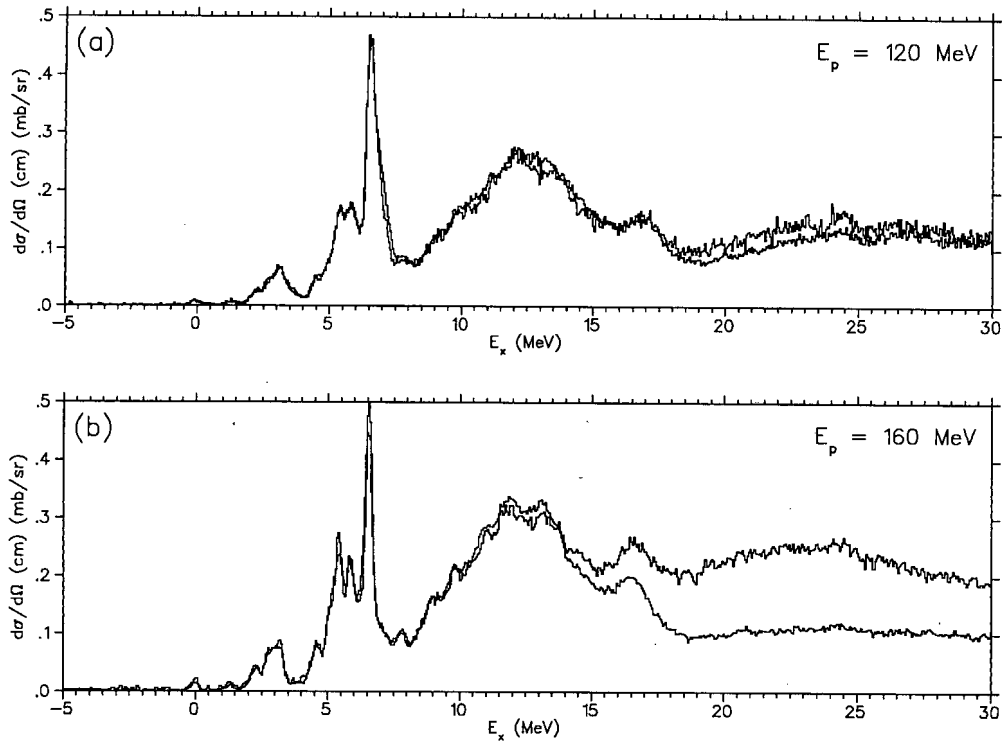

Figure 5.7: Overlays of 0° and scaled 4° ^{51}V$(p,n)^{51}$Cr spectra at (a) $E_p = 120$ MeV, and (b) $E_p = 160$ MeV. The 4° spectrum is scaled to the 0° spectrum in the region of the IAS at $E_x = 6.61$ MeV. In both cases the upper curve at $E_x \geq 20$ MeV is the 4° spectrum.

scale that by the cross section ratio in the region of the $\Delta L = 1$ resonance, and subtract this from the zero degree spectrum. Since the two spectra differ only in this region that would effectively remove all the continuum from identification as $\Delta L = 0$ strength. Clearly this represents the lower limit on the GT strength in this region. The upper limit is obtained by regarding all the strength as $\Delta L = 0$.

5.3 Gamow-Teller Strength

^{51}Cr has a GT beta decay to the ground state of ^{51}V which has been measured. This allows the calculation of the GT strength of this transition and can be used to normalise the GT strength of all the other GT transitions. The measured $\log ft$ for the gs $\rightarrow$ gs $^{51}\mathrm{Cr} \xrightarrow{EC} {}^{51}\mathrm{V}$ is $\log ft = 5.3906 \pm 0.0016$ [18]. From eq. 2.5 one then gets the GT beta decay strength of the ground state transition

$$B(\mathrm{GT}) = 0.01565 \pm 0.00008$$

and since the ground states of ^{51}Cr and ^{51}V both have $J^\pi = \frac{7}{2}^-$, the (p,n) GT strength (from eq. 2.9) has the same value. Since the unit cross section is the same for any transition in a particular spectrum, one obtains the GT strength in any other transition from the ratio of its cross section to that of the ground state according to eq. 2.17. The danger of this procedure for this particular case, is that the transition of known strength is a very weak transition resulting in large uncertainties in the extracted strengths. Figure 5.8 contains plots of the extracted strengths for the same few transitions whose cross sections are plotted in figure 5.4. These strengths are obtained under the assumption that they are pure GT transitions. The IAS is a special case. ^{51}V is an odd-A nucleus and, therefore, the ground state spin is half integral. The transition to the IAS in

^{51}Cr is $\frac{7}{2} \longrightarrow \frac{7}{2}$ and can proceed via both the F and GT operators. From the sharp decrease in cross section with increasing beam energy, which is characteristic of Fermi strength, one expects that only a small fraction of the IAS transition strength will be GT. This fraction, f_{GT}, can be calculated using the empirically derived ratio of GT to Fermi unit cross sections, as discussed in section 2.5, and the ratio of ground state to IAS cross sections, as shown in eq. 2.24. The results of this calculation for the various beam energies are plotted in figure 5.9 and listed in table 5.1. In all cases the value of f_{GT} comes out negative, which is clearly unphysical. Most of these points are clustered around $f_{GT} = -0.7$. The error bars shown in figure 5.9 are the statistical uncertainties and are too small for the values of f_{GT} to be consistent with zero. Because of this the GT strengths in the IAS transitions have been set to their minimum possible value of zero, which is what is plotted in the top left graph of figure 5.8. The uncertainty in $B(GT)$ for the IAS should have very little effect on the total GT strength in the spectra. The sums of the GT strengths in all the fitted discrete states are plotted in figure 5.12a and listed in table 5.1.

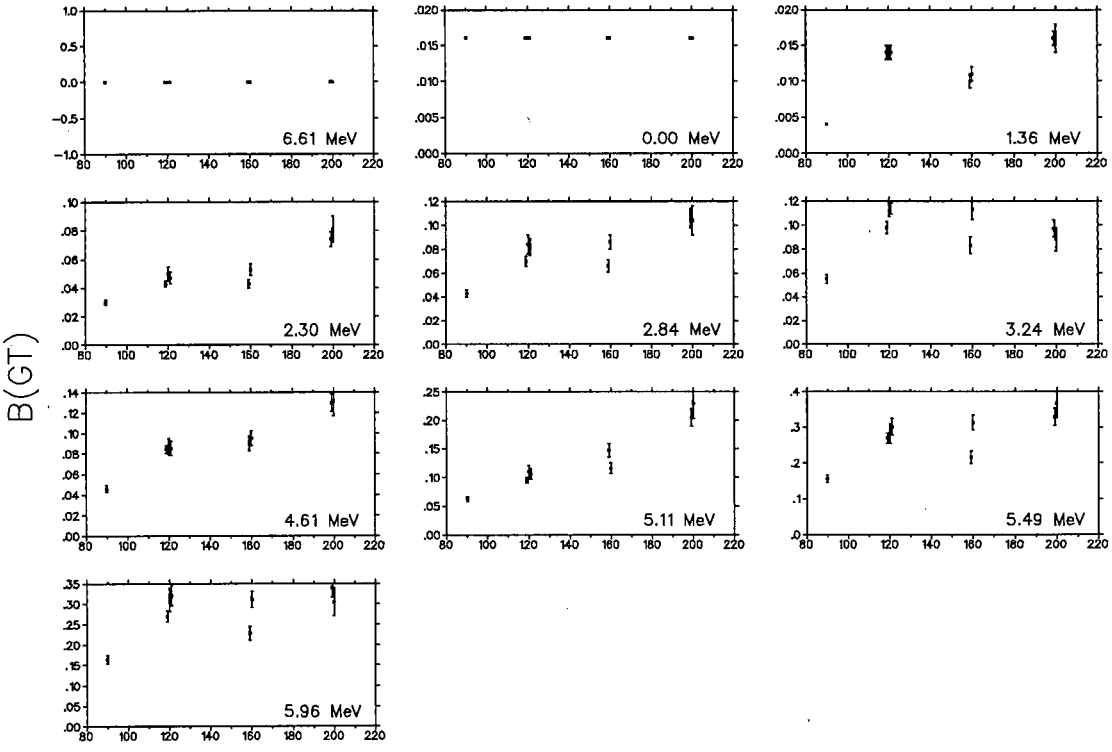

Figure 5.8: GT strengths at the measured beam energies (in MeV) for some of the transitions in ^{51}V(p,n)^{51}Cr. The top left graph represents the IAS transition. The excitation energy of the residual nucleus corresponding to each transition is printed in each graph.

Since the statistical uncertainties cannot account for the calculated values of f_{GT}, it is necessary to examine possible systematic uncertainties. Examination of eq. 2.24 reveals two possible causes for the effect. Either the empirically determined $R(E_p, A)^2$ is too small, or the ratio of ground state to IAS cross sections is too large. As was discussed in section 2.5, some doubt has been cast on the validity of the slope parameter $E_o = 55.0 \pm 0.4$ MeV for odd mass nuclei [20, 21], although more recent evidence [45] supports the original value of E_o. If, however, the alternate value of $E_o = 45.0 \pm 0.6$ MeV as proposed by Huang [21] is used, most of the points are brought considerably closer to zero, but not enough for the statistical error to make them consistent with zero. The more probable explanation lies in the ratio of ground state to IAS cross sections. As discussed above, the IAS cross section is probably accurately determined, especially at the lower beam energies. However the ground state is a very weak transition. There is some suspicion [45]

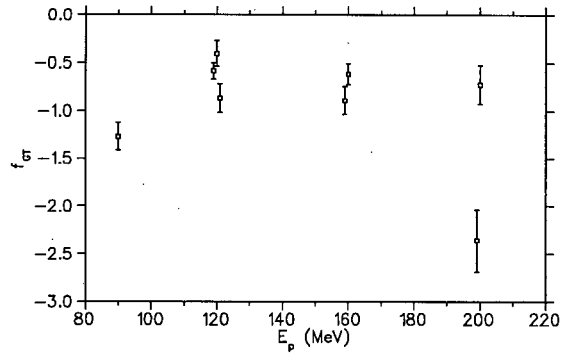

Figure 5.9: Calculated fraction of GT strength in the IAS transition of ^{51}V(p,n)^{51}Cr. See the text for discussion on why it is less than zero.

that it may suffer from contamination of $\Delta L \neq 0$ components. As discussed above, the evidence from figure 5.7 suggests that there is very little contribution from $\Delta L > 0$ strength in the discrete part of the spectrum. However, even a small quantity could amount to a significant fraction of the ground state cross section, thus making the second term of eq. 2.24 too large. Figure 5.4 shows that the ground state cross section does not exhibit the same energy dependence as the other, stronger transitions. Assuming that both $R(E_p, A)^2$ is well known and the IAS cross section is accurately extracted, it is possible to calculate how much of the ground state cross section must be attributed to non $\Delta L = 0$ strength in order for f_{GT} to be zero. For most of the points in figure 5.9 this requires approximately 40% of the ground state cross section to be due to non-GT strength. The two exceptions are the 90 MeV point and the one 200 MeV point. The 90 MeV point is low because of the relatively large ground state cross section. Inspection of figure 5.4 shows that for all the strong transitions (which are presumed to be almost pure GT transitions) the cross section at 90 MeV is lower than at all other measured beam energies. In the case of the ground state the 90 MeV cross section is one of the largest measured. The IAS cross section follows the expected trend, and this results in a very low f_{GT}. The one 200 MeV point disagrees with the other points due to poor energy resolution. This spectrum is plotted in figure 5.10 for comparison with the other dataset plotted in figure 5.3d. The poor resolution in this case resulted in some of the IAS cross section being lost in the GT background. The low value for f_{GT} in this case was due to an underestimate of the IAS cross section and an overestimate of the ground state GT cross section.

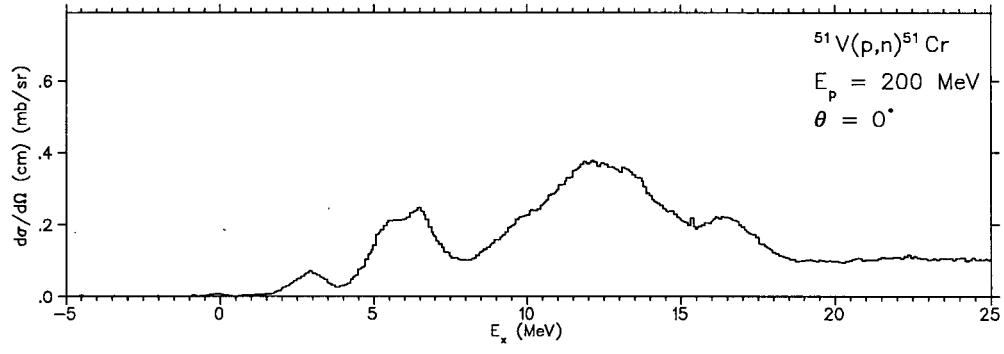

Figure 5.10: Double differential cm cross section for 0° ^{51}V(p,n)^{51}Cr at 200 MeV. The poor resolution of this dataset in comparison with the one shown in figure 5.3d results in an underestimate of the IAS cross section.

Further discussion of the question of GT strength in the continuum below and beyond the discrete part of the spectrum is in order. The procedure used to extract the yields of the discrete transitions in the spectra employed a polynomial fit to the region above $E_x \approx 20$ MeV which was forced to

drop smoothly to zero below the peaks at low excitation energy. Effectively this modeled the broad continuum structure and subtracted it from the discrete part of the spectrum, and is a procedure in common use in experimental (p,n) analysis. Osterfeld [52, 53] has criticised this procedure in the light of calculations of his on ^{48}Ca$(p,n)^{48}$Sc (figure 2.3) which show that almost all the cross section below the discrete states is due to GT strength. His calculations indicate that the background of $\Delta L > 0$ strength accounts for most of the spectrum above the GT resonance, but drops off sharply to zero beneath the GT resonance. The results of the multipole decomposition of Rapaport *et al.*[17] (compare figure 5.6 with figure 2.3) indicates a similar effect for ^{51}V with the higher multipole contributions dropping off to almost zero in the region of $12 \leq E_x \leq 22$ MeV. Application of the Goodman procedure [4] for estimating the $\Delta L = 0$ components of the zero degree spectra, which was described in the previous section, resulted in the spectra shown in figure 5.11 for beam energies of 120 and 160 MeV. This also suggests that the $\Delta L = 0$ strength is concentrated below 20 MeV in excitation. In order to estimate the GT strength below the background fit and thus excluded from the discrete peaks already examined, the following simple procedure was adopted. An excitation energy was selected in the region where there is a large mixture of $\Delta L = 0$ strength and higher multipoles, and all the strength in the background below this energy was assumed to be $\Delta L = 0$ strength. This excluded any $\Delta L = 0$ strength above this energy, but included the $\Delta L > 0$ strength below it. The selection of this point was made so that the excluded $\Delta L = 0$ strength was approximately equal to the included $\Delta L > 0$ strength. For ^{51}V$(p,n)^{51}$Cr the excitation energy selected for this procedure was $E_x = 18$ MeV. Combined with the strength seen in the discrete states, this provided an estimate of the total GT strength in the spectra up to $E_x = 20$ MeV, and is presented in figure 5.12b and table 5.1.

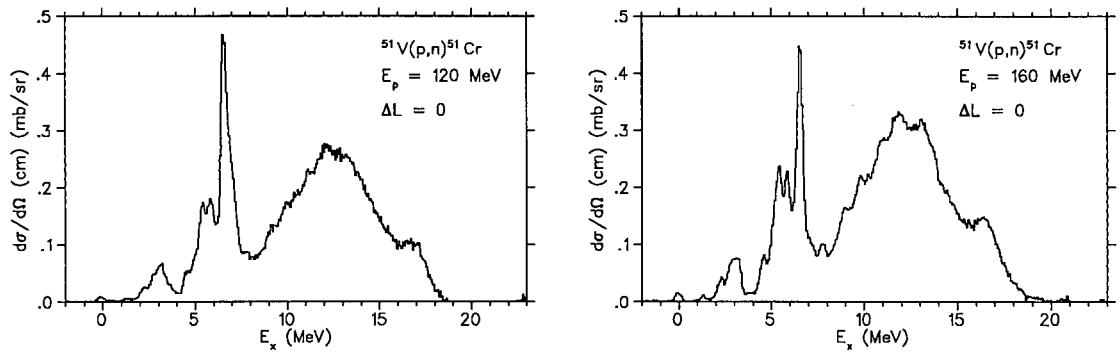

Figure 5.11: Estimated $\Delta L = 0$ component of the zero degree ^{51}V$(p,n)^{51}$Cr spectra at $E_p = 120$ and 160 MeV.

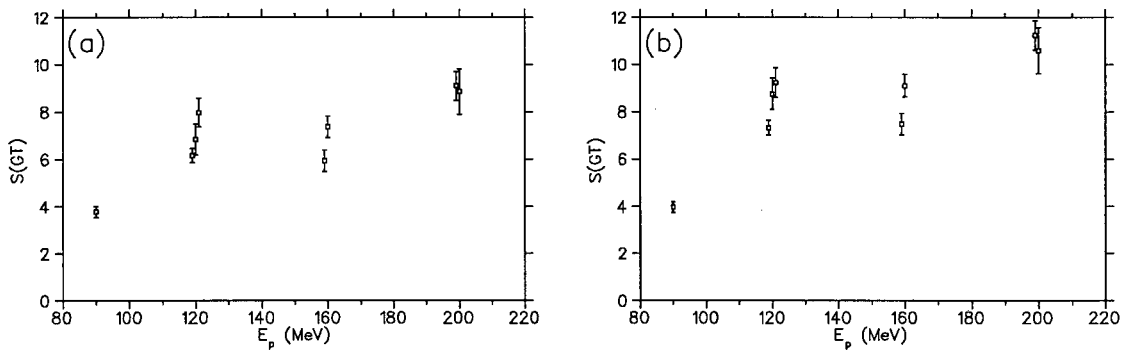

Figure 5.12: Summed GT strength in (a) the discrete structure of ^{51}V$(p,n)^{51}$Cr, and (b) the discrete structure plus the background contribution up to $E_x = 20$ MeV.

In order to compare this with the predictions of the GT sum rule given by eq. 2.30 the β^+ strength

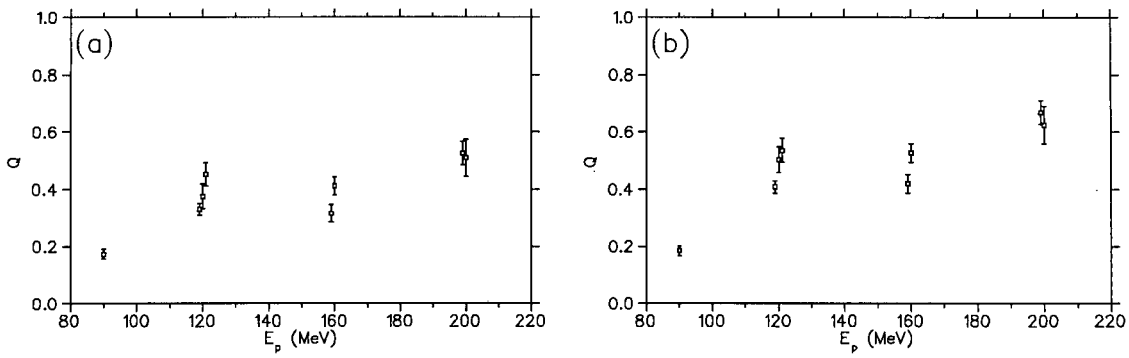

Figure 5.13: The Gamow-Teller sum rule quenching factors $Q = (S(\mathrm{GT})^- - S(\mathrm{GT})^+)/3(N-Z)$ for ^{51}V$(p,n)^{51}$Cr if (a) only the strength in the discrete region is considered, and (b) if the strength in the background below the GT resonance is included.

must also be measured. Since ^{51}V has a neutron excess of 5 this is expected to be much smaller than the β^- strength due to Pauli blocking. The recent (n,p) experiment of Alford *et al.* [65] at 198 MeV has confirmed this with a value of $S(\mathrm{GT})^+ = 1.2 \pm 0.1$ up to 8 MeV in excitation energy. The GT sum rule predicts that the difference between the two sums should be equal to $3(N-Z) = 15$. The quenching factor Q, defined to be the ratio of the difference between observed GT strengths to the sum rule prediction of $3(N-Z)$ is presented in figure 5.13 and table 5.1. This is done for case where $S(\mathrm{GT})^-$ is taken to be just the strength in the discrete states and for the case where $S(\mathrm{GT})^-$ includes the background below the GT resonance up to $E_x = 20$ MeV. Without the background contribution the GT strength falls far short of the expected amount. A maximum of only about 50% of the sum rule prediction is observed. When including the estimated background contribution this figure rises to a maximum of 67% which is similar to the previous measurement on ^{51}V by Rapaport *et al.* [17] at 160 MeV. They measured $S(\mathrm{GT})^- = 12.6 \pm 2.5$ which is just over 10% larger than the largest value from this work (at 200 MeV), and about 50% larger than the 160 MeV points. However, they report a quenching factor of 0.63, where this is defined to be the ratio of the measured $S(\mathrm{GT})^-$ to a calculated $S(\mathrm{GT})^-$, which agrees with the maximum value of

E_p (MeV)	f_{GT}	$S(\mathrm{GT})^-$ Discrete states	$Q^\dagger$	$S(\mathrm{GT})^-$ (0 – 20 MeV) Discrete + background	$Q^\ddagger$
90	-1.27 ± 0.14	3.79 ± 0.23	0.17 ± 0.02	3.98 ± 0.23	0.19 ± 0.02
120	-0.58 ± 0.08	6.15 ± 0.30	0.33 ± 0.02	7.33 ± 0.31	0.41 ± 0.02
120	-0.40 ± 0.13	6.83 ± 0.64	0.38 ± 0.04	8.76 ± 0.66	0.50 ± 0.04
120	-0.87 ± 0.15	7.97 ± 0.61	0.45 ± 0.04	9.24 ± 0.61	0.54 ± 0.04
160	-0.89 ± 0.15	5.93 ± 0.44	0.32 ± 0.03	7.49 ± 0.46	0.42 ± 0.03
160	-0.62 ± 0.11	7.36 ± 0.47	0.41 ± 0.03	9.12 ± 0.48	0.53 ± 0.03
200	-2.36 ± 0.32	9.10 ± 0.62	0.53 ± 0.04	11.24 ± 0.63	0.67 ± 0.04
200	-0.72 ± 0.20	8.85 ± 0.95	0.51 ± 0.06	10.59 ± 0.97	0.63 ± 0.07

Table 5.1: The calculated fraction of GT strength in the IAS, the total GT strength in the discrete region, the quenching factor $Q^\dagger$ assuming the total GT strength is that in column 3, the total GT strength in the discrete region plus the background under the GT resonance, and the quenching factor $Q^\ddagger$ assuming that the total GT strength is that in column 5, for ^{51}V$(p,n)^{51}$Cr at the four measured beam energies.

Q reported here. It must be remembered, though, that the sum rule prediction is being compared to the difference between two measured (and probably incomplete) values. The total measured β^- strength, however, including the background contribution, is no more than about two thirds of minimum value of $3(N-Z) = 15$ obtained by putting $S(\mathrm{GT})^+ = 0$. If the calculated strengths presented here are accurate, then a significant fraction of the strength must lie in the continuum region beyond $E_x = 20\,\mathrm{MeV}$. However, as discussed above, there is a large systematic uncertainty in these strengths from the extraction of the cross sections due to GT strength in the ground state transition. This is discussed further in the next section.

5.4 Alternate Gamow-Teller Strength Calculation

The GT strengths derived above are all normalised to the GT strength in the transition to the ^{51}Cr ground state, which is known from beta decay. The problems related to the weakness of this transition and the possible contamination of it by non-GT strength makes this procedure far from ideal. The possible inclusion of a small amount of non-GT strength results in a large statistical uncertainty in the extracted strengths. However, as discussed above, the evidence suggests that the amount of GT strength mixed in with the Fermi strength in the IAS transition is small. If that amount is assumed to be known, it is then possible to normalise the GT strength in the spectra to the Fermi strength in the IAS. Because the IAS transition is a much stronger transition this procedure would effectively eliminate the systematic uncertainties associated with the possible inclusion of non-GT strength in the ground state cross section. This has been done assuming a value of $f_{\mathrm{GT}} = 0.00 \pm 0.15$, ie. that the IAS transition is a pure Fermi transition. The GT strengths may then be calculated according to eq. 2.26. The results are listed in table 5.2 and plotted in figures 5.14 to 5.16. Since this procedure depends crucially on the accurate determination of the IAS cross section, the one 200 MeV point with poor resolution has been omitted.

E_p (MeV)	f_{GT}	$S(\mathrm{GT})^-$ Discrete states	$Q^\dagger$	$S(\mathrm{GT})^-$ (0 – 20 MeV) Discrete + background	$Q^\ddagger$
90	0.00 ± 0.15	7.35 ± 0.42	0.41 ± 0.03	7.78 ± 0.42	0.44 ± 0.03
120	0.00 ± 0.15	8.57 ± 0.46	0.49 ± 0.03	10.41 ± 0.47	0.61 ± 0.03
120	0.00 ± 0.15	8.47 ± 0.76	0.48 ± 0.05	11.14 ± 0.80	0.66 ± 0.05
120	0.00 ± 0.15	13.09 ± 0.93	0.79 ± 0.06	15.41 ± 0.94	0.95 ± 0.06
160	0.00 ± 0.15	10.12 ± 0.77	0.59 ± 0.05	12.94 ± 0.80	0.78 ± 0.05
160	0.00 ± 0.15	10.75 ± 0.72	0.64 ± 0.05	13.46 ± 0.75	0.82 ± 0.05
200	0.00 ± 0.15	13.99 ± 1.71	0.85 ± 0.11	16.81 ± 1.75	1.04 ± 0.12

Table 5.2: The calculated fraction of GT strength in the IAS, the total GT strength in the discrete region, the quenching factor $Q^\dagger$ assuming the total GT strength is that in column 3, the total GT strength in the discrete region plus the background under the GT resonance, and the quenching factor $Q^\ddagger$ assuming that the total GT strength is that in column 5, for ^{51}V$(p,n)^{51}$Cr at the four measured beam energies if the IAS is assumed to be a pure Fermi transition.

The most obvious effect of this is the significant increase in the derived GT strengths. The energy dependence of the derived GT strengths has also been lessened, although there is still a general increase in strength with beam energy. It is now seen that the minimum value of $3(N-Z) = 15$ for $S(\mathrm{GT})^-$ is met by the total strength obtained for the 200 MeV point, and in fact the difference between measured $S(\mathrm{GT})^-$ and $S(\mathrm{GT})^+$ satisfies the sum rule prediction. Increasing the assumed

value of f_{GT} results in larger derived GT strengths (compare figures 5.15 and 5.17). Clearly the assumed value of $f_{GT} = 0$ represents the lower limit on the derived strengths. It is now important to determine the value of f_{GT} accurately. This requires a polarised beam experiment with its ability to distinguish spin-flip from non-spin-flip components.

Returning briefly to the question of possible non-GT strength in the ground state cross section, it is seen that reducing the ground state cross section in eq. 2.17 would lead to increased GT strengths. This was the relation used to determine the GT strengths relative to the ground state strength. Since the choice of $f_{GT} = 0$ leads to the lower limit of measured GT strength, it seems clear that the previous values are too low. In other words, the GT strengths derived under the assumption of $f_{GT} = 0$ support the theory of non-GT contamination of the ground state transition.

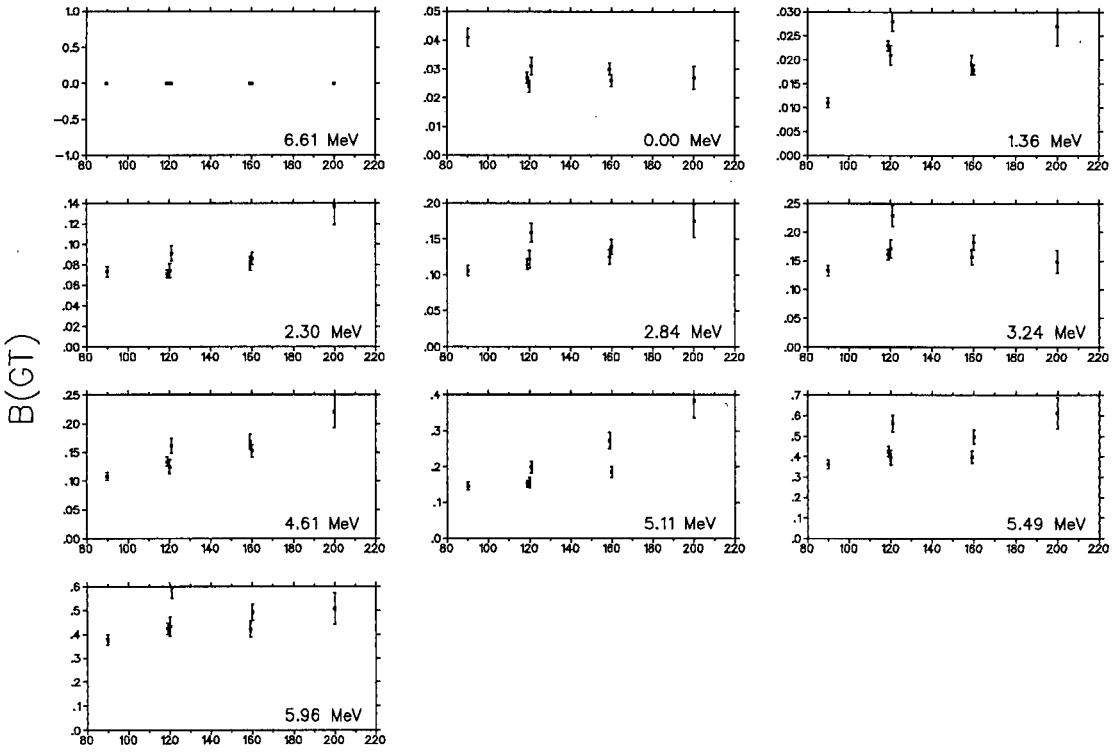

Figure 5.14: GT strengths at the measured beam energies (in MeV) for a few of the peaks fitted to the ^{51}V(p,n)^{51}Cr spectra, assuming that the IAS is a pure Fermi transition.

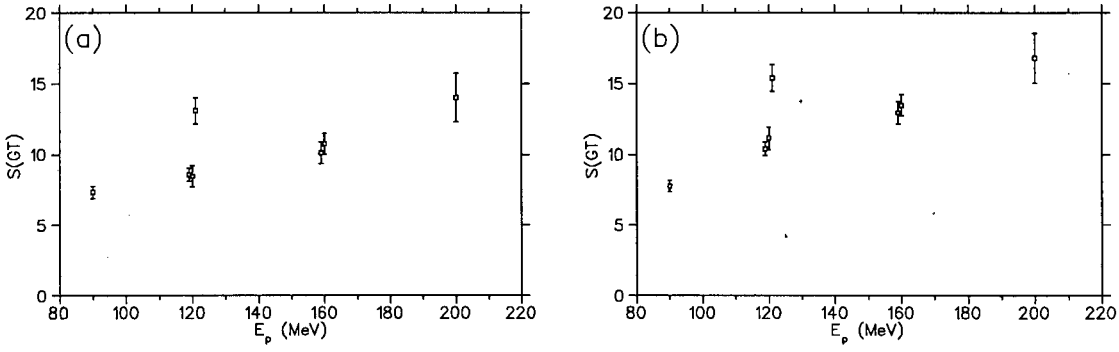

Figure 5.15: Summed GT strength in (a) the discrete structure of ^{51}V(p,n)^{51}Cr, and (b) the discrete structure plus the background contribution up to $E_x = 20$ MeV, assuming that the IAS is a pure Fermi transition.

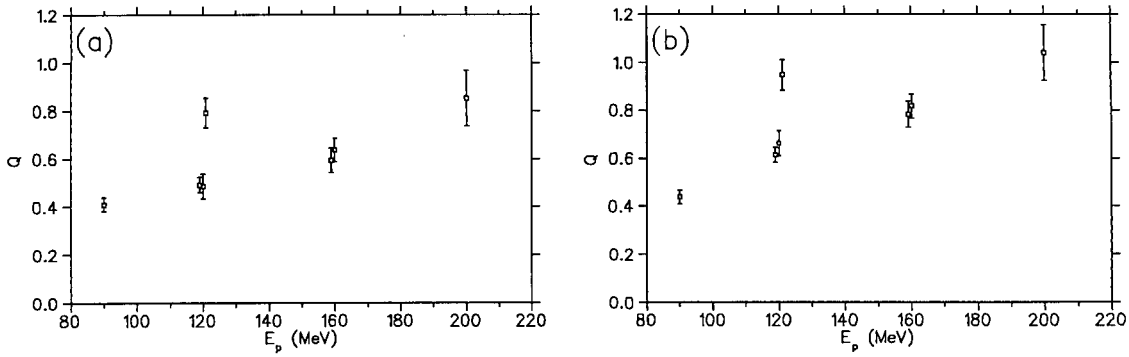

Figure 5.16: The Gamow-Teller sum rule quenching factors $Q = (S(\mathrm{GT})^- - S(\mathrm{GT})^+)/3(N-Z)$ for ^{51}V$(p,n)^{51}$Cr if (a) only the strength in the discrete region is considered, and (b) if the strength in the background below the GT resonance is included, assuming that the IAS is a pure Fermi transition.

Lastly, a check was performed to test whether the choice of zero f_{GT} was not some special value leading to meaningless $B(\mathrm{GT})$ results. An arbitrary choice of $f_{\mathrm{GT}} = 0.50 \pm 0.15$ was made, ie. fully half the IAS transition strength is GT strength, and the same calculations performed. The total GT strengths thus derived are plotted in figure 5.17. As expected the values are much greater than for $f_{\mathrm{GT}} = 0$, but the systematics appear to be quite insensitive to the exact value chosen.

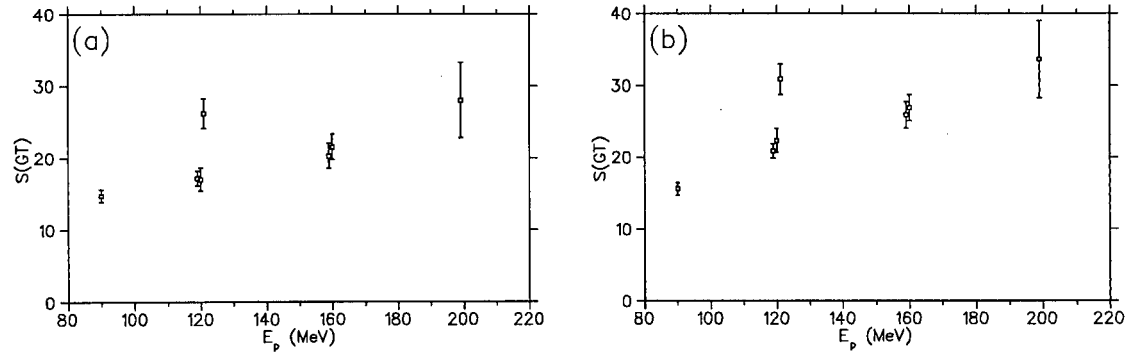

Figure 5.17: Summed GT strength in (a) the discrete structure of ^{51}V$(p,n)^{51}$Cr, and (b) the discrete structure plus the background contribution up to $E_x = 20$ MeV, assuming $f_{\mathrm{GT}} = 0.5$.

Chapter 6

^{54}Fe(p,n)^{54}Co Analysis

6.1 Fits to the Spectra

Zero degree time-of-flight spectra for ^{54}Fe(p,n)^{54}Co at the four measured beam energies are presented in figure 6.1. These spectra are the complete TOF spectra for a particular dataset. They comprise the sum of all runs in that dataset after those runs had been normalised to a common time scale and each section shifted into alignment with each other as described in section 4.1.

After accumulation into the TOF spectra, the slow neutron wraparound background was removed as described in section 4.2 and a fit was made to the discrete states as described in section 4.3. The IAS of the ^{54}Fe 0^+ ground state is the ground state of ^{54}Co. This state is cleanly separated from all the other states and does not sit on top of any GT background. It was therefore fitted along with all the other peaks, as opposed to the special procedure necessary in the case of ^{51}V and ^{59}Co. Selection of which peaks to fit was made on the principle of using as few peaks as possible to adequately reproduce the discrete part of the spectra. The same set of peaks was used to fit the spectra up to $E_x = 14$ MeV at all angles and beam energies for a particular target. In order to obtain good fits to the ^{54}Fe spectra it was necessary to fit 29 peaks to the data. The ground state and first excited state peaks are clearly separated from each other for beam energies ≤ 160 MeV. It is evident that these peak shapes are not completely symmetrical, and the procedure described in section 4.3 employing a second, small gaussian to model the asymmetric shoulder, was used for the fits to these energies. The peak widths were constrained to be the same for all peaks above the lowest two states in a particular spectrum, and were generally set by the fitting program to be a little broader than the first two. The exception to this is the 90 MeV spectrum. It was found to be impossible to get good fits to the data if the peak widths were constrained to be the same, and it was necessary to allow them to be fixed independently by the fitting program. This suggests that several of them may, in fact, be due to groups of unresolved states. The results of the wraparound removal and the fits to the 0° data are shown in figure 6.2. The ground state peak and the prominent peak at 10.06 MeV [25, 66] were then used to determine the time-to-energy calibration and to convert the TOF spectra to excitation energy spectra as described in section 4.3. The uncertainty in the energy calibration is estimated to be less than 100 keV. The differential cross section was calculated for each transition as described in section 4.4 and also for each bin in the excitation energy spectra. The resulting double differential cross sections are plotted in figure 6.3.

^{54}Fe is an even-even nucleus so the ground state has $J^\pi = 0^+$. The IAS in ^{54}Co must have the same spin and parity, so the transition to the IAS is a pure Fermi transition according to eq. 2.6. The strong transitions to the ^{54}Co 0^+ ground state, which is the isobaric analog of the ^{54}Fe ground state, and the first excited 1^+ state at 0.94 MeV, are seen to be clearly separated from the rest of the spectrum. The other strong transitions are the one at 10.06 MeV and its neighbours, as was

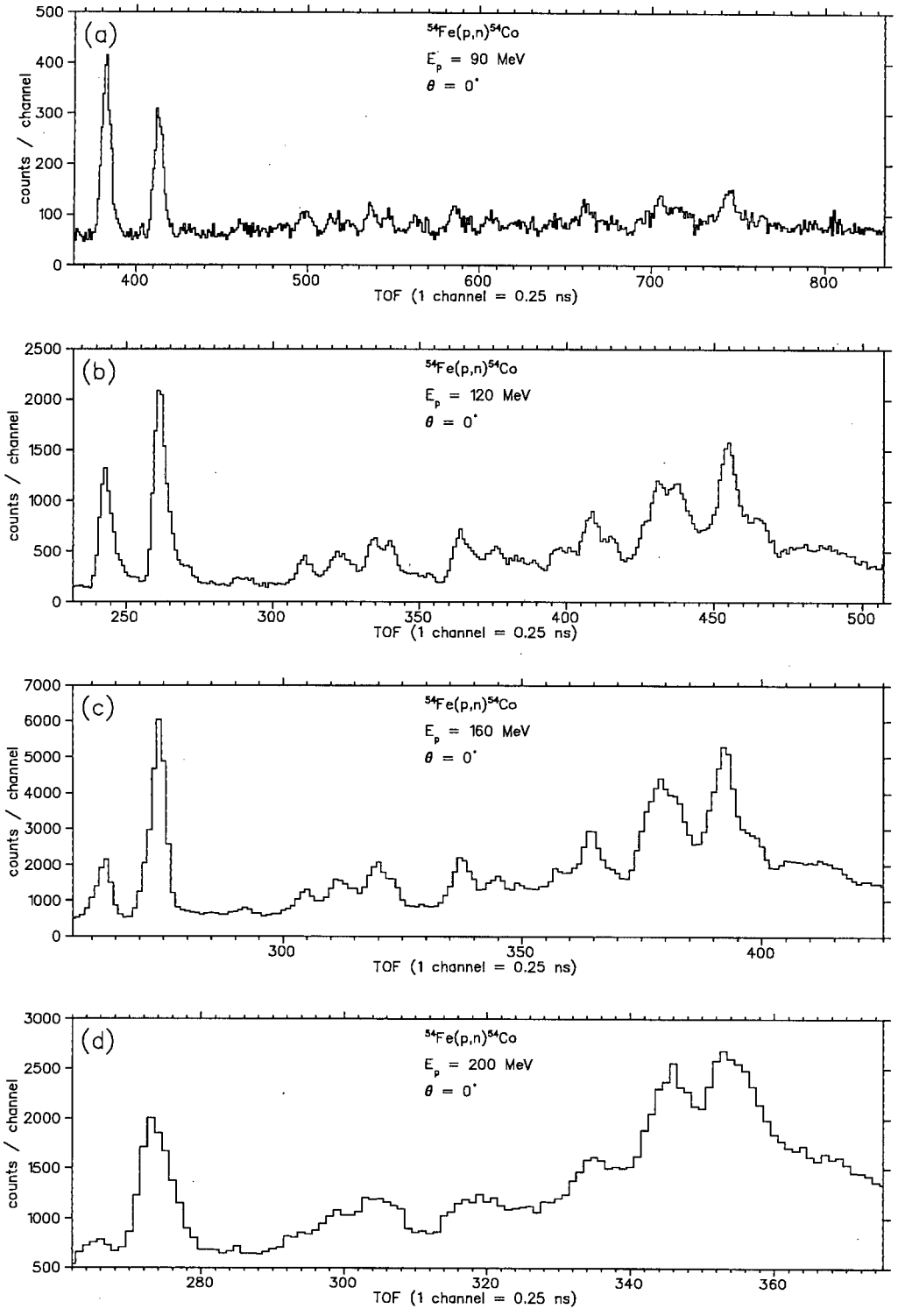

Figure 6.1: The ^{54}Fe(p,n)^{54}Co TOF spectra at beam energies from 90 to 200 MeV.

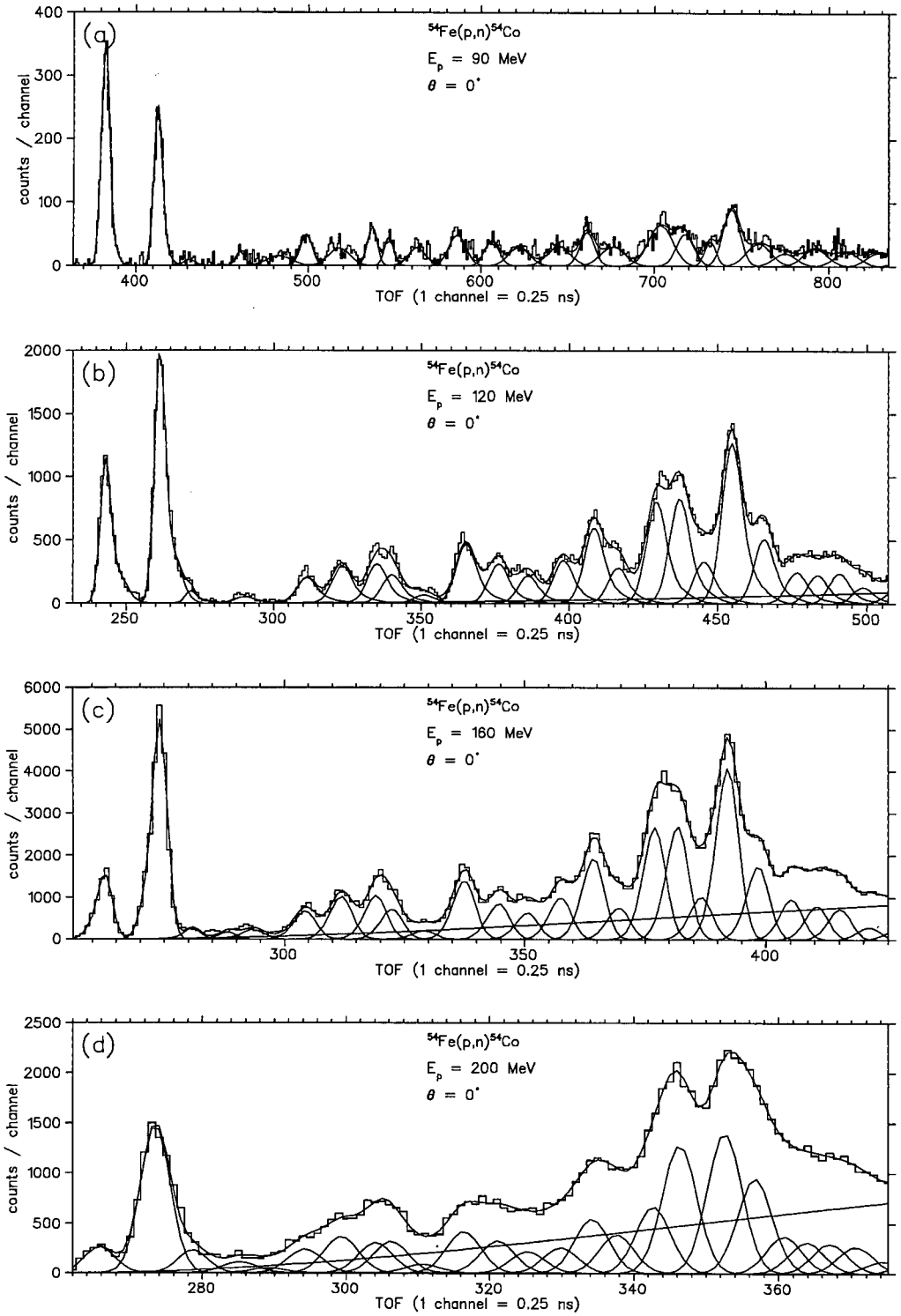

Figure 6.2: The background and peak fits to the ^{54}Fe(p,n)^{54}Co TOF spectra at the four beam energies.

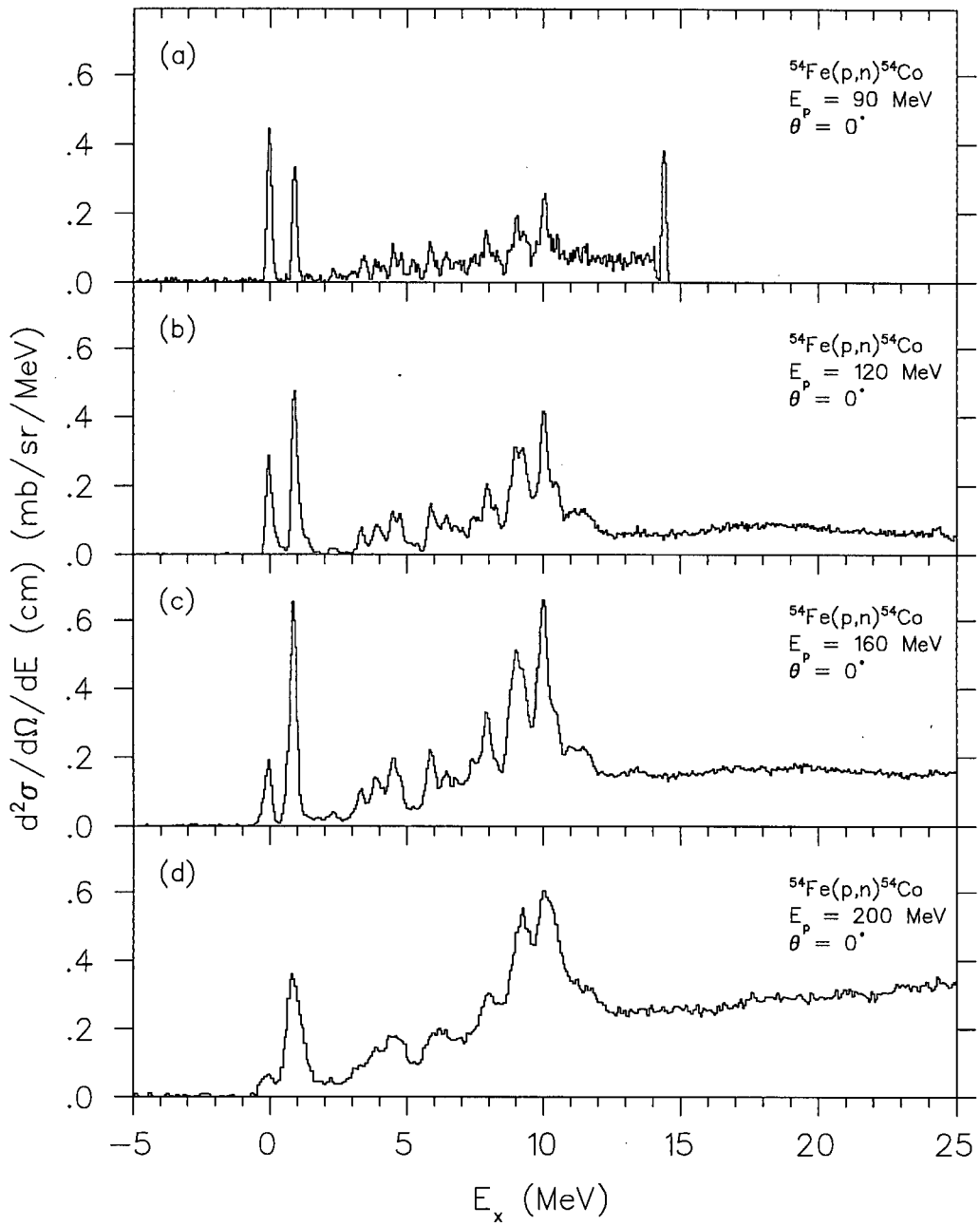

Figure 6.3: Double differential cm cross sections for ^{54}Fe(p,n)^{54}Co as a function of excitation energy of the residual nucleus. The sharp peak at $E_x \sim 14.4$ MeV in (a) is spurious (see the text for details).

observed previously [22, 23, 25]. The state at 5.31 MeV is observed to be weakly excited in disagreement with the low energy results of ref. [22], but in agreement with the 120 and 160 MeV results of ref. [23] and the 135 MeV data of ref. [25]. Similar strength distribution was observed at 300 MeV [24], although with much lower energy resolution. The IAS cross section decreases dramatically with increasing beam energy, while the GT components increase strongly. The giant GT resonance (GTGR) is seen to be highly fragmented with significant groupings at approximately 4 MeV, 6.5 MeV, 8 MeV, and 10 MeV in addition to the strong GT transition at 0.94 MeV. As was the case in the ^{51}V spectra, the sharp peak at the right hand end of the spectra ($E_x \sim 14.4$ MeV in figure 6.3a) is an artifact of the electronic signal processing and should be ignored. It was caused by the finite width of a logic timing signal in a coincidence unit. For a range of times equal to the width of the pulse the same (long) time-of-flight was measured resulting in a peak at the far end of the spectrum.

Full results of the fits to the individual transitions, including excitation energies, cross sections, and GT strengths, are tabulated in appendix A.

6.2 Cross Sections

The cross sections for some of the more prominent transitions are plotted as a function of incident proton energy in figure 6.4. Two datasets were acquired at each of the 160 and 200 MeV beam energies. They consist of data taken during separate experimental runs as described in the previous chapter. The points corresponding to these datasets have been separated by 1 MeV in the graphs for clarity. The top left graph in figure 6.4 shows the energetics of the ground state IAS transition. This is a $0^+ \rightarrow 0^+$ transition and is thus a pure Fermi transition. Its cross section drops sharply as is expected of a Fermi transition. Between 90 and 200 MeV it drops by a factor of approximately two. The other transitions all exhibit increasing cross section with increasing beam energy. This increase appears to depend on the strength of the particular transition. The cross sections of the weaker transitions increase by a factor of roughly 3 from 90 to 200 MeV while for the strongest transitions this factor exceeds 5. This may possibly be due to some of the weaker transitions not being pure GT transitions, or just that a similar amount of non $\Delta L = 0$ contamination has a greater effect on a weak transition than on a strong one. As discussed below, there is evidence that some of the weaker transitions are of mixed strength. The effects of decreasing energy resolution with higher beam energy is again evident in the variations in the distribution of strength between closely spaced states; as demonstrated, for example, at $E_p = 200$ MeV in the states between $E_x = 8$ and 9 MeV.

Previously published analyses of ^{54}Fe(p,n)^{54}Co indicate that most of the cross section up to about $E_x = 15$ MeV is due to GT strength [23, 24, 25]. Without a full DWIA calculation and multipole decomposition it is not possible to identify which of the extracted transitions are pure GT or mixed with higher multipoles. The analysis of Anderson *et al.* [25] at 135 MeV, however, did include this. They identified 14 peaks as pure $\Delta L = 0$ transitions containing 86% of the total $\Delta L = 0$ strength. The other peaks were identified as mixed transitions with $\Delta L = 0$ components obtained by subtracting calculated $\Delta L > 0$ shapes from the angular distributions. The deconvolution of states from the spectra in this work yields very similar results to that of the 135 MeV analysis of reference [25], which presented the only other data of comparable resolution to that of this work. The transitions extracted in this work which corresponded to those identified by Anderson *et al.* as pure $\Delta L = 0$, comprise about 84% of the total fitted cross section. Since the exact amounts of $\Delta L = 0$ strength identified in each of the mixed transitions are not listed in reference [25], they were arbitrarily set to 50% with an uncertainty of 50% for this analysis. This estimated $\Delta L > 0$ contribution was then subtracted from the total cross section in the discrete region. In agreement

with reference [25], since these mixed transitions account for just 17% of the total cross section, this introduces an uncertainty of just 2% into the total cross section in the discrete part of the spectra. The resulting sums of cross sections of all the fitted states except the IAS are plotted in figure 6.5. As for ^{51}V and for the individual ^{54}Fe states this rises smoothly with beam energy, leveling off slightly towards 200 MeV. The two datasets at 160 and 200 MeV each are in good agreement with each other.

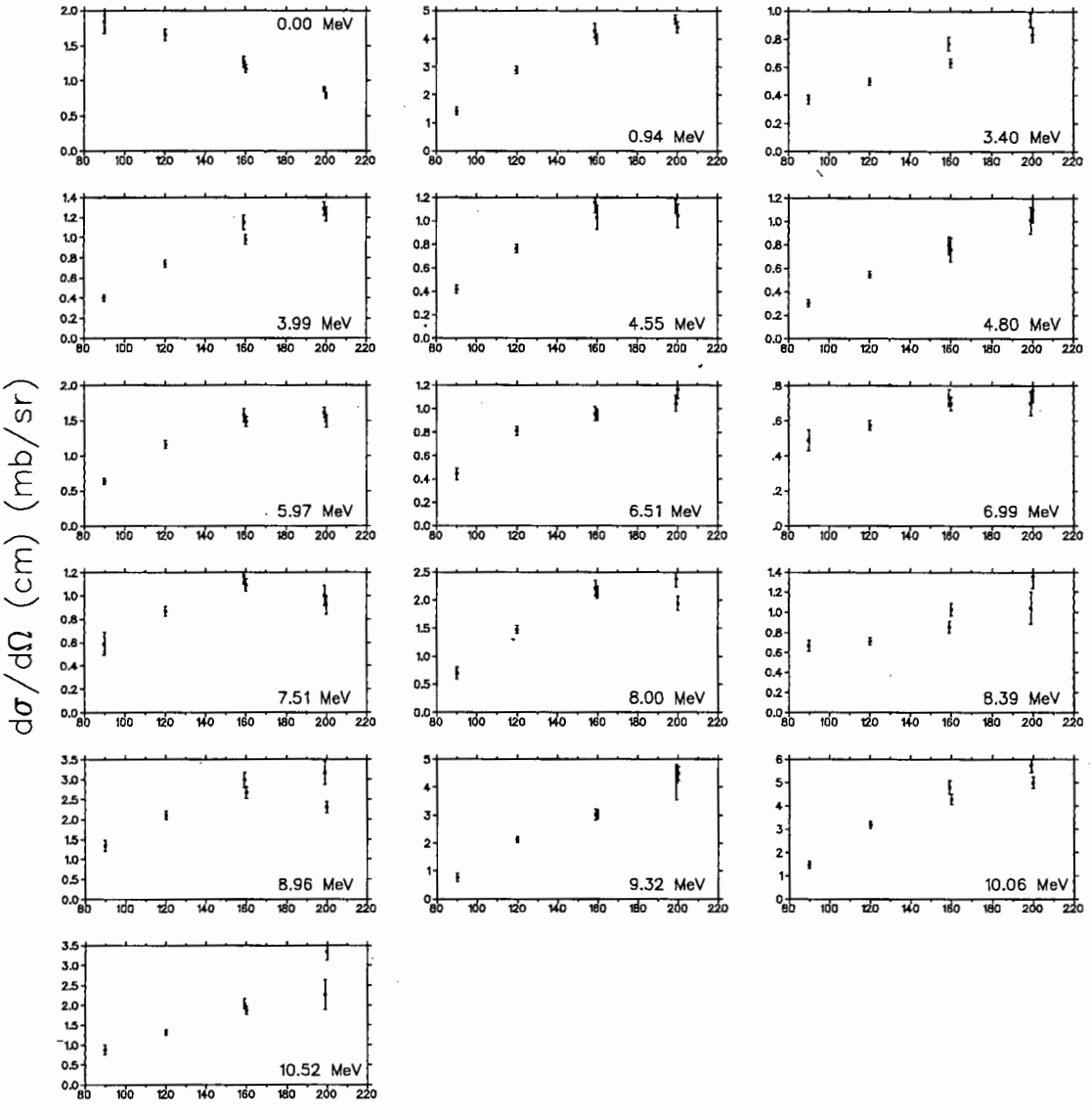

Figure 6.4: Zero degree cross sections as a function of beam energy (in MeV) for some of the transitions in ^{54}Fe$(p,n)^{54}$Co. The top left graph shows the cross section of the ground state IAS transition, and the other plots are for various GT transitions. The excitation energy of the residual nucleus corresponding to each transition is printed in each graph.

As mentioned above, the background below the GT resonance is expected to be mostly GT as illustrated by the result of a multipole decomposition by Vetterli *et al.* [24] on ^{54}Fe(p,n)^{54}Co at 300 MeV, shown in figure 6.6. As done for the ^{51}V data, the $\Delta L = 0$ components of the background were estimated in this analysis by examination of the difference between the 0° and 4° spectra. Figure 6.7 shows overlayed 0° and 4° spectra at 120 and 160 MeV after the 4° spectra had been scaled to the strong $\Delta L = 0$ transition at 0.94 MeV. The shapes of the two spectra are nearly identical in the discrete region and differ only above about 11 MeV in excitation. This indicates that the $\Delta L > 0$ contribution in the continuum region drops off sharply just above $E_x = 11$ MeV. Therefore, a similar procedure to that for ^{51}V was used to estimate the background $\Delta L = 0$ cross section below the GT resonance up to $E_x = 15$ MeV. All strength up to a certain excitation energy was assumed to be $\Delta L = 0$ strength. The point at $E_x = 12$ MeV was selected for this purpose since roughly as much $\Delta L > 0$ strength lies below it as there is $\Delta L = 0$ strength between it and $E_x = 15$ MeV. This then gives the estimate of GT cross section in the spectra up to $E_x = 15$ MeV.

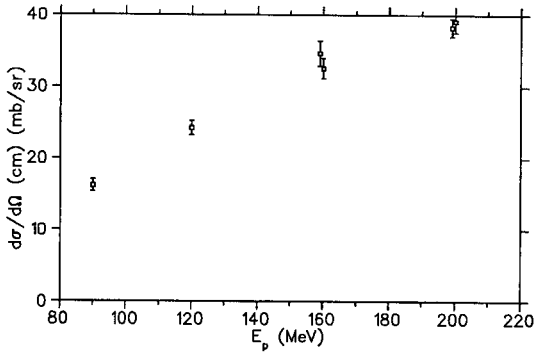

Figure 6.5: Summed zero degree cross sections of all fitted discrete states except the IAS for the ^{54}Fe(p,n)^{54}Co reaction.

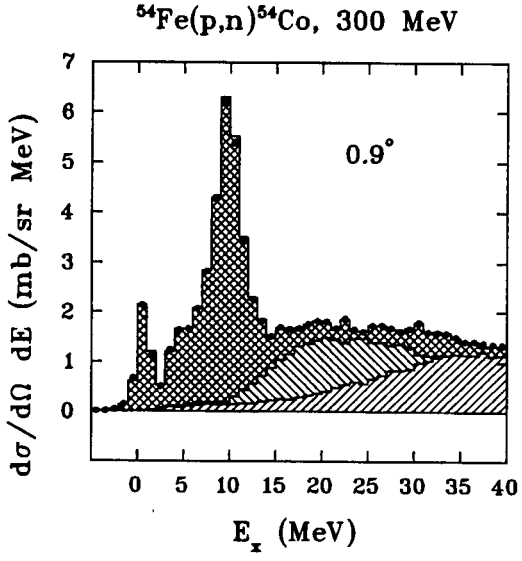

Figure 6.6: Multipole decomposition of ^{54}Fe(p,n)^{54}Co at 300 MeV. From reference [24].

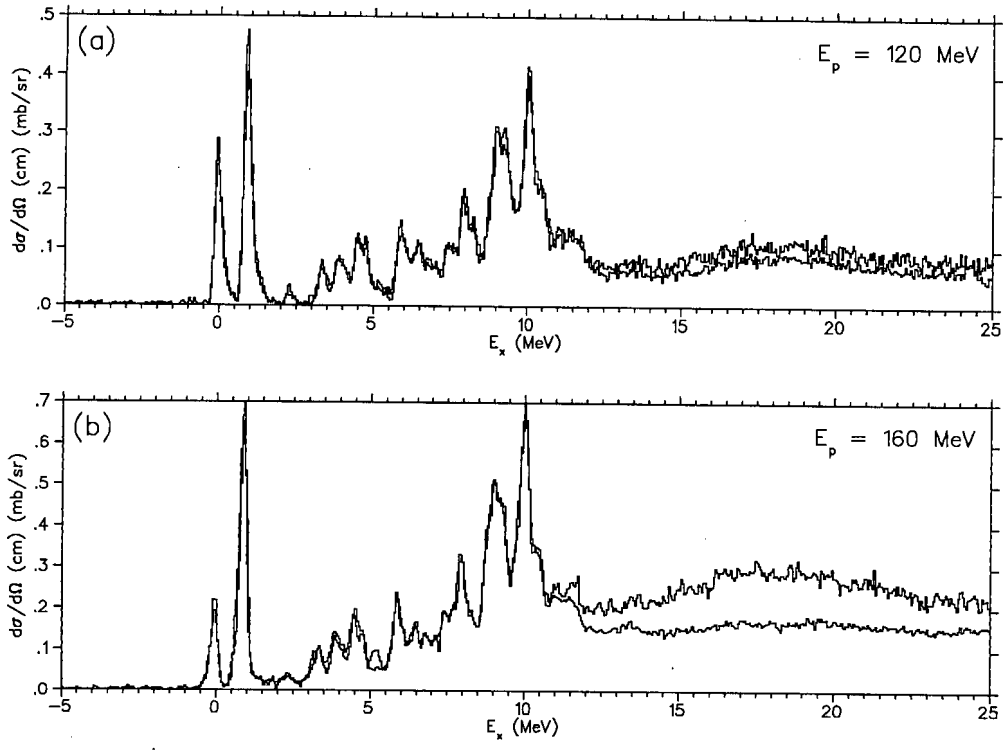

Figure 6.7: Overlays of 0° and scaled 4° ^{54}Fe(p,n)^{54}Co spectra at (a) $E_p = 120$ MeV, and (b) $E_p = 160$ MeV. The 4° spectrum is scaled to the 0° spectrum 0.94 MeV state. In both cases the upper curve at $E_x \geq 15$ MeV is the 4° spectrum.

6.3 Gamow-Teller Strength

No GT beta decay exists against which to calibrate the GT strength in ^{54}Fe(p,n)^{54}Co. However, the 0^+ gs $\rightarrow$ 0^+ gs transition is a pure Fermi transition according to the selection rules of eq. 2.6. The Fermi strength of $N - Z = 2$ is assumed to be concentrated in this state. This is, in fact, seen experimentally; the Fermi beta decay of ^{54}Co gs $\rightarrow$ ^{54}Fe gs has log $ft = 3.484$ [67]. Substitution into eq. 2.2 gives B(F) = 2.02. The GT strength in any transition can therefore be determined relative to the ground state Fermi strength by using Taddeucci's [6, 26] empirically determined ratio of GT to Fermi unit cross sections. This was done according to eq. 2.26. Plots of the GT strength derived in this manner for several of the fitted peaks are presented in figure 6.8. The use of a relative normalisation procedure as applied here and also for ^{51}V has the advantage that systematic uncertainties in the absolute cross sections cancel out, but the disadvantage of sensitivity to errors in the ratio of cross sections. This was seen to be a problem with ^{51}V because the transition to which the others were normalised (the ground state) is a very weak transition and subject to large uncertainty in its cross section. This is not the case, fortunately, for ^{54}Fe. The ground state transition is one of the stronger transitions in the spectrum and cleanly separated from all other transitions (at least for $E_p < 200$ MeV), thereby eliminating any uncertainty from peak deconvolution. Consequently the uncertainty in the extracted strength is mostly dependent on the uncertainties in the ratio $R(E_p, A)^2$ and the cross section of the transition being extracted. Taddeucci *et al.* [6] estimate the former to be about 6%. The summed GT strength in all the fitted discrete structure is plotted against beam energy in figure 6.9a.

Figure 6.9b shows the total measured GT strength in the spectra up to $E_x = 15$ MeV, including both the contribution from the discrete structure and the background beneath the GT resonance. A noticeable feature is that the two points at $E_p = 160$ MeV, which were in excellent agreement in

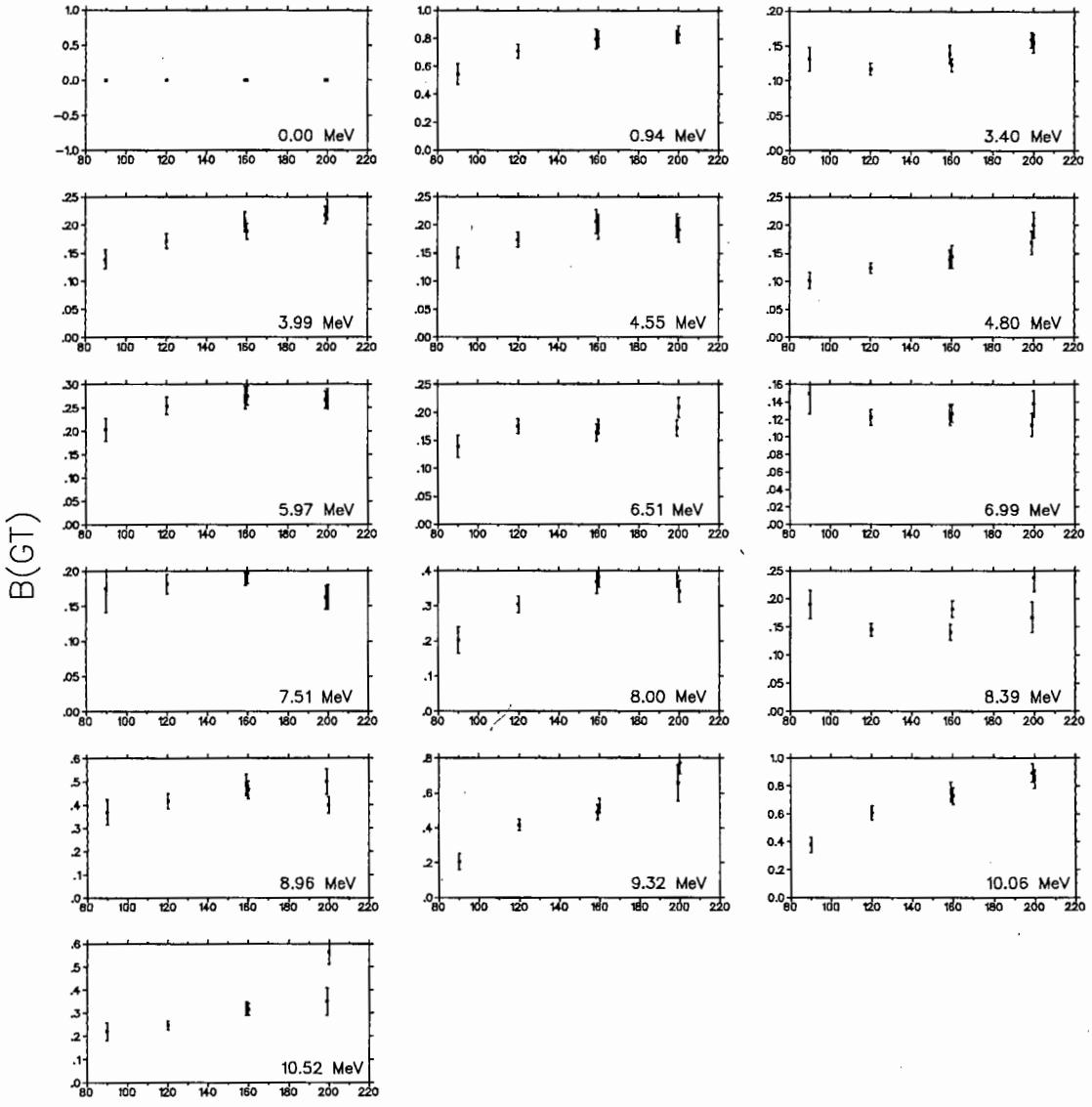

Figure 6.8: GT strengths at the measured beam energies (in MeV) for the same transitions in ^{54}Fe(p,n)^{54}Co as are plotted in figure 6.4. The top left graph represents the IAS transition.

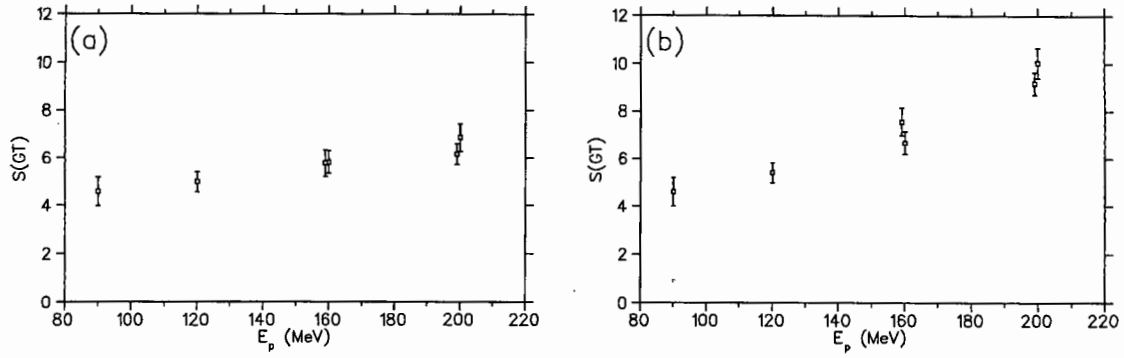

Figure 6.9: Summed GT strength in (a) the discrete structure of ^{54}Fe(p,n)^{54}Co, and (b) the discrete structure plus the background contribution up to E_x = 15 MeV.

figure 6.9a have now separated. This is due to a factor of two difference in the GT contribution from the background of the two datasets, and raises concerns about possible systematic errors due to variations in experimental conditions. The two spectra in question are overlayed on top of one another in figure 6.10. It can be seen that the shapes of the two in the discrete region are nearly identical. However, the continuum region of the one spectrum is approximately double the size of the other. Plotted above the two overlayed spectra is the difference between them. This shows a smooth difference going to zero near the ground state peak. The structure in this difference spectrum is due to the slight difference in resolution between the two spectra. In other words, the same peak has slightly different widths in the two spectra, and when subtracted from each other this results in bumps at the peak edges. This tends to rule out target contamination as a cause of this extra background. If that were the cause, some structure due to the contaminant would be expected. The two likely candidates for contamination of the iron target are oxygen from oxidation in air and carbon from possible contact with grease. These two have reaction Q–values of 7 and 9 MeV greater than ^{54}Fe and should thus show some structure in the spectra above that excitation energy in ^{54}Fe. The particular dataset in question was not the last of the datasets to be acquired. At no time since manufacture was the target subjected to treatment, so any contamination should have shown up in subsequent datasets. It is also hard to imagine a systematic effect with the accelerator, such as protons hitting the beam pipe upstream of the target, as being responsible, since a similar effect was not observed in runs on the vanadium target acquired at the same time. At present the cause of this effect is not understood, and both datasets were included in the analysis.

The Goodman procedure for estimating the $\Delta L = 0$ component of the zero degree spectra, described in more detail in the previous chapter, was also applied to the ^{54}Fe data. The results for 120 and 160 MeV, for which 4° spectra are available, are shown in figure 6.11. This procedure indicates that most of the strength below about 13 MeV is $\Delta L = 0$. As was noted for the ^{51}V case, since the shapes at the two angles differ only in the continuum region, the second step of the procedure, that of scaling the difference by the cross section ratio in the region of the $\Delta L = 1$ resonance at around E_x = 18 MeV and subtracting this from the 0° spectrum, effectively cuts out any strength above the GT resonance. This is in contradiction with the multipole decomposition results of Vetterli *et al.* [24] at 300 MeV which show a fairly constant amount of $\Delta L = 0$ strength extending all the way up to E_x = 40 MeV (see figure 6.6).

The β^+ strength has been measured for ^{54}Fe in an (n,p) reaction at 300 MeV [24]. The summed strength up to E_x = 10 MeV was determined to be $S(\mathrm{GT})^+ = 3.1 \pm 0.6$, which is larger than that for ^{51}V. This is expected since ^{54}Fe has a smaller neutron excess, and consequently should experience less Pauli blocking of β^+ strength. Large uncertainties in the extraction of strength above E_x = 10 MeV restricted the analysis to this limit, despite the results of the multipole decomposition indicating $\Delta L = 0$ strength up to E_x = 40 MeV. Anderson *et al.* [25] measured $S(\mathrm{GT})^- = 6.0 \pm 0.4$

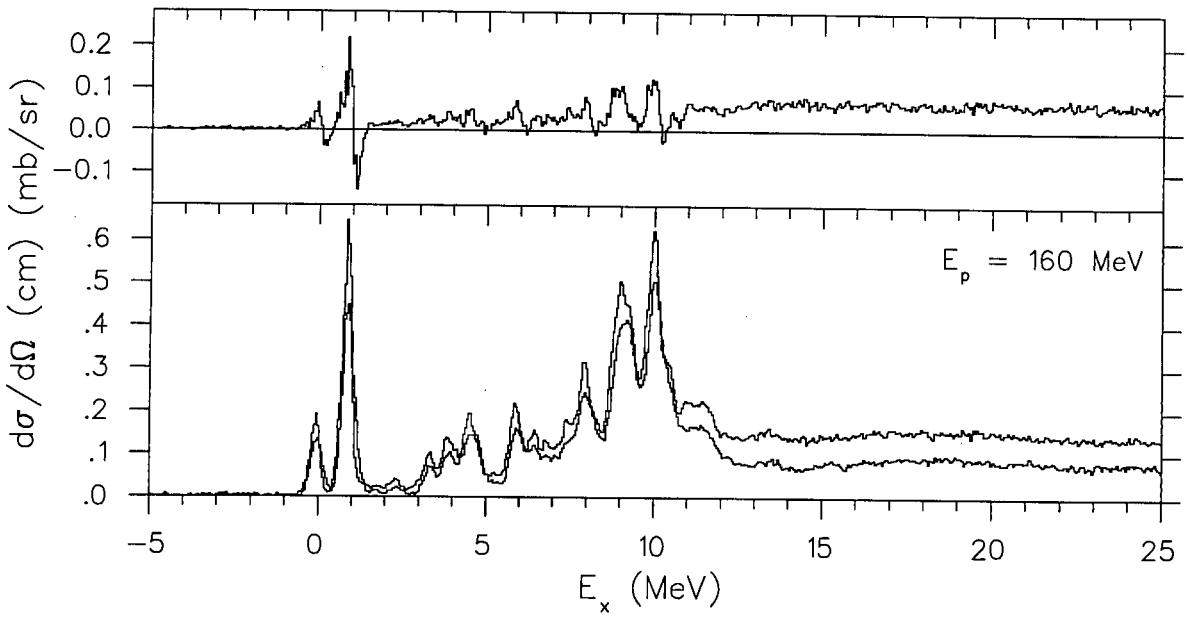

Figure 6.10: Overlayed spectra of the two 0° 160 MeV ^{54}Fe(p,n)^{54}Co datasets showing the larger continuum background of the one. The top graph shows the difference between the two. The structure in the difference is due to the slightly different resolution of the two spectra.

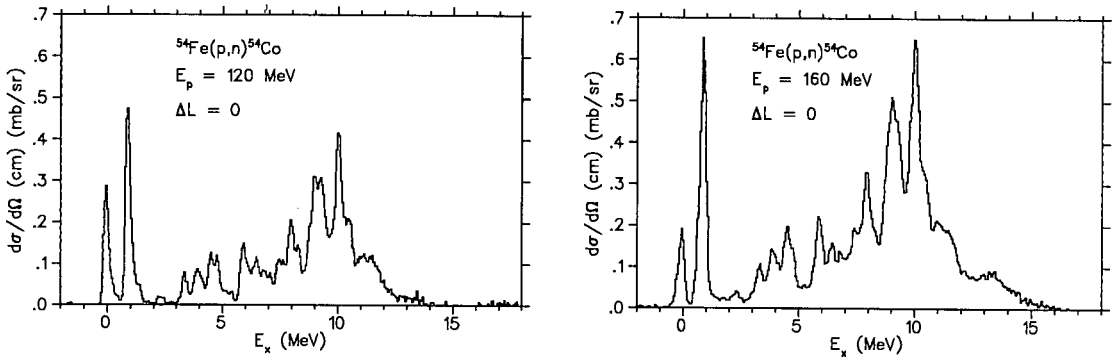

Figure 6.11: Estimated $\Delta L = 0$ component of the zero degree ^{54}Fe(p,n)^{54}Co spectra at E_p = 120 and 160 MeV.

for the discrete states only at E_p = 135 MeV. For the sum of this and the background up to E_x = 24 MeV they obtain $S(\mathrm{GT})^- = 7.5 \pm 0.7$ after subtraction of a calculated quasifree scattering component. This is in good agreement with the values of $S(\mathrm{GT})^- = 7.8 \pm 1.9$ up to 14 MeV and $S(\mathrm{GT})^- = 7.5 \pm 1.2$ up to 15 MeV reported by Rapaport *et al.* [23] and Vetterli *et al.* [24] at E_p = 160 and 300 MeV respectively. Anderson *et al.* [25] claim that their value is an underestimate of the GT contribution to the background and continuum because the quasifree scattering calculation contains some unidentified strength. They reported a multipole decomposition analysis of the full background which yielded $S(\mathrm{GT})^- = 10.3 \pm 1.4$ up to E_x = 24 MeV, although they believe that to be an overestimate.

In this work the average of the two values at E_p = 200 MeV gives the maximum value of $S(\mathrm{GT})^- = 6.5 \pm 0.4$ for the strength in the discrete states, in good agreement with that of Anderson *et al.* [25]. This can account for the minimum value of $3(N - Z) = 6$ predicted by the sum rule. Including the measured $S(\mathrm{GT})^+$ quoted above, results in a maximum quenching factor of $Q = 0.57$, where Q is the ratio of measured to predicted values of the GT sum rule. Inclusion of the background

estimate pushes Q up to just over 1.0. Bearing in mind the large uncertainties associated with the background strength estimate and the fact that there is probably neglected strength in both the (n,p) and (p,n) directions above the excitation energy limits of the respective analyses, it is quite possible that all the strength predicted by the sum rule is present in the observed spectra (at least at the higher beam energies). In other words, it may be possible to account for all the predicted strength with mechanisms such as configuration mixing, and without resorting to sub-nucleonic degrees of freedom. The values of Q obtained from the $S(\mathrm{GT})^-$ of this analysis combined with the $S(\mathrm{GT})^+$ of Vetterli *et al.* [24] are plotted in figure 6.12.

The numbers corresponding to the data plotted in figures 6.9 and 6.12 are presented in table 6.1.

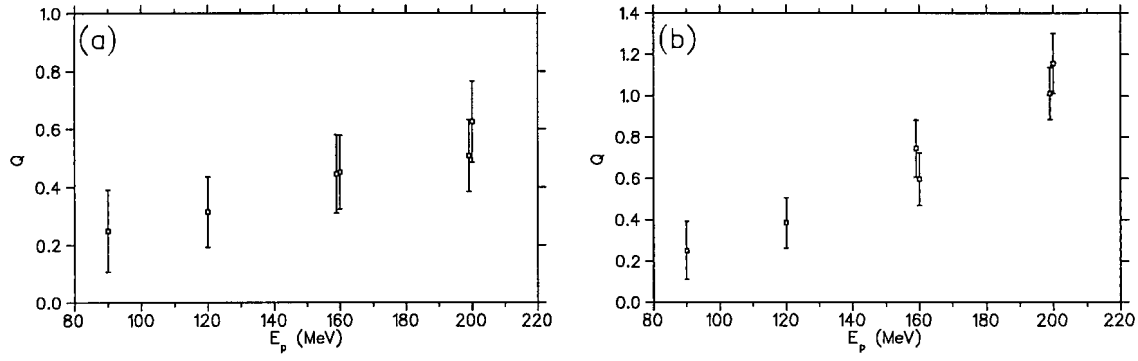

Figure 6.12: The Gamow-Teller sum rule quenching factors $Q = (S(\mathrm{GT})^- - S(\mathrm{GT})^+)/3(N-Z)$ for ^{54}Fe$(p,n)^{54}$Co if (a) only the strength in the discrete region is considered, and (b) if the strength in the background below the GT resonance is included.

E_p (MeV)	$S(\mathrm{GT})^-$ Discrete states	$Q^\dagger$	$S(\mathrm{GT})^-$ (0 – 15 MeV) Discrete + background	$Q^\ddagger$
90	4.59 ± 0.60	0.25 ± 0.14	4.61 ± 0.60	0.25 ± 0.14
120	4.98 ± 0.42	0.31 ± 0.12	5.41 ± 0.42	0.38 ± 0.12
160	5.77 ± 0.56	0.45 ± 0.14	7.57 ± 0.57	0.75 ± 0.14
160	5.81 ± 0.47	0.45 ± 0.13	6.68 ± 0.48	0.60 ± 0.13
200	6.15 ± 0.44	0.51 ± 0.12	9.18 ± 0.47	1.01 ± 0.13
200	6.85 ± 0.58	0.63 ± 0.14	10.04 ± 0.62	1.16 ± 0.14

Table 6.1: The total GT strength in the discrete region, the quenching factor $Q^\dagger$ assuming the total GT strength is that in column 2, the total GT strength in the discrete region plus the background under the GT resonance, and the quenching factor $Q^\ddagger$ assuming that the total GT strength is that in column 4, for ^{54}Fe$(p,n)^{54}$Co at the four measured beam energies.

It is clear, though, that a thorough multipole decomposition requiring a more extensive angular distribution is required to handle the issue of the strength in the continuum. This can determine the total $\Delta L = 0$ strength in the spectrum but, as pointed out by Anderson *et al.* [68], if there is a quasifree component in the spectrum then there can be some $\Delta L = 0$ strength which is not GT strength. It becomes no longer possible to identify the GT strength uniquely from the cross section data alone, and the problem becomes model-dependent.

Chapter 7

^{59}Co(p,n)^{59}Ni Analysis

7.1 Fits to the Spectra

Zero degree time-of-flight spectra for ^{59}Co(p,n)^{59}Ni at the four measured beam energies are presented in figure 7.1. These spectra are the complete TOF spectra for a particular dataset. They comprise the sum of all runs in that dataset after those runs had been normalised to a common time scale and each section shifted into alignment with each other as described in section 4.1.

After accumulation into the TOF spectra, the slow neutron wraparound background was removed as described in section 4.2 and a fit was made to the discrete states as described in section 4.3. The IAS at 7.2 MeV sits on top of a GT background and is extracted before all the other discrete states are fitted, as was the case with ^{51}V. In this case too there is an asymmetric shoulder on the right hand side of the peak which is most prominent at 120 MeV, and which is attributed to an unresolved GT transition. The deconvolution of these two peaks introduces a small statistical uncertainty into the extracted yields. Once again there is a systematic uncertainty due to the selection of the GT background shape. In this case, as opposed to the ^{51}V case, the peaks on either side of the IAS are not resolved from each other and this results in a smoother shape. Consequently there is a smaller uncertainty in the background fit. This uncertainty is also a function of beam energy since the IAS cross section decreases with energy. The systematic uncertainty in the IAS yield is estimated to range from 2% at 90 MeV to 10% at 200 MeV. In all cases this amounts to much less than 1% in the total GT cross section. After the IAS peak was fitted, the parameters of the fit were fixed and the rest of the discrete states were extracted. Selection of which peaks to fit was made on the principle of using as few peaks as possible to adequately reproduce the discrete part of the spectra. The same set of peaks was used to fit the spectra up to E_x = 18 MeV at all angles and beam energies for the particular target. In order to obtain good fits to the ^{59}Co spectra it was necessary to fit 26 peaks to the data. The results of the wraparound removal and the fits to the 0° data are shown in figure 7.2. The first excited state at 0.34 MeV and the IAS at 7.2 MeV [69, 70] were then used to determine the time-to-energy calibration and to convert the TOF spectra to excitation energy spectra as described in section 4.3.

The differential cross section was then calculated for each transition as described in section 4.4 and also for each bin in the excitation energy spectra. The resulting double differential cross sections are plotted in figure 7.3.

The ^{59}Co ground state has $J^\pi = \frac{7}{2}^-$ and the ^{59}Ni ground state has $J^\pi = \frac{3}{2}^-$ and is, therefore, unreachable because of the selection rules given in eq. 2.6. The first excited state with $J^\pi = \frac{5}{2}^-$ at 0.34 MeV is possible to reach via the (p,n) reaction and is seen, for example, at ~channel 118 in figure 7.1b. It is a very weak GT transition, but stronger ones are seen in two main groupings

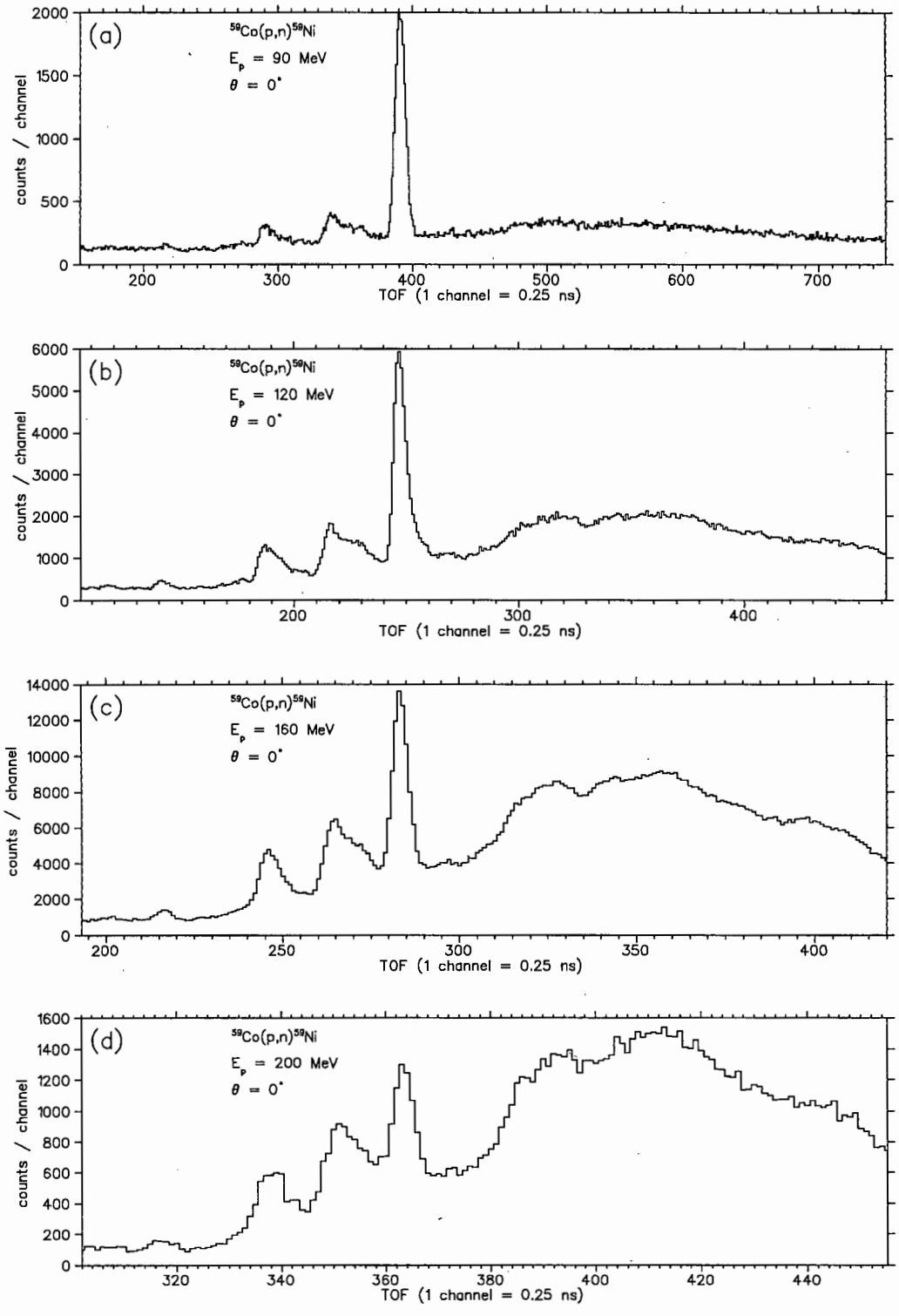

Figure 7.1: The ^{59}Co(p,n)^{59}Ni TOF spectra at beam energies from 90 to 200 MeV.

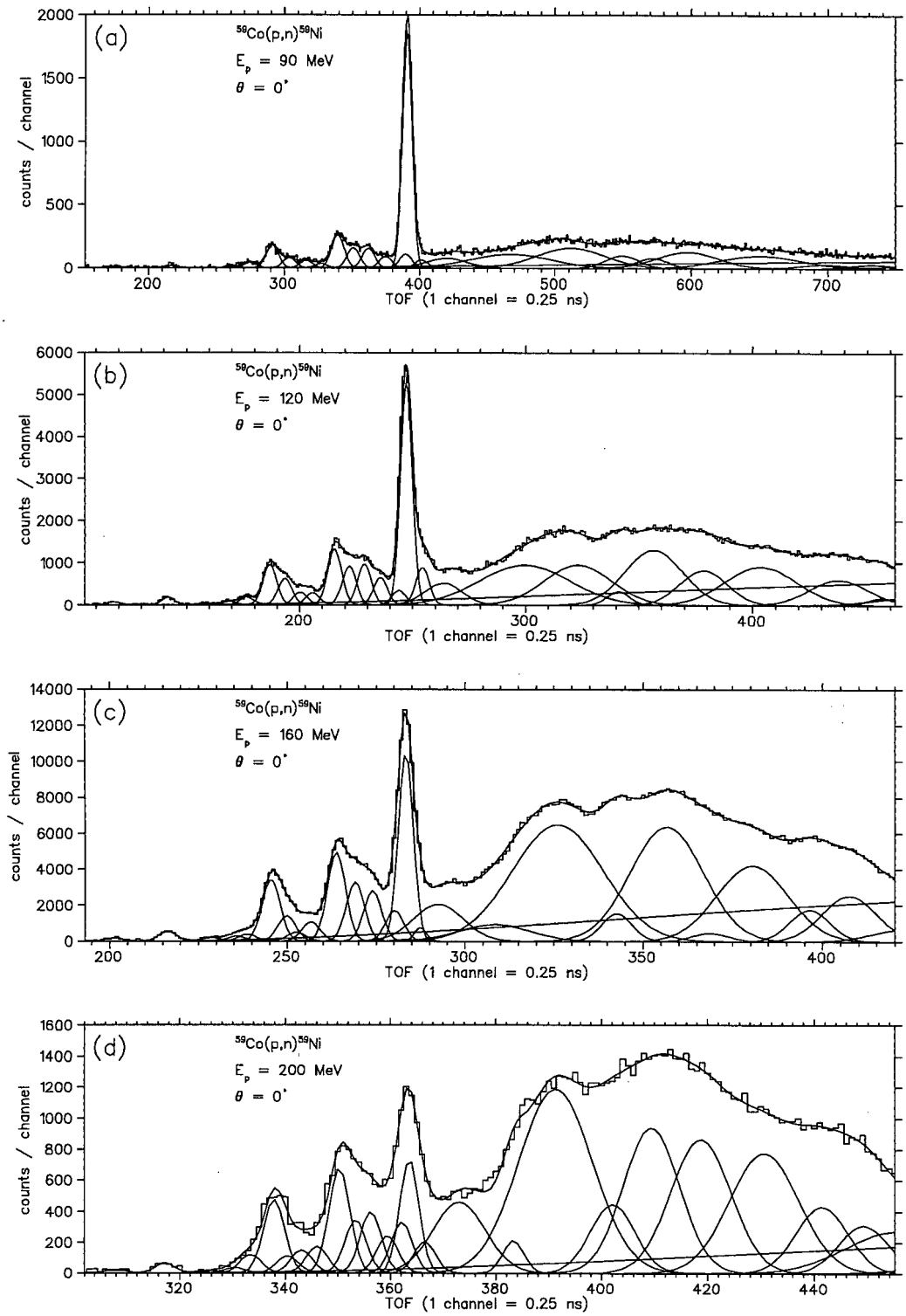

Figure 7.2: The background and peak fits to the ^{59}Co(p,n)^{59}Ni TOF spectra at the four beam energies.

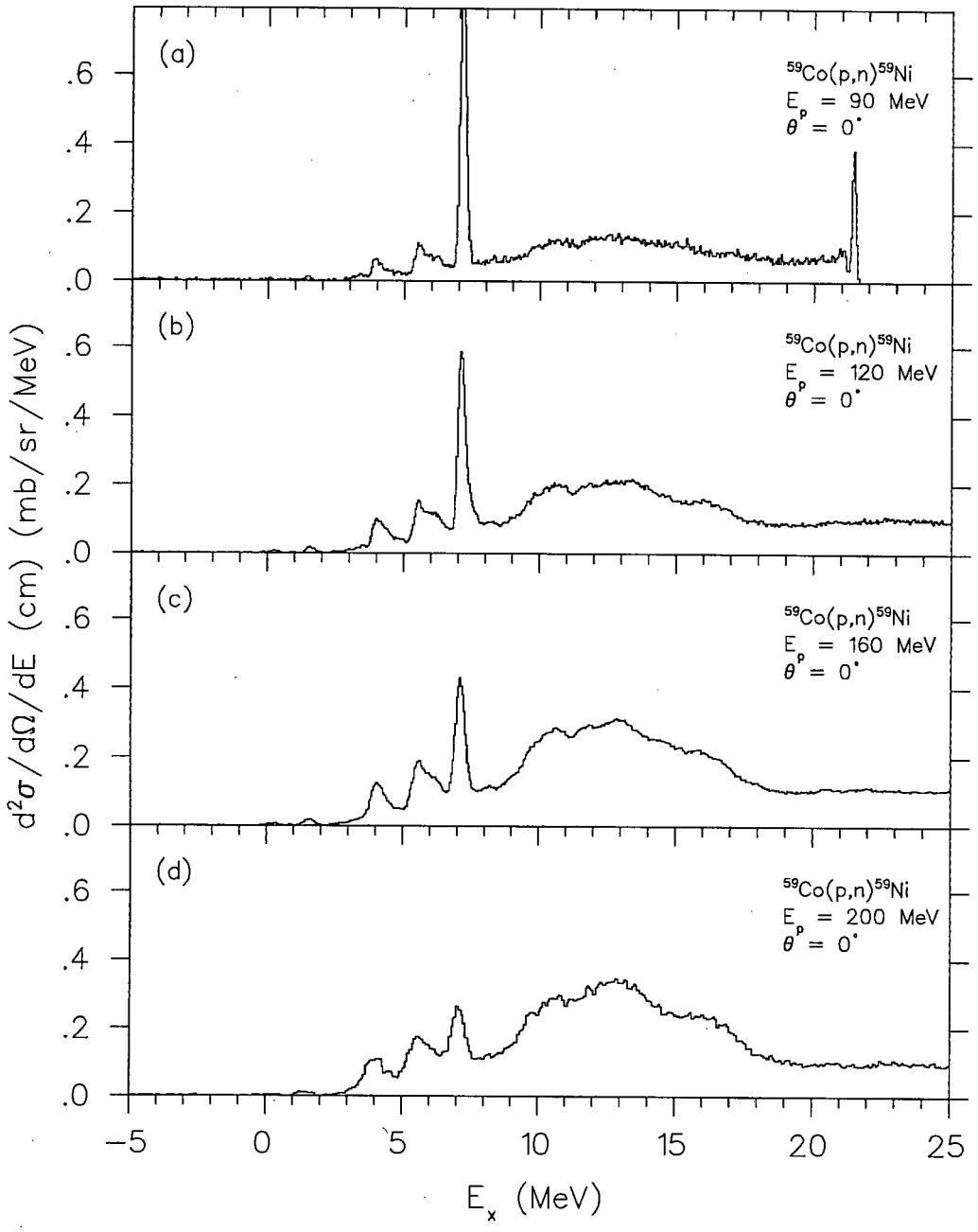

Figure 7.3: Double differential cm cross sections for ^{59}Co(p,n)^{59}Ni as a function of excitation energy of the residual nucleus. The sharp peak at $E_x \sim 21.5$ MeV in (a) is spurious (see the text for details).

at ~4 MeV and ~6 MeV and in the GT resonance centered at ~13 MeV. The IAS transition at ~channel 390 in figure 7.1a is very strong at low beam energy and decreases with increasing beam energy. The rest of the cross section, assumed to correspond mostly to GT strength, is seen in figure 7.3 to increase with beam energy, both relative to the IAS cross section and in absolute terms. In general, the density of excited states appears to be higher for ^{59}Co(p,n)^{59}Ni than for the other two reactions studied, and only the IAS and the first two excited states are resolved. Little confidence can, therefore, be put in the assignment of the fitted peaks to individual states. It is possible that many of the fitted peaks represent groups of excited states. As with the other two targets, the sharp peaks at the far right of the spectra (eq. at $E_x \sim 21.5$ MeV in figure 7.3a) are an artifact of the electronic signal processing. Full results of the fits to the individual transitions, including excitation energies, cross sections, and GT strengths, are tabulated in appendix A.

7.2 Cross Sections

Cross sections for a few of the more prominent fitted peaks are presented in figure 7.4. Two datasets were acquired at $E_p = 200$ MeV and the cross sections from the two are seen to be in good agreement with each other considering the lack of resolution between the fitted peaks. In particular, the two points corresponding to the single well resolved, strong transition (the IAS, presented in the top left graph of figure 7.4) are in excellent agreement with each other. The systematics of the Fermi and Gamow-Teller components with beam energy are very similar to that of the ^{51}V(p,n)^{51}Cr and ^{54}Fe(p,n)^{54}Co reactions. The decrease in the IAS cross section as the beam energy increases (approximately a factor of two between 90 and 200 MeV) is very similar to that of ^{51}V and ^{54}Fe and indicative of Fermi strength. Although the transition to the IAS is $\frac{7}{2}^- \longrightarrow \frac{7}{2}^-$, and may thus contain Fermi and GT strength, the behaviour of the cross section suggests that the amount of GT strength in this transition is small. This is discussed further below. The sum of cross sections of all the fitted peaks except the IAS is plotted in figure 7.5. It increases smoothly between 90 and 200 MeV by a factor of about four. These systematics are again very similar to those seen in ^{51}V and ^{54}Fe.

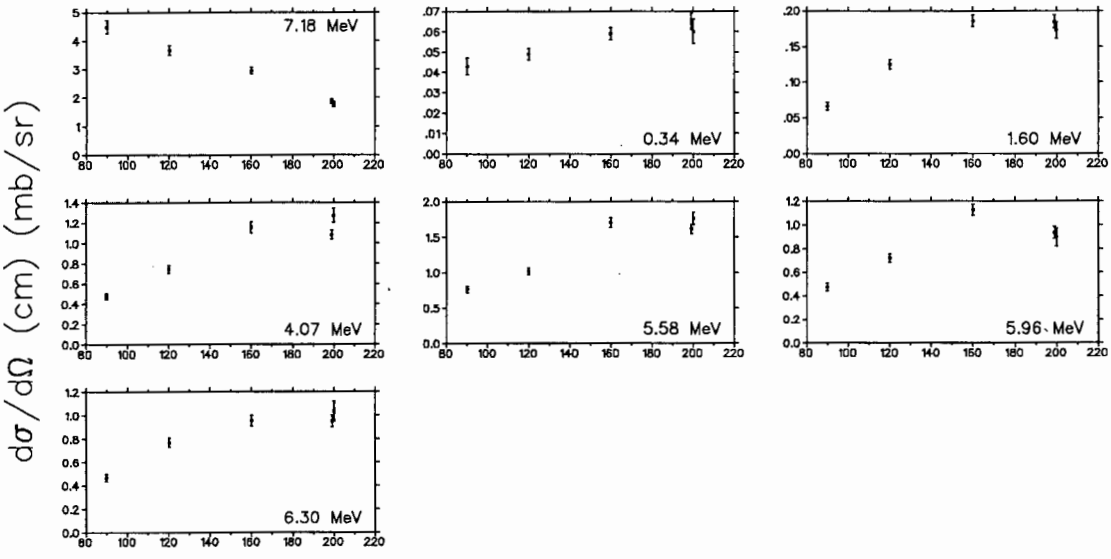

Figure 7.4: Zero degree cross sections as a function of beam energy (in MeV) for some of the transitions in ^{59}Co(p,n)^{59}Ni. The top left graph shows the cross section of the IAS transition, and the other plots are for various GT transitions. The excitation energy of the residual nucleus corresponding to each transition is printed in each graph.

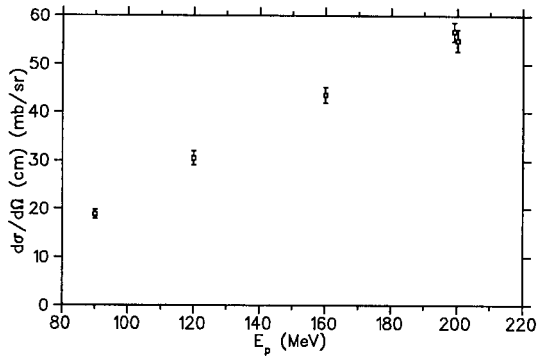

Figure 7.5: Summed zero degree cross sections of all fitted discrete states for the ^{59}Co(p,n)^{59}Ni reaction, excluding the IAS.

7.3 Gamow-Teller Strength

The estimates of $\Delta L = 0$ strength in the ^{59}Co(p,n)^{59}Ni spectra have been made in the same manner as for ^{51}V(p,n)^{51}Cr and ^{54}Fe(p,n)^{54}Co. No previous analysis of $\Delta L = 0$ strength in ^{59}Co(p,n)^{59}Ni has been published. A proper multipole decomposition is very desirable, and future work on this target should include a more complete angular distribution for this purpose. However, in the absence thereof, the data have been subjected to the same analysis as the ^{51}V data. The spectra are seen to be extremely similar to the ^{51}V(p,n)^{51}Cr spectra, with the IAS and GT resonances at excitations within about 1 MeV of each other and having very similar strength distributions. Only one 4° point was acquired for ^{59}Co(p,n)^{59}Ni, that at $E_p = 200$ MeV. This is shown scaled to the IAS cross section and overlayed on top of the zero degree spectrum in figure 7.6. Once again the difference between the two spectra is seen to be primarily in the continuum region, and extending down to $E_x \approx 13$ MeV. This may be compared with figure 5.7 to show how similar the behaviour is in the two reactions. In the light of this it was decided to integrate the background up to the same energy as for ^{51}V (ie. $E_x = 18$ MeV) in order to estimate the $\Delta L = 0$ contribution in the background beneath the GT resonance. This leads to the exclusion of roughly as much $\Delta L = 0$ cross section above 18 MeV as the inclusion of $\Delta L > 0$ cross section below it. Clearly there is a large systematic uncertainty associated with this estimate. The errors quoted with the results of the estimate are statistical only. Figure 7.7 shows the estimated $\Delta L = 0$ strength distribution in ^{59}Co(p,n)^{59}Ni obtained from the subtraction of the scaled difference between the 0° and 4° spectra at 200 MeV according to Goodman's procedure [4]. Once again, this is very similar to that obtained for ^{51}V(p,n)^{51}Cr shown in figure 5.11.

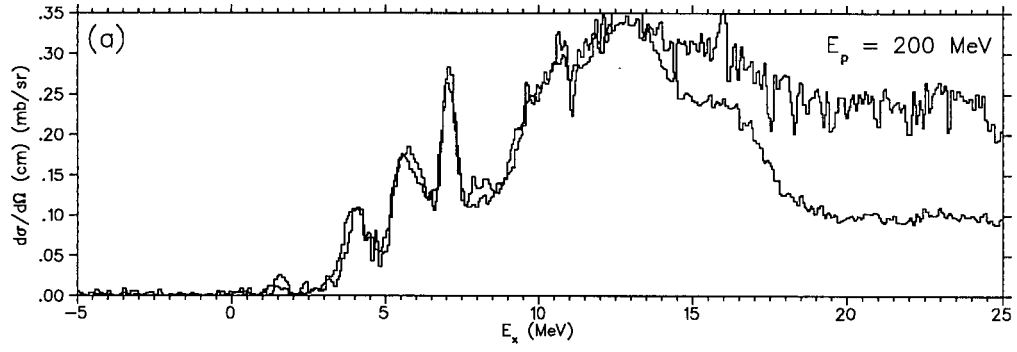

Figure 7.6: Overlays of the 0° and scaled 4° ^{59}Co(p,n)^{59}Ni spectra at $E_p = 200$ MeV. The scaling is done by the cross section of the IAS at $E_x = 7.2$ MeV. The upper curve is the 4° spectrum.

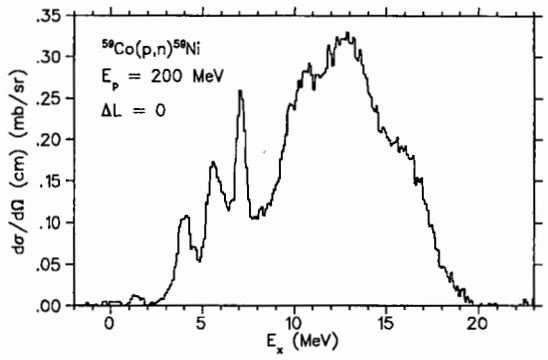

Figure 7.7: Estimated $\Delta L = 0$ component of the zero degree ^{59}Co$(p,n)^{59}$Ni spectrum at $E_p = 200$ MeV.

The ground state of ^{59}Co is $\frac{7}{2}^-$. By the selection rules of eq. 2.6 the IAS transition contains a mixture of Fermi and GT strength. Although the Fermi strength $B(\mathrm{F}) = N - Z = 5$ is known and assumed concentrated in the IAS, the empirically derived ratio $R(E_p, A)^2$ of GT to Fermi strengths cannot be used to calculate the GT strengths unless the fraction of GT strength in the IAS, f_{GT}, is known. Unfortunately there exists no GT beta decay against which to calibrate other GT transition strengths. This is strong motivation for a polarised beam experiment on ^{59}Co so that f_{GT} may be independently obtained from the transverse spin polarisation transfer coefficient D_{NN}. In the absence of this one is forced to use calculated GT unit cross sections with their large associated uncertainties, as discussed in section 2.8 in order to determine $B(\mathrm{GT})$.

GT unit cross sections were obtained from the DWIA calculations of Taddeucci *et al.* [6] as plotted in figure 2.2. Because of the large variation in GT unit cross section between targets, uncertainties of 30% were assigned to the values read off from the graphs. No calculations have been published for $E_p = 90$ MeV, so the analysis is restricted to the other three energies. The following values were used:

E_p (MeV)	$\hat{\sigma}_{\mathrm{GT}}$(mb/sr)
120	4.1 ± 1.2
160	5.1 ± 1.5
200	5.0 ± 1.5

Table 7.1: GT unit cross sections obtained from figure 2.2 for $A = 59$.

The GT strengths were then calculated according to eq. 2.27 and the GT strength in the IAS transition according to eq. 2.28. This was done under the assumption that all the fitted peaks, with the exception of the IAS, correspond to pure GT transitions. A proper multipole decomposition is needed to check this assumption. The strengths obtained for the selected transitions shown in figure 7.4 are presented in figure 7.8. The large error bars resulting from the uncertainties in the GT unit cross sections means that these results could be consistent with no dependence on beam energy, in disagreement with what is seen for the other two targets. As with ^{51}V the fraction of GT strength in the IAS, f_{GT}, is calculated to be negative. However, the large uncertainties in these values mean that they are consistent with $f_{\mathrm{GT}} = 0$ and, in fact, with $f_{\mathrm{GT}} \leq 0.15$. This agrees with the suspicion, mentioned above, that f_{GT} is small. The values of f_{GT} are plotted in figure 7.9. Because of this, the GT strengths in the IAS transitions are set to their minimum value of zero. The summed strength in the discrete transitions is plotted in figure 7.10 with and without the estimated contribution from the background under the GT resonance.

The β^+ strength in ^{59}Co has been measured [65] and found to be $S(\mathrm{GT})^+ = 1.9 \pm 0.1$ up to 8 MeV

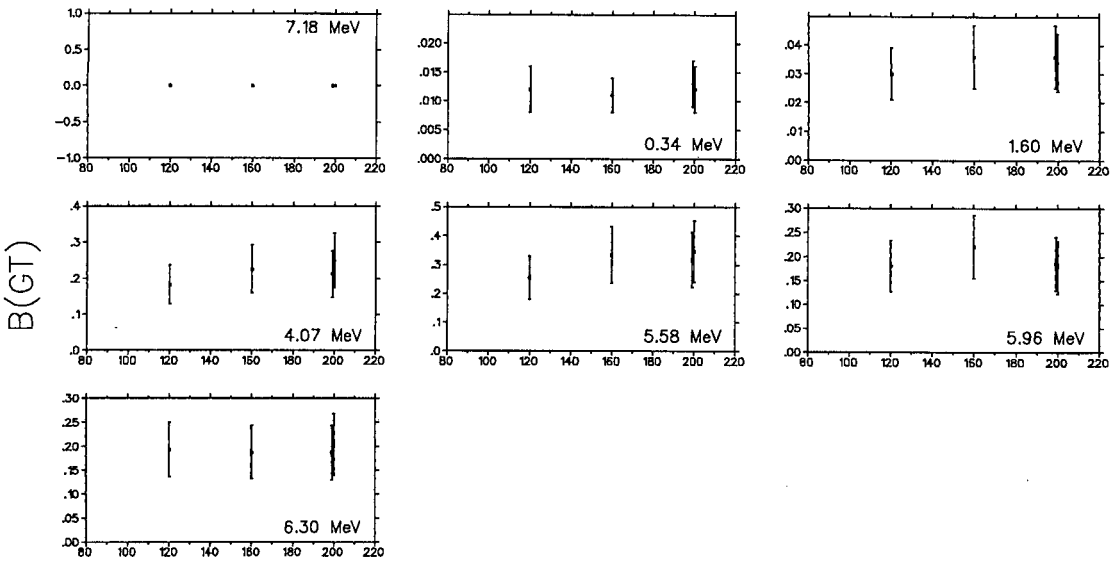

Figure 7.8: GT strengths for a few of the transitions in ^{59}Co(p,n)^{59}Ni at the measured beam energies (in MeV).

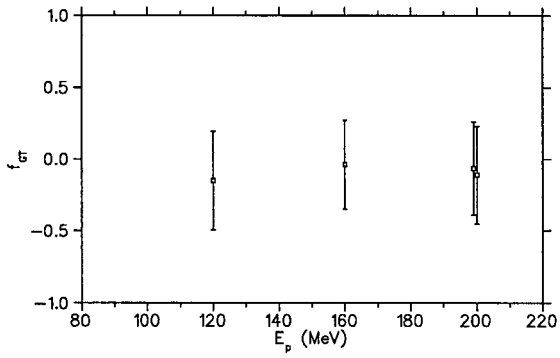

Figure 7.9: Calculated fraction of GT strength in the ^{59}Co(p,n)^{59}Ni IAS transition.

in excitation energy. Putting this into the GT sum rule along with the $S(\mathrm{GT})^-$ values of figure 7.10 allows the calculation of the quenching factor Q, where Q is the ratio of measured to predicted values of the GT sum rule. These are plotted in figure 7.11. With the exception of the 200 MeV points the total GT strength falls short of the minimum value of $3(N-Z)$.

The numbers corresponding to the data plotted in figures 7.9, 7.10 and 7.11 are presented in table 7.2.

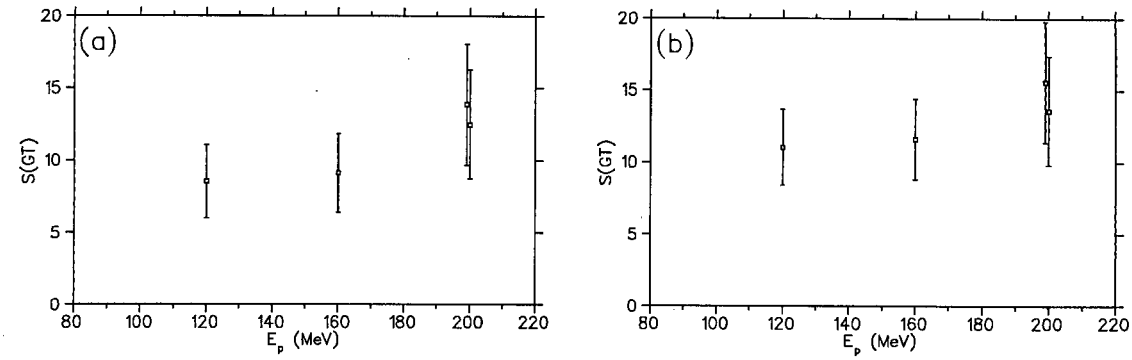

Figure 7.10: Summed GT strength in (a) the discrete structure of ^{59}Co(p,n)^{59}Ni, and (b) the discrete structure plus the background contribution up to $E_x = 20$ MeV.

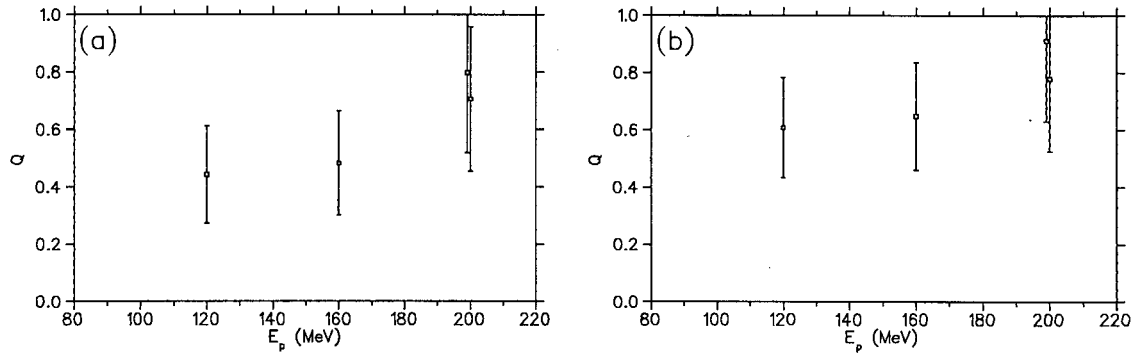

Figure 7.11: The Gamow-Teller sum rule quenching factors $Q = (S(\mathrm{GT})^- - S(\mathrm{GT})^+)/3(N-Z)$ for ^{59}Co(p,n)^{59}Ni if (a) only the strength in the discrete region is considered, and (b) if the strength in the background below the GT resonance is included.

E_p (MeV)	f_{GT}	$S(\mathrm{GT})^-$ Discrete states	$Q^\dagger$	$S(\mathrm{GT})^-$ (0 – 20 MeV) Discrete + background	$Q^\ddagger$
120	-0.15 ± 0.34	8.53 ± 2.53	0.44 ± 0.17	11.03 ± 2.64	0.61 ± 0.18
160	-0.04 ± 0.31	9.13 ± 2.71	0.48 ± 0.18	11.62 ± 2.81	0.65 ± 0.19
200	-0.06 ± 0.32	13.87 ± 4.19	0.80 ± 0.28	15.58 ± 4.22	0.91 ± 0.28
200	-0.11 ± 0.34	12.49 ± 3.78	0.71 ± 0.25	13.58 ± 3.79	0.78 ± 0.25

Table 7.2: The calculated fraction of GT strength in the IAS, the total GT strength in the discrete region, the quenching factor $Q^\dagger$ assuming the total GT strength is that in column 3, the total GT strength in the discrete region plus the background under the GT resonance, and the quenching factor $Q^\ddagger$ assuming that the total GT strength is that in column 5, for ^{59}Co(p,n)^{59}Ni at beam energies ≥ 120 MeV.

7.4 Alternate Gamow-Teller Strength Calculation

The large uncertainties in the above results, originating from the GT unit cross sections, make it difficult to draw any definite conclusions from them. The reason that the unit cross sections were employed was that no GT beta decay exists against which to calibrate the GT strength, and that the fraction of GT strength in the IAS transition is unknown, so that the GT strength cannot be normalised to the Fermi strength. However, the evidence indicated that the fraction of GT strength in the IAS transition was small. The four points in figure 7.9 are consistent with $f_{GT} \leq 0.15$. If it is assumed that f_{GT} is known, then the cross section in the IAS that is due to Fermi strength is known and the GT strength can be obtained relative to this according to eq. 2.26. This has been done making the assumption that $f_{GT} = 0.00 \pm 0.15$. In other words it is assumed that the IAS is a pure Fermi transition with an uncertainty of 15% given by the maximum value of f_{GT} consistent with the results in figure 7.9. The results are presented below in table 7.3 and plotted in figures 7.12 to 7.14. The point at $E_p = 90$ MeV, which was excluded because no GT unit cross section has been calculated at that energy, has now been included.

E_p (MeV)	f_{GT}	$S(GT)^-$ Discrete states	$Q^\dagger$	$S(GT)^-$ (0 – 20 MeV) Discrete + background	$Q^\ddagger$
90	0.00 ± 0.15	6.69 ± 0.50	0.32 ± 0.03	8.18 ± 0.52	0.42 ± 0.04
120	0.00 ± 0.15	7.89 ± 0.55	0.40 ± 0.04	10.36 ± 0.57	0.56 ± 0.04
160	0.00 ± 0.15	8.21 ± 0.49	0.42 ± 0.03	10.52 ± 0.51	0.57 ± 0.03
200	0.00 ± 0.15	12.75 ± 0.89	0.72 ± 0.06	14.42 ± 0.90	0.83 ± 0.06
200	0.00 ± 0.15	12.18 ± 0.99	0.69 ± 0.07	13.29 ± 0.99	0.76 ± 0.07

Table 7.3: The calculated fraction of GT strength in the IAS, the total GT strength in the discrete region, the quenching factor $Q^\dagger$ assuming the total GT strength is that in column 3, the total GT strength in the discrete region plus the background under the GT resonance, and the quenching factor $Q^\ddagger$ assuming that the total GT strength is that in column 5, for ^{59}Co(p,n)^{59}Ni at the four measured beam energies if the IAS is assumed to be a pure Fermi transition.

The GT strengths are now extracted relative to the IAS Fermi strength and depend on the ratio of GT to Fermi cross sections. The IAS transition is a strong transition which is well resolved from the surrounding GT cross section. The uncertainties in the extracted cross sections are, therefore, quite small, as is seen in figure 7.4. This is propagated through to the calculated GT strengths and the uncertainties are seen to be significantly smaller than the previous ones. The new points, though, are all in quite good agreement with the old ones, and certainly all within the old, large uncertainties. This suggests firstly that the estimates of the GT unit cross sections were not too far off the mark, ie. the DWIA calculations of Taddeucci *et al.* [6] work quite well for ^{59}Co, and secondly that the estimate of $f_{GT} = 0$ is also not too far off. The GT strengths plotted in figures 7.12 and 7.13 confirm the earlier impression that the energy dependence observed in the other two targets is not nearly so strong in ^{59}Co. The strengths of the stronger transitions shown in figure 7.12 indicate almost no energy dependence. The total strengths shown in figure 7.13 do increase with increasing beam energy, but the dependence is certainly weaker than in the other targets. Since the IAS cross section attributed to Fermi strength is inversely proportional to f_{GT}, eq. 2.26 shows that the GT strengths obtained in this manner are proportional to f_{GT}. If f_{GT} were as high as just 0.2, instead of zero as assumed above, this would push the average 200 MeV value of Q in column 6 of table 7.3 up to unity. In other words, if just 20% of the IAS transition strength is GT strength, then the sum rule prediction can be satisfied by strength in the visible spectrum.

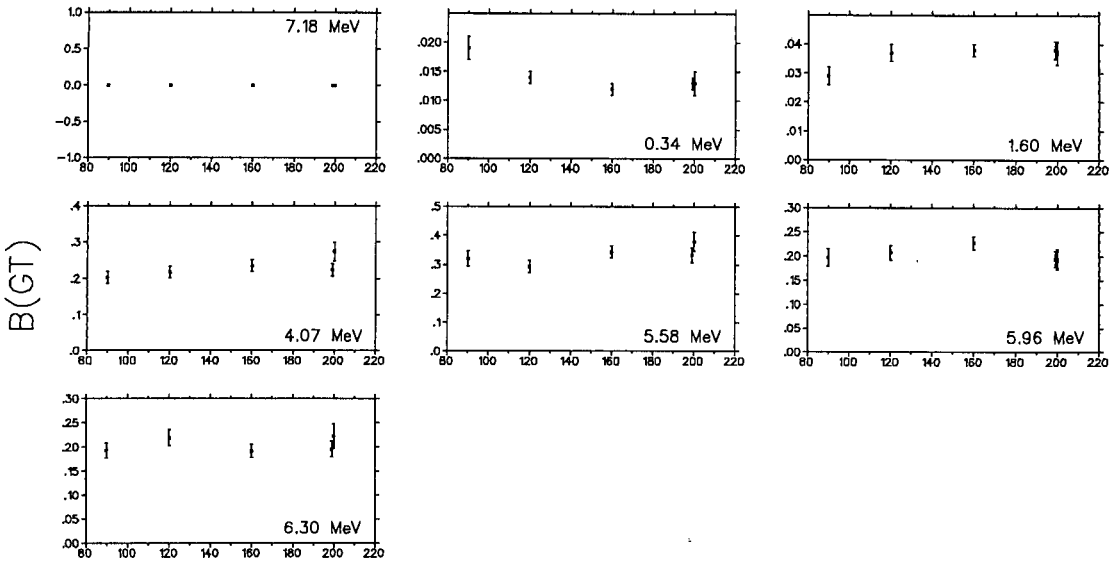

Figure 7.12: GT strengths for a few of the transitions in ^{59}Co(p,n)^{59}Ni at the measured beam energies (in MeV), assuming that the IAS is a pure Fermi transition.

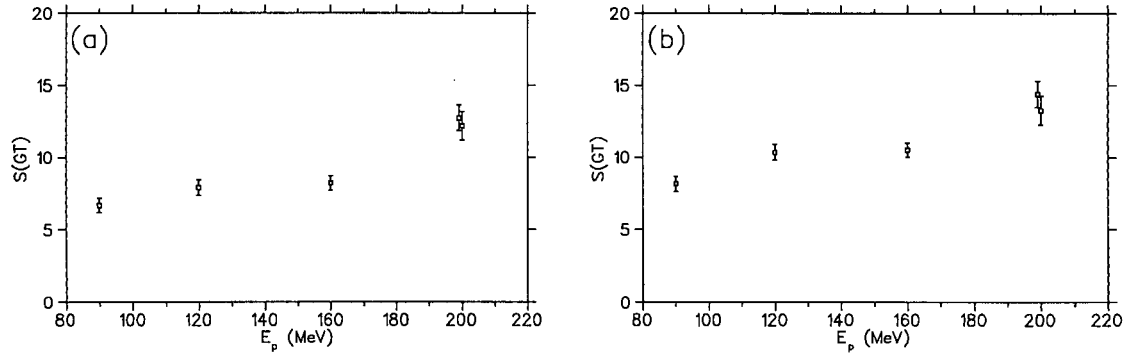

Figure 7.13: Summed GT strength in (a) the discrete structure of ^{59}Co(p,n)^{59}Ni, and (b) the discrete structure plus the background contribution up to E_x = 20 MeV, assuming that the IAS is a pure Fermi transition.

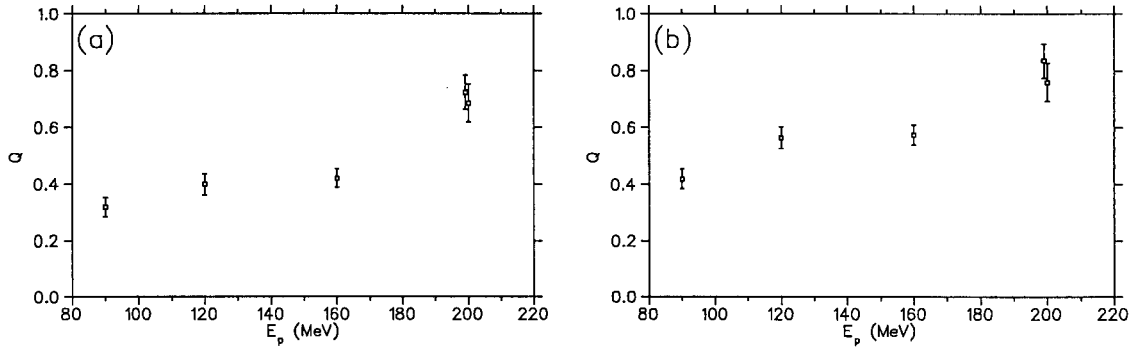

Figure 7.14: The Gamow-Teller sum rule quenching factors $Q = (S(\mathrm{GT})^- - S(\mathrm{GT})^+)/3(N-Z)$ for ^{59}Co(p,n)^{59}Ni if (a) only the strength in the discrete region is considered, and (b) if the strength in the background below the GT resonance is included, assuming that the IAS is a pure Fermi transition.

As another check on the validity of the assumption of zero GT strength in the IAS, the same calculation was done with the arbitrary assumption of $f_{\mathrm{GT}} = 0.50 \pm 0.15$, ie. half the IAS cross section is due to GT strength. The total GT strengths obtained in this manner are plotted in figure 7.15. These strengths are, of course, much larger than in the previous calculation, but the behaviour with beam energy is seen to be extremely insensitive to the exact value of f_{GT} chosen, as was seen in the similar analysis for ^{51}V.

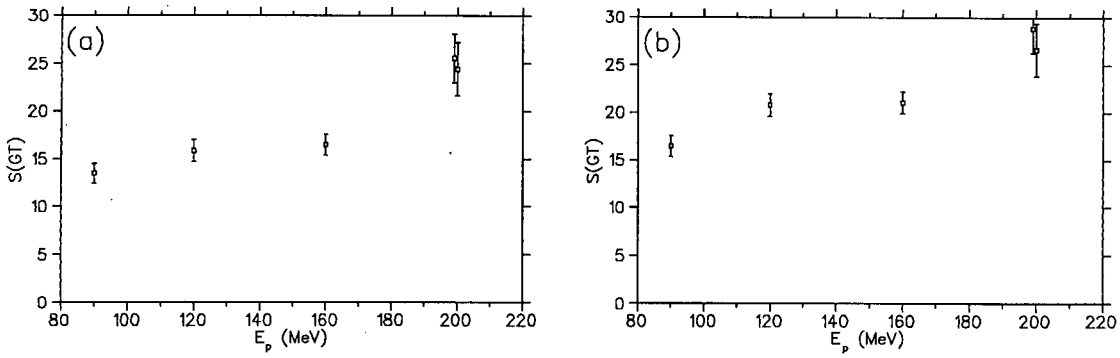

Figure 7.15: Summed GT strength in (a) the discrete structure of ^{59}Co(p,n)^{59}Ni, and (b) the discrete structure plus the background contribution up to $E_x = 20$ MeV, assuming $f_{\mathrm{GT}} = 0.5$.

Chapter 8

Summary and Discussion

Zero degree (p,n) spectra have been acquired for three medium mass targets (^{51}V, ^{54}Fe, and ^{59}Co) at beam energies in the range $90 \leq E_p \leq 200$ MeV. Cross sections are normalised to the known yields for Lithium. A comparison of the spectra from the three reactions at $E_p = 120$ MeV is presented in figure 8.1. In particular, the spectra from ^{51}V$(p,n)^{51}$Cr and ^{59}Co$(p,n)^{59}$Ni are remarkably similar. The IAS transitions occur within 600 keV of each other at ~7 MeV and the GT resonances centered at ~12 MeV in excitation look almost identical. They also have similar groupings of discrete states at excitations below the IAS. Above the IAS the giant resonance is not resolved into separate states although some evidence for structure is seen (ie. the giant resonance bulge is not completely smooth). The total cross sections visible in the spectra are also very similar. This applies to all four measured beam energies. The ^{54}Fe$(p,n)^{54}$Co spectra are slightly different in appearance. The IAS transition is also a strong, clearly identifiable peak, but in this case it is the ground state transition. The GT resonance occurs at an excitation of ~10 MeV, a little lower than in the other two cases. The GT strength is seen to be highly fragmented all the way through the GT resonance up to the continuum region. In fact, nearly thirty states are required in order to get a good fit to the data. The measured cross sections are a little lower than for the other two reactions at each beam energy. In all three targets the isobaric analog state is clearly visible and its cross section is observed to decrease with increasing beam energy as expected from the corresponding term in the effective interaction of Love and Franey [40, 41]. The expected increase in GT cross section with beam energy relative to the Fermi cross section is observed to occur, as is expected from the ratio of corresponding terms in the effective interaction which is plotted in figure 2.1b. The cross sections of the strong discrete transitions are also seen to increase with increasing beam energy in absolute terms for all three targets, as is the total cross section in the discrete structure. This cross section is thought to correspond mostly to GT strength. The continuum background above the GT resonance is observed to increase with beam energy. This is similar for ^{51}V and ^{59}Co and much more pronounced for ^{54}Fe. Estimates have been made of the cross section due to GT strength in the background below the GT resonance. This was done by selecting an excitation energy and assuming that all the cross section below it was due to GT strength. Previous analyses on ^{51}V and ^{54}Fe have shown that some $\Delta L = 0$ strength extends up to excitation energies well beyond 20 MeV and that some $\Delta L > 0$ strength extends almost all of the way down to $E_x = 0$ MeV. The procedure to estimate the background strength assumes that the selection of an appropriate excitation energy will exclude as much $\Delta L = 0$ strength as it includes $\Delta L > 0$ strength. A large uncertainty is introduced with the selection of this energy. In particular the appropriate point may change with beam energy, which has not been considered in this analysis. The background cross sections obtained this way are also seen to increase with beam energy.

Gamow-Teller strengths have been calculated from the extracted cross sections, both for the individual peaks fitted to the spectra and for the total strength in each reaction. The ^{51}V strengths

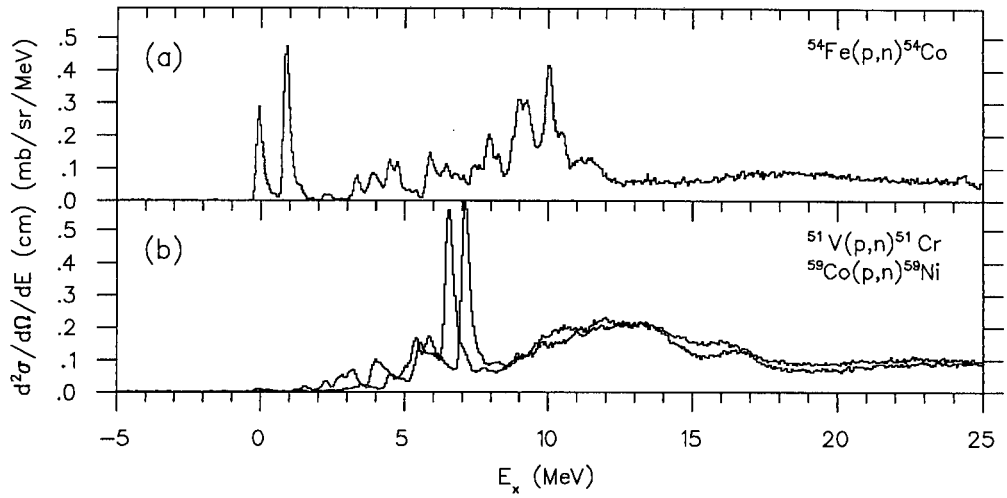

Figure 8.1: Comparison of the 0° spectra from the three reactions at $E_p = 120$ MeV. The two odd mass target spectra are overlayed to highlight their similarity.

were obtained relative to the strength in the ground state transition which is known from beta decay. This is a very weak transition and it appears to be contaminated by non-GT strength, making the extraction of GT strength in the rest of the spectrum unreliable. The ^{54}Fe strengths were obtained relative to the known Fermi strength in the strong IAS transition which is a pure Fermi transition. Since the IAS transition in ^{59}Co contains a mixture of Fermi and GT strength with an unknown ratio, and there is no GT beta decay against which to normalise the strengths, the calculated GT unit cross sections were used to obtain the GT strengths for ^{59}Co. These unit cross sections, however, are subject to large uncertainty which is propagated through to the B(GT). In both the ^{51}V and ^{59}Co reactions the evidence indicated that the amount of GT strength in the IAS transition was small. Based on this, the GT strengths were recalculated in the same manner as for ^{54}Fe under the assumption that the IAS transition was a pure Fermi transition. The GT strengths for ^{51}V increased as expected, while the strengths for ^{59}Co were in good agreement with the previous values. It appears that the assumption of zero, or at least very little, GT strength in the IAS transition is a good one.

The total GT strengths for the three targets, including the strengths in the discrete structure and the background below the GT resonance, are replotted in figure 8.2. The plotted values of $S(\mathrm{GT})^-$ for ^{51}V and ^{59}Co are those obtained under the assumption of zero GT strength in the IAS transition. Also plotted are three of the four previous measurements of $S(\mathrm{GT})^-$ in ^{51}V and ^{54}Fe (excluding the 300 MeV ^{54}Fe point) which are discussed in the chapters corresponding to the particular target.

Equation 2.26, which was used to extract the GT strengths relative to the Fermi strength in the IAS transition, contains three energy dependent variables: $\sigma(0,0)_{\mathrm{GT}}$ which is dependent on E_p, $\sigma(0,0)_{\mathrm{F}}$ which has an inverse dependence on E_p, and $R(E_p,A)^2 \propto E_p^2$. The interplay between these three determines the energy dependence of the derived GT strengths. If the two cross sections are linearly dependent on E_p then the overall dependence of B(GT) of E_p vanishes. However the observed dependence of the cross sections is, in general, not quite linear. In all three cases the total GT strength is seen to increase with E_p, although the strengths of the stronger individual transitions in ^{59}Co(p,n)^{59}Ni do not display such a dependence. The energy dependence is also not as clear in the individual ^{51}V(p,n)^{51}Cr transitions as in the total strength. The energy dependence is most pronounced in the ^{54}Fe data, and especially when the background is included with the total strength in the discrete states.

This energy dependence of the GT strengths is not expected, since they should be a function of

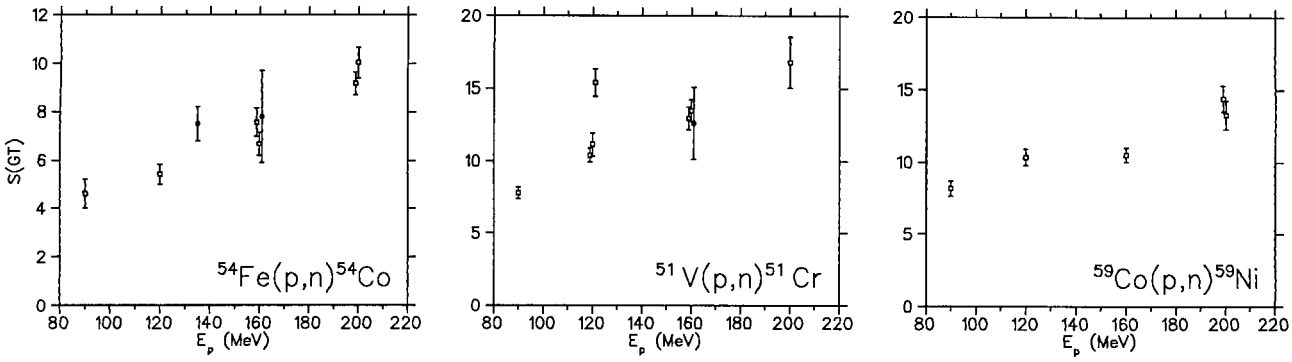

Figure 8.2: Total measured GT strength in the three targets (open squares) compared with previously published points (solid circles – see text for details). The ^{51}V and ^{59}Co values are those obtained under the assumption of a pure Fermi IAS transition.

the nuclear structure and not of the reaction mechanism. The ^{54}Fe(p,n)^{54}Co reaction is where the effect is most pronounced and also the reaction for which the analysis is most unambiguous. The IAS is clearly separated from all other states, so there is no error due to peak deconvolution. It is a strong transition so the statistical error on the extracted yield is small, and any small contamination from non $\Delta L = 0$ strength would have a small effect. In any case, the background clearly goes to zero at this low excitation energy at all but the highest beam energy. It is a pure Fermi transition according to the selection rules. There is probably a large uncertainty in the extracted background cross section, but this is not the case for the discrete states. Not only does the high fragmentation of the GT strength make the fitting of the peaks quite unambiguous, but this reaction has been previously analysed [25] so that the transitions containing GT strength are known. It is thus difficult to imagine a major error in the extraction of the GT strengths in the discrete structure.

At present the effect is not fully understood. However, it is suspected that the main cause of this problem lies with the lower beam energy points. This is enforced by the good agreement with previously published results at higher energies, especially at $E_p = 160$ MeV. The cause could be either due to incorrectly extracted cross sections, or in the derivation of the GT strengths from these cross sections. Two possible causes of the latter can be identified. Firstly, the use of the Impulse Approximation may lead to incorrect strengths at low energies. The 90 MeV points are certainly at the lower limit of the validity of this approximation, and even the 120 MeV points may suffer some effect. Secondly, the use of the parameterization of equation 2.14 for the factor $F(q,\omega)$, in which only central interactions are considered, is also less valid at lower projectile energies. This second approximation may be removed if full DWIA calculations employing non-central interactions were made. Although both of these effects are expected to increase the derived strengths at the lower beam energies, it appears that the cross sections themselves are suspect at the lower beam energies. Recent results suggest that an energy dependence is expected for the cross sections, but that it should be limited to about a 50% increase over the energy range measured here [74]. The data in this work show a 300%–400% increase in cross section from 90 to 200 MeV. It is not known why this dependence appears so pronounced.

The mean value of the total GT strength from the two ^{51}V(p,n)^{51}Cr points at $E_p = 160$ MeV is $S(\mathrm{GT})^- = 13.2 \pm 0.6$ (statistical error only). This is in good agreement with the value of Rapaport *et al.* [17] who obtained $S(\mathrm{GT})^- = 12.6 \pm 2.5$ at the same beam energy. This is still less than the minimum value of $3(N-Z) = 15$ predicted by the GT sum rule. However, this value only includes strength up to $E_x = 20$ MeV and is probably incomplete. The minimum value of 15 is satisfied by the measured strength at $E_p = 200$ MeV. If these values are combined with the measured β^+ strength of $S(\mathrm{GT})^+ = 1.2 \pm 0.1$ [65], also measured at $E_p = 200$ MeV and including strength up to $E_x = 8$ MeV, the sum rule prediction is satisfied at 200 MeV and a large proportion of the predicted

strength is seen at the lower beam energies. Previously published work on ^{54}Fe [24, 25] is more sophisticated than that of ^{51}V [17], employing various model calculations to analyse the background and continuum strength. The GT strength measured at E_p = 160 MeV is about 10% lower than that of reference [24] obtained at the same beam energy, but within the uncertainty of that result. The total β^- strength obtained here can account for the minimum expected value of $3(N-Z) = 6$ at E_p = 160 and 200 MeV. Combined with the measured (n,p) strength of $S(\mathrm{GT})^+ = 3.1 \pm 0.6$ [24] integrated up to E_x = 10 MeV the measured strength can account for the full sum rule prediction at E_p = 200 MeV. This is in agreement with the conclusions of Anderson *et al.* [25] from work at E_p = 135 MeV, and with shell model calculations on ^{54}Fe and ^{56}Fe by Caurier *et al.* [30]. There are no previous (p,n) measurements with which to compare the ^{59}Co results. There is a measured (n,p) strength at E_p = 198 MeV [65] of $S(\mathrm{GT})^+ = 1.9 \pm 0.1$ up to E_x = 8 MeV. The total measured GT strengths cannot quite account for the minimum predicted value of $3(N-Z) = 15$ and combined with the $S(\mathrm{GT})^+$ results in a maximum of 80% of the sum rule prediction. However, if the fraction of GT strength in the IAS transition is 0.2 or greater, instead of zero as assumed in the analysis, then the sum rule prediction could be satisfied at E_p = 200 MeV. Bearing in mind that both the measured $S(\mathrm{GT})^+$ and $S(\mathrm{GT})^-$ are incomplete, and that the assumption of zero f_{GT} results in minimum values of $S(\mathrm{GT})^-$, it appears as if the full GT sum rule prediction could be satisfied in all three reactions (at least at E_p = 200 MeV) by strength in the visible spectrum. Strength in the background and continuum due possibly to configuration mixing may be sufficient to account for all the predicted strength, and the excitation of non-nucleonic degrees of freedom may not be necessary to explain the results.

A recent paper by Aufderheide *et al.* [31] presents shell model calculations of the same three nuclei studied in this work. They predicted that the GT strength in ^{59}Co will probably be larger than that seen in ^{51}V and estimated a value of $S(\mathrm{GT})^- \sim 13.5$. A mean value of $S(\mathrm{GT})^- = 13.9 \pm 0.7$ (statistical error only) for the two points at E_p = 200 MeV is obtained here, in good agreement with that prediction. However, this is lower than the corresponding value for ^{51}V, in disagreement with what they predicted. The calculations, based on a couple of model spaces, do a reasonable job in predicting the GT strength function in ^{51}V and ^{54}Fe. The predictions for ^{59}Co are reproduced in figure 8.3 along with the normalised data from this work. The similarity between the ^{51}V and ^{59}Co spectra was not expected. The calculations do a reasonable job of predicting the general shape, and specifically of predicting the shape of the low excitation energy strength, but centre the GT resonance about 3 MeV higher than it actually is. The relative proportions of the GT components are reproduced quite well.

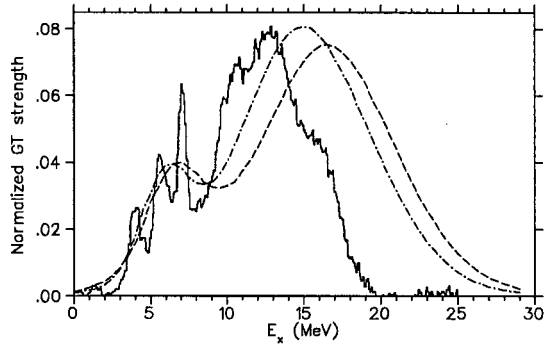

Figure 8.3: Estimated $\Delta L = 0$ strength function for ^{59}Co$(p,n)^{59}$Ni from figure 7.7 compared with the two shell model calculations of Aufderheide *et al.* [31] (the dashed and dot-dashed lines). The strength function has been normalised to the published calculations for comparison.

Apart from the possibly poor approximations used in calculating the GT strengths at low pro-

jectile energies, the primary deficiency in the analysis presented here is the ability to accurately determine the $\Delta L = 0$ components of the spectrum, especially in the background and continuum. Previously published multipole decompositions of ^{51}V$(p,n)^{51}$Cr and ^{54}Fe$(p,n)^{54}$Co data at similar beam energies to those analysed here were used in conjunction with the procedure of Goodman and Bloom [4] to estimate the $\Delta L = 0$ components for ^{51}V and ^{54}Fe. No such published work exists for ^{59}Co. In that case the similarities between ^{59}Co$(p,n)^{59}$Ni and ^{51}V$(p,n)^{51}$Cr were used to justify a similar estimate of the $\Delta L = 0$ strength. It is, therefore, desirable in future work to measure a more extensive angular distribution. These could then be compared with the shapes predicted by DWIA calculations for the various multipole components to decide the relative contributions attributable to each multipole component. An angular distribution up to 20° should be sufficient for the various shapes to be distinguished. The experimental difficulty involved with this is that the visible structure rapidly diminishes as one moves out to higher angles in this target mass range. It is, therefore, difficult to extract the angular distributions of the individual peaks from the acquired spectra. The alternative, and the only possibility for the background and continuum region, is to bin the spectrum into many fixed width bins and to do a multipole decomposition on each bin. Another difficulty encountered in this analysis, and for any analysis on data from odd mass targets, is that the IAS may be reached via a Fermi or a GT transition, and that the IAS peak cross section will thus be a mixture of the two. Unless the amount of this mixing is known it is impossible to use the empirically derived ratio of the two unit cross sections to extract GT strengths. In ^{51}V there is a GT beta decay which allows one to obtain the relative GT strengths of other states. However, the transition of known GT strength is very weak and this introduces large uncertainties into the analysis, as seen in chapter 5. It would, therefore, be desirable for future experiments to employ a polarised proton beam and a neutron polarimeter. Measurement of the transverse spin polarisation transfer coefficient, $D_{\rm NN}$, enables the separation of the spin-flip and non-spin-flip cross sections [9, 71, 72, 73], and thus provides a clearer extraction of the GT strength in the spectrum as well as an independent calculation of the fraction, $f_{\rm GT}$, of GT strength in the IAS.

Although the consistency of the data with previously published results indicated that there were no major flaws in the experiment, there is nevertheless room for improvement. In particular, it would be extremely desirable to have mechanisms to make independent checks on some of the measured quantities. An example would be a means of independently checking the setting of the beam swinger angle. At present this is merely set according to calculated values of the necessary magnetic fields. In several cases analysis of non-zero degree spectra revealed them to be remarkably similar to the corresponding zero degree spectrum, and it is suspected that the swinger angle may not have been at the intended setting. Although it is quite possible that the machine operators merely selected the incorrect angle, it is also possible that the actual angle obtained was less than expected from the calculations. In the cases referred to above, the suspect data had to be discarded and this resulted in some points with zero degree data only. It would obviously be essential to have a complete and accurate angular distribution for further work involving multipole decompositions. Another datum for which no independent check was available was the integrated beam current on target. This comes from a current integrator linked to the Faraday cup just downstream of the target. Since the cross sections are measured relative to the known lithium cross sections, any long term systematic error in quantities such as the accumulated charge should cancel out. However, it would be reassuring to have an independent check of short term variations within a run, possibly by having an inductance coil just upstream of the target to measure the beam current continuously. Lastly, it would be desirable to have some monitor of the beam spot on target. At present the beam is visually aligned between runs by inserting a fluorescent quartz target and using a video camera to look at the bright spot produced by the beam. If the beam wanders slightly during a run, it is currently very hard to notice. This is important because if the beam were to strike anything other than the target, such as the target frame, this would create unwanted background in the data. It is particularly important for targets such as the vanadium target used in this experiment,

which are smaller than the target frame. The vanadium target used here consisted of a rectangular strip of the metal which was slightly narrower than the diameter of the target frame and thus left small gaps between it and the frame on two sides. If some of the beam went through this gap it would have no possibility of a reaction with the target, but would still be included in the charge accumulated in the Faraday cup. This would result in erroneously small cross sections. However, the general stability of the beam and the low probability of it wandering far enough off centre without also striking the target frame, thus creating noticeable background, makes this an unlikely cause of systematic error.

In summary, measured GT strengths have been obtained from (p,n) reactions on targets of ^{51}V, ^{54}Fe, and ^{59}Co, at beam energies from 90 to 200 MeV. An apparent dependence on the incident proton energy of the measured GT strength was observed. This is not expected and at present the cause of this is not completely understood. It is suspected that the extractions of the strengths for the lower beam energy points may be at fault. The cross sections display a greater energy dependence than expected and the approximations made in the derivations of the GT strengths, namely the use of the Impulse Approximation and the consideration of only central interactions, are most valid for the larger beam energies. Indeed, at these beam energies the largest values were obtained for the GT strengths, and these are in good agreement with previously published results. These values exhaust a large fraction of the sum rule prediction. If they are correct, it is possible that the entire GT strength predicted by the sum rule may be in the observed excitation energy range. The relative importance of various mechanisms for shifting the GT strength out of the discrete structure is still the subject of some debate, but the results presented here suggest that those mechanisms responsible for shifting strength to excitation energies beyond those observed here may not be important, at least for *fp*-shell nuclei.

Appendix A

Results of the Spectrum Deconvolutions

In the following tables is listed the information for the individual peaks extracted from the fits to each of the zero degree spectra for the three targets. For each peak the excitation energy E_x assigned to the peak, the centre-of-mass cross section $\sigma(q,\omega)$, the factor $F(q,\omega)$ needed to correct the cross section to zero momentum transfer, and the derived GT strength $B(\mathrm{GT})$, are listed. In each table, the first peak in the list is the IAS. ^{51}V(p,n)^{51}Cr and ^{59}Co(p,n)^{59}Ni have two sets of tables, one for each of the methods used to derive the GT strength. The first method for ^{59}Co(p,n)^{59}Ni, using the GT unit cross section to derive the GT strength, was not applied to the E_p = 90 MeV point and the $B(\mathrm{GT})$ values in that table are all set to zero. It must be remembered that the assignments of peaks within the GT resonance region in ^{51}V and ^{59}Co in particular was rather arbitrary, and the fit was allowed to vary these peak parameters as much as it liked. The tabulated details for these peaks are, therefore, meaningless.

A.1 ^{51}V(p,n)^{51}Cr

^{51}V(p,n)^{51}Cr	$E_p = 90$ MeV	$\theta = 0°$	
E_x	$\sigma(q,\omega)$	$F(q,\omega)$	B(GT)
6.61	5.08 ± 0.19	0.94 ± 0.01	0.00 ± 0.00
0.00	0.10 ± 0.01	1.00 ± 0.00	0.02 ± 0.00
1.36	0.03 ± 0.00	0.99 ± 0.00	0.00 ± 0.00
2.30	0.19 ± 0.01	0.99 ± 0.01	0.03 ± 0.00
2.84	0.28 ± 0.02	0.98 ± 0.01	0.04 ± 0.00
3.24	0.35 ± 0.02	0.98 ± 0.01	0.06 ± 0.00
3.91	0.09 ± 0.01	0.97 ± 0.01	0.01 ± 0.00
4.61	0.29 ± 0.01	0.96 ± 0.01	0.05 ± 0.00
5.11	0.39 ± 0.02	0.95 ± 0.01	0.06 ± 0.00
5.49	0.99 ± 0.04	0.95 ± 0.01	0.16 ± 0.01
5.96	1.04 ± 0.04	0.94 ± 0.01	0.16 ± 0.01
6.44	0.45 ± 0.04	0.92 ± 0.01	0.07 ± 0.01
7.01	1.10 ± 0.05	0.92 ± 0.01	0.17 ± 0.01
7.79	0.55 ± 0.03	0.90 ± 0.01	0.09 ± 0.01
9.07	2.52 ± 0.11	0.87 ± 0.01	0.41 ± 0.03
9.95	0.17 ± 0.02	0.85 ± 0.01	0.03 ± 0.00
11.01	4.77 ± 0.19	0.82 ± 0.02	0.78 ± 0.05
11.96	1.12 ± 0.10	0.79 ± 0.02	0.18 ± 0.02
13.26	5.53 ± 0.26	0.74 ± 0.02	0.92 ± 0.06
14.70	0.56 ± 0.09	0.70 ± 0.02	0.09 ± 0.02
15.48	0.71 ± 0.08	0.67 ± 0.02	0.12 ± 0.02
16.54	2.08 ± 0.09	0.63 ± 0.02	0.35 ± 0.02

^{51}V(p,n)^{51}Cr	$E_p = 120$ MeV	$\theta = 0°$	
E_x	$\sigma(q,\omega)$	$F(q,\omega)$	B(GT)
6.61	3.50 ± 0.12	0.97 ± 0.01	0.00 ± 0.00
0.00	0.09 ± 0.00	1.00 ± 0.00	0.02 ± 0.00
1.36	0.08 ± 0.00	1.00 ± 0.00	0.01 ± 0.00
2.30	0.23 ± 0.01	1.00 ± 0.01	0.04 ± 0.00
2.84	0.37 ± 0.02	0.99 ± 0.01	0.07 ± 0.00
3.24	0.52 ± 0.02	0.99 ± 0.01	0.10 ± 0.01
3.91	0.13 ± 0.01	0.99 ± 0.01	0.02 ± 0.00
4.61	0.44 ± 0.02	0.98 ± 0.01	0.08 ± 0.00
5.11	0.50 ± 0.02	0.98 ± 0.01	0.10 ± 0.01
5.49	1.41 ± 0.05	0.97 ± 0.01	0.27 ± 0.01
5.96	1.41 ± 0.05	0.97 ± 0.01	0.27 ± 0.01
6.44	0.49 ± 0.02	0.96 ± 0.01	0.09 ± 0.01
7.01	0.98 ± 0.06	0.96 ± 0.01	0.19 ± 0.01
7.79	1.82 ± 0.07	0.94 ± 0.01	0.35 ± 0.02
9.07	1.28 ± 0.09	0.92 ± 0.01	0.25 ± 0.02
9.95	0.60 ± 0.08	0.91 ± 0.02	0.12 ± 0.02
11.01	8.38 ± 0.34	0.88 ± 0.02	1.65 ± 0.09
11.96	0.35 ± 0.05	0.87 ± 0.02	0.07 ± 0.01
13.26	7.88 ± 0.43	0.83 ± 0.02	1.56 ± 0.10
14.70	0.41 ± 0.09	0.79 ± 0.02	0.08 ± 0.02
15.48	0.00 ± 0.00	0.78 ± 0.02	0.00 ± 0.00
16.54	4.09 ± 0.16	0.75 ± 0.02	0.82 ± 0.04

^{51}V(p,n)^{51}Cr	$E_p = 120$ MeV	$\theta = 0°$	
E_x	$\sigma(q,\omega)$	$F(q,\omega)$	B(GT)
6.61	3.24 ± 0.20	0.97 ± 0.01	0.00 ± 0.00
0.00	0.07 ± 0.01	1.00 ± 0.00	0.02 ± 0.00
1.36	0.06 ± 0.00	1.00 ± 0.00	0.01 ± 0.00
2.30	0.22 ± 0.02	1.00 ± 0.01	0.05 ± 0.01
2.84	0.37 ± 0.03	0.99 ± 0.01	0.08 ± 0.01
3.24	0.52 ± 0.03	0.99 ± 0.01	0.12 ± 0.01
3.91	0.10 ± 0.01	0.99 ± 0.01	0.02 ± 0.00
4.61	0.38 ± 0.03	0.98 ± 0.01	0.09 ± 0.01
5.11	0.48 ± 0.03	0.98 ± 0.01	0.11 ± 0.01
5.49	1.22 ± 0.08	0.97 ± 0.01	0.28 ± 0.03
5.96	1.34 ± 0.08	0.97 ± 0.01	0.31 ± 0.03
6.44	0.53 ± 0.04	0.96 ± 0.01	0.12 ± 0.01
7.01	1.45 ± 0.10	0.96 ± 0.01	0.34 ± 0.03
7.79	1.40 ± 0.09	0.94 ± 0.01	0.33 ± 0.03
9.07	1.03 ± 0.11	0.93 ± 0.01	0.24 ± 0.03
9.95	3.20 ± 0.24	0.91 ± 0.02	0.76 ± 0.08
11.01	1.61 ± 0.26	0.89 ± 0.02	0.38 ± 0.07
11.96	3.75 ± 0.77	0.87 ± 0.02	0.90 ± 0.19
13.26	7.24 ± 1.29	0.83 ± 0.02	1.74 ± 0.33
14.70	0.48 ± 0.74	0.81 ± 0.02	0.12 ± 0.18
15.48	0.80 ± 0.17	0.79 ± 0.02	0.19 ± 0.04
16.54	2.60 ± 0.20	0.75 ± 0.02	0.63 ± 0.07

^{51}V(p,n)^{51}Cr	$E_p = 120$ MeV	$\theta = 0°$	
E_x	$\sigma(q,\omega)$	$F(q,\omega)$	B(GT)
6.61	2.77 ± 0.13	0.98 ± 0.01	0.00 ± 0.00
0.00	0.08 ± 0.01	1.00 ± 0.00	0.02 ± 0.00
1.36	0.07 ± 0.00	1.00 ± 0.00	0.01 ± 0.00
2.30	0.24 ± 0.01	1.00 ± 0.01	0.05 ± 0.00
2.84	0.42 ± 0.02	1.00 ± 0.01	0.08 ± 0.01
3.24	0.60 ± 0.03	0.99 ± 0.01	0.12 ± 0.01
3.91	0.23 ± 0.01	0.99 ± 0.01	0.05 ± 0.00
4.61	0.43 ± 0.03	0.98 ± 0.01	0.09 ± 0.01
5.11	0.53 ± 0.03	0.98 ± 0.01	0.11 ± 0.01
5.49	1.50 ± 0.07	0.97 ± 0.01	0.30 ± 0.02
5.96	1.60 ± 0.08	0.97 ± 0.01	0.32 ± 0.03
6.44	0.96 ± 0.05	0.96 ± 0.01	0.19 ± 0.02
7.01	2.00 ± 0.10	0.96 ± 0.01	0.40 ± 0.03
7.79	1.86 ± 0.09	0.95 ± 0.01	0.38 ± 0.03
9.07	3.35 ± 0.17	0.92 ± 0.01	0.68 ± 0.05
9.95	2.11 ± 0.13	0.90 ± 0.02	0.43 ± 0.04
11.01	3.66 ± 0.19	0.89 ± 0.02	0.75 ± 0.06
11.96	2.05 ± 0.13	0.87 ± 0.02	0.42 ± 0.04
13.26	9.36 ± 0.45	0.84 ± 0.02	1.94 ± 0.15
14.70	3.68 ± 0.20	0.80 ± 0.02	0.77 ± 0.06
15.48	0.02 ± 0.02	0.78 ± 0.02	0.00 ± 0.00
16.54	4.10 ± 0.19	0.75 ± 0.02	0.87 ± 0.07

^{51}V$(p,n)^{51}$Cr	$E_p = 160$ MeV	$\theta = 0°$	
E_x	$\sigma(q,\omega)$	$F(q,\omega)$	B(GT)
6.61	2.42 ± 0.12	1.00 ± 0.01	0.00 ± 0.00
0.00	0.12 ± 0.01	1.00 ± 0.00	0.02 ± 0.00
1.36	0.08 ± 0.01	1.01 ± 0.00	0.01 ± 0.00
2.30	0.33 ± 0.02	1.01 ± 0.01	0.04 ± 0.00
2.84	0.50 ± 0.03	1.00 ± 0.01	0.07 ± 0.01
3.24	0.63 ± 0.04	1.00 ± 0.01	0.08 ± 0.01
3.91	0.10 ± 0.01	1.00 ± 0.01	0.01 ± 0.00
4.61	0.68 ± 0.04	1.00 ± 0.01	0.09 ± 0.01
5.11	1.10 ± 0.06	1.00 ± 0.01	0.15 ± 0.01
5.49	1.61 ± 0.08	0.99 ± 0.01	0.21 ± 0.02
5.96	1.70 ± 0.09	0.99 ± 0.01	0.23 ± 0.02
6.44	0.79 ± 0.05	0.99 ± 0.01	0.11 ± 0.01
7.01	1.92 ± 0.10	0.98 ± 0.01	0.26 ± 0.02
7.79	0.47 ± 0.05	0.98 ± 0.01	0.06 ± 0.01
9.07	4.47 ± 0.44	0.96 ± 0.01	0.61 ± 0.07
9.95	0.95 ± 0.38	0.95 ± 0.02	0.13 ± 0.05
11.01	6.16 ± 1.38	0.94 ± 0.02	0.84 ± 0.20
11.96	2.47 ± 1.19	0.93 ± 0.02	0.34 ± 0.17
13.26	12.80 ± 1.08	0.91 ± 0.02	1.76 ± 0.18
14.70	1.10 ± 0.28	0.88 ± 0.02	0.15 ± 0.04
15.48	0.00 ± 0.00	0.87 ± 0.02	0.00 ± 0.00
16.54	5.58 ± 0.30	0.85 ± 0.02	0.78 ± 0.06

^{51}V$(p,n)^{51}$Cr	$E_p = 160$ MeV	$\theta = 0°$	
E_x	$\sigma(q,\omega)$	$F(q,\omega)$	B(GT)
6.61	2.37 ± 0.10	1.00 ± 0.01	0.00 ± 0.00
0.00	0.10 ± 0.01	1.00 ± 0.00	0.02 ± 0.00
1.36	0.07 ± 0.00	1.01 ± 0.00	0.01 ± 0.00
2.30	0.34 ± 0.02	1.01 ± 0.01	0.05 ± 0.00
2.84	0.55 ± 0.03	1.00 ± 0.01	0.09 ± 0.01
3.24	0.72 ± 0.03	1.00 ± 0.01	0.11 ± 0.01
3.91	0.13 ± 0.01	1.00 ± 0.01	0.02 ± 0.00
4.61	0.60 ± 0.03	1.00 ± 0.01	0.10 ± 0.01
5.11	0.73 ± 0.04	1.00 ± 0.01	0.12 ± 0.01
5.49	1.98 ± 0.09	0.99 ± 0.01	0.31 ± 0.02
5.96	1.96 ± 0.08	0.99 ± 0.01	0.31 ± 0.02
6.44	1.03 ± 0.05	0.99 ± 0.01	0.16 ± 0.01
7.01	1.87 ± 0.08	0.98 ± 0.01	0.30 ± 0.02
7.79	1.09 ± 0.09	0.98 ± 0.01	0.17 ± 0.02
9.07	3.34 ± 0.17	0.96 ± 0.01	0.54 ± 0.04
9.95	2.85 ± 0.15	0.95 ± 0.02	0.46 ± 0.03
11.01	3.25 ± 0.34	0.94 ± 0.02	0.53 ± 0.06
11.96	5.56 ± 0.44	0.93 ± 0.02	0.90 ± 0.08
13.26	12.23 ± 0.75	0.91 ± 0.02	1.99 ± 0.16
14.70	1.42 ± 0.31	0.88 ± 0.02	0.23 ± 0.05
15.48	0.00 ± 0.00	0.86 ± 0.02	0.00 ± 0.00
16.54	5.83 ± 0.26	0.85 ± 0.02	0.96 ± 0.06

^{51}V$(p,n)^{51}$Cr	$E_p = 200$ MeV	$\theta = 0°$	
E_x	$\sigma(q,\omega)$	$F(q,\omega)$	B(GT)
6.61	0.68 ± 0.05	1.01 ± 0.01	0.00 ± 0.00
0.00	0.09 ± 0.01	1.01 ± 0.00	0.02 ± 0.00
1.36	0.10 ± 0.01	1.01 ± 0.00	0.02 ± 0.00
2.30	0.43 ± 0.02	1.01 ± 0.01	0.07 ± 0.01
2.84	0.61 ± 0.03	1.01 ± 0.01	0.11 ± 0.01
3.24	0.56 ± 0.03	1.01 ± 0.01	0.10 ± 0.01
3.91	0.24 ± 0.02	1.01 ± 0.01	0.04 ± 0.00
4.61	0.74 ± 0.04	1.01 ± 0.01	0.13 ± 0.01
5.11	1.17 ± 0.06	1.01 ± 0.01	0.20 ± 0.02
5.49	1.88 ± 0.09	1.01 ± 0.01	0.33 ± 0.02
5.96	1.94 ± 0.09	1.00 ± 0.01	0.34 ± 0.02
6.44	1.33 ± 0.07	1.00 ± 0.01	0.23 ± 0.02
7.01	2.55 ± 0.13	1.00 ± 0.01	0.45 ± 0.03
7.79	0.15 ± 0.06	1.00 ± 0.01	0.03 ± 0.01
9.07	5.47 ± 0.28	0.99 ± 0.01	0.97 ± 0.07
9.95	2.13 ± 0.16	0.98 ± 0.02	0.38 ± 0.04
11.01	5.19 ± 0.31	0.97 ± 0.02	0.92 ± 0.08
11.96	5.52 ± 0.34	0.96 ± 0.02	0.98 ± 0.08
13.26	11.62 ± 0.56	0.95 ± 0.02	2.08 ± 0.15
14.70	1.01 ± 0.21	0.93 ± 0.02	0.18 ± 0.04
15.48	2.74 ± 0.21	0.92 ± 0.02	0.49 ± 0.05
16.54	5.77 ± 0.26	0.91 ± 0.03	1.04 ± 0.07

^{51}V$(p,n)^{51}$Cr	$E_p = 200$ MeV	$\theta = 0°$	
E_x	$\sigma(q,\omega)$	$F(q,\omega)$	B(GT)
6.61	1.33 ± 0.10	1.01 ± 0.01	0.00 ± 0.00
0.00	0.10 ± 0.01	1.01 ± 0.00	0.02 ± 0.00
1.36	0.10 ± 0.01	1.01 ± 0.00	0.02 ± 0.00
2.30	0.48 ± 0.03	1.01 ± 0.01	0.08 ± 0.01
2.84	0.62 ± 0.04	1.01 ± 0.01	0.10 ± 0.01
3.24	0.52 ± 0.04	1.01 ± 0.01	0.09 ± 0.01
3.91	0.12 ± 0.02	1.01 ± 0.01	0.02 ± 0.00
4.61	0.78 ± 0.05	1.01 ± 0.01	0.13 ± 0.02
5.11	1.36 ± 0.09	1.01 ± 0.01	0.23 ± 0.03
5.49	2.16 ± 0.13	1.01 ± 0.01	0.37 ± 0.04
5.96	1.79 ± 0.11	1.01 ± 0.01	0.30 ± 0.03
6.44	1.09 ± 0.10	1.00 ± 0.01	0.18 ± 0.02
7.01	1.83 ± 0.15	1.00 ± 0.01	0.31 ± 0.04
7.79	0.45 ± 0.11	1.00 ± 0.01	0.08 ± 0.02
9.07	3.22 ± 0.41	0.99 ± 0.01	0.55 ± 0.09
9.95	5.55 ± 0.80	0.98 ± 0.02	0.95 ± 0.16
11.01	3.68 ± 0.69	0.97 ± 0.02	0.63 ± 0.13
11.96	7.82 ± 0.97	0.96 ± 0.02	1.35 ± 0.21
13.26	10.16 ± 0.95	0.95 ± 0.02	1.76 ± 0.23
14.70	3.98 ± 0.48	0.93 ± 0.02	0.69 ± 0.10
15.48	0.03 ± 0.02	0.92 ± 0.02	0.01 ± 0.00
16.54	5.67 ± 0.33	0.91 ± 0.03	0.99 ± 0.11

A.2 ^{51}V(p,n)^{51}Cr assuming $f_{\mathrm{GT}} = 0$

^{51}V(p,n)^{51}Cr	$E_p = 90$ MeV	$\theta = 0°$	
E_x	$\sigma(q,\omega)$	$F(q,\omega)$	B(GT)
6.61	5.08 ± 0.19	0.94 ± 0.01	0.00 ± 0.01
0.00	0.10 ± 0.01	1.00 ± 0.00	0.04 ± 0.00
1.36	0.03 ± 0.00	0.99 ± 0.00	0.01 ± 0.00
2.30	0.19 ± 0.01	0.99 ± 0.01	0.07 ± 0.01
2.84	0.28 ± 0.02	0.98 ± 0.01	0.11 ± 0.01
3.24	0.35 ± 0.02	0.98 ± 0.01	0.13 ± 0.01
3.91	0.09 ± 0.01	0.97 ± 0.01	0.03 ± 0.00
4.61	0.29 ± 0.01	0.96 ± 0.01	0.11 ± 0.01
5.11	0.39 ± 0.02	0.95 ± 0.01	0.15 ± 0.01
5.49	0.99 ± 0.04	0.95 ± 0.01	0.36 ± 0.02
5.96	1.04 ± 0.04	0.94 ± 0.01	0.38 ± 0.02
6.44	0.45 ± 0.04	0.92 ± 0.01	0.16 ± 0.02
7.01	1.10 ± 0.05	0.92 ± 0.01	0.39 ± 0.02
7.79	0.55 ± 0.03	0.90 ± 0.01	0.19 ± 0.01
9.07	2.52 ± 0.11	0.87 ± 0.01	0.85 ± 0.05
9.95	0.17 ± 0.02	0.85 ± 0.01	0.06 ± 0.01
11.01	4.77 ± 0.19	0.82 ± 0.02	1.51 ± 0.09
11.96	1.12 ± 0.10	0.79 ± 0.02	0.34 ± 0.03
13.26	5.53 ± 0.26	0.74 ± 0.02	1.60 ± 0.11
14.70	0.56 ± 0.09	0.70 ± 0.02	0.15 ± 0.03
15.48	0.71 ± 0.08	0.67 ± 0.02	0.19 ± 0.02
16.54	2.08 ± 0.09	0.63 ± 0.02	0.51 ± 0.04

^{51}V(p,n)^{51}Cr	$E_p = 120$ MeV	$\theta = 0°$	
E_x	$\sigma(q,\omega)$	$F(q,\omega)$	B(GT)
6.61	3.50 ± 0.12	0.97 ± 0.01	0.00 ± 0.01
0.00	0.09 ± 0.00	1.00 ± 0.00	0.03 ± 0.00
1.36	0.08 ± 0.00	1.00 ± 0.00	0.02 ± 0.00
2.30	0.23 ± 0.01	1.00 ± 0.01	0.07 ± 0.00
2.84	0.37 ± 0.02	0.99 ± 0.01	0.12 ± 0.01
3.24	0.52 ± 0.02	0.99 ± 0.01	0.16 ± 0.01
3.91	0.13 ± 0.01	0.99 ± 0.01	0.04 ± 0.00
4.61	0.44 ± 0.02	0.98 ± 0.01	0.13 ± 0.01
5.11	0.50 ± 0.02	0.98 ± 0.01	0.15 ± 0.01
5.49	1.41 ± 0.05	0.97 ± 0.01	0.43 ± 0.02
5.96	1.41 ± 0.05	0.97 ± 0.01	0.42 ± 0.02
6.44	0.49 ± 0.02	0.96 ± 0.01	0.15 ± 0.01
7.01	0.98 ± 0.06	0.96 ± 0.01	0.29 ± 0.02
7.79	1.82 ± 0.07	0.94 ± 0.01	0.53 ± 0.03
9.07	1.28 ± 0.09	0.92 ± 0.01	0.37 ± 0.03
9.95	0.60 ± 0.08	0.91 ± 0.02	0.17 ± 0.03
11.01	8.38 ± 0.34	0.88 ± 0.02	2.30 ± 0.14
11.96	0.35 ± 0.05	0.87 ± 0.02	0.10 ± 0.02
13.26	7.88 ± 0.43	0.83 ± 0.02	2.04 ± 0.15
14.70	0.41 ± 0.09	0.79 ± 0.02	0.10 ± 0.02
15.48	0.00 ± 0.00	0.78 ± 0.02	0.00 ± 0.00
16.54	4.09 ± 0.16	0.75 ± 0.02	0.96 ± 0.06

^{51}V(p,n)^{51}Cr	$E_p = 120$ MeV	$\theta = 0°$	
E_x	$\sigma(q,\omega)$	$F(q,\omega)$	B(GT)
6.61	3.24 ± 0.20	0.97 ± 0.01	0.00 ± 0.01
0.00	0.07 ± 0.01	1.00 ± 0.00	0.02 ± 0.00
1.36	0.06 ± 0.00	1.00 ± 0.00	0.02 ± 0.00
2.30	0.22 ± 0.02	1.00 ± 0.01	0.07 ± 0.01
2.84	0.37 ± 0.03	0.99 ± 0.01	0.12 ± 0.01
3.24	0.52 ± 0.03	0.99 ± 0.01	0.17 ± 0.02
3.91	0.10 ± 0.01	0.99 ± 0.01	0.03 ± 0.00
4.61	0.38 ± 0.03	0.98 ± 0.01	0.13 ± 0.01
5.11	0.48 ± 0.03	0.98 ± 0.01	0.15 ± 0.02
5.49	1.22 ± 0.08	0.97 ± 0.01	0.40 ± 0.04
5.96	1.34 ± 0.08	0.97 ± 0.01	0.43 ± 0.04
6.44	0.53 ± 0.04	0.96 ± 0.01	0.17 ± 0.02
7.01	1.45 ± 0.10	0.96 ± 0.01	0.46 ± 0.04
7.79	1.40 ± 0.09	0.94 ± 0.01	0.44 ± 0.04
9.07	1.03 ± 0.11	0.93 ± 0.01	0.32 ± 0.04
9.95	3.20 ± 0.24	0.91 ± 0.02	0.97 ± 0.10
11.01	1.61 ± 0.26	0.89 ± 0.02	0.47 ± 0.08
11.96	3.75 ± 0.77	0.87 ± 0.02	1.09 ± 0.23
13.26	7.24 ± 1.29	0.83 ± 0.02	2.01 ± 0.39
14.70	0.48 ± 0.74	0.81 ± 0.02	0.13 ± 0.20
15.48	0.80 ± 0.17	0.79 ± 0.02	0.21 ± 0.05
16.54	2.60 ± 0.20	0.75 ± 0.02	0.65 ± 0.07

^{51}V(p,n)^{51}Cr	$E_p = 120$ MeV	$\theta = 0°$	
E_x	$\sigma(q,\omega)$	$F(q,\omega)$	B(GT)
6.61	2.77 ± 0.13	0.98 ± 0.01	0.00 ± 0.01
0.00	0.08 ± 0.01	1.00 ± 0.00	0.03 ± 0.00
1.36	0.07 ± 0.00	1.00 ± 0.00	0.03 ± 0.00
2.30	0.24 ± 0.01	1.00 ± 0.01	0.09 ± 0.01
2.84	0.42 ± 0.02	1.00 ± 0.01	0.16 ± 0.01
3.24	0.60 ± 0.03	0.99 ± 0.01	0.23 ± 0.02
3.91	0.23 ± 0.01	0.99 ± 0.01	0.09 ± 0.01
4.61	0.43 ± 0.03	0.98 ± 0.01	0.16 ± 0.01
5.11	0.53 ± 0.03	0.98 ± 0.01	0.20 ± 0.02
5.49	1.50 ± 0.07	0.97 ± 0.01	0.56 ± 0.04
5.96	1.60 ± 0.08	0.97 ± 0.01	0.59 ± 0.04
6.44	0.96 ± 0.05	0.96 ± 0.01	0.36 ± 0.03
7.01	2.00 ± 0.10	0.96 ± 0.01	0.73 ± 0.06
7.79	1.86 ± 0.09	0.95 ± 0.01	0.68 ± 0.05
9.07	3.35 ± 0.17	0.92 ± 0.01	1.18 ± 0.09
9.95	2.11 ± 0.13	0.90 ± 0.02	0.73 ± 0.06
11.01	3.66 ± 0.19	0.89 ± 0.02	1.24 ± 0.10
11.96	2.05 ± 0.13	0.87 ± 0.02	0.68 ± 0.06
13.26	9.36 ± 0.45	0.84 ± 0.02	3.02 ± 0.23
14.70	3.68 ± 0.20	0.80 ± 0.02	1.13 ± 0.09
15.48	0.02 ± 0.02	0.78 ± 0.02	0.01 ± 0.01
16.54	4.10 ± 0.19	0.75 ± 0.02	1.18 ± 0.09

^{51}V$(p,n)^{51}$Cr	$E_p = 160$ MeV	$\theta = 0°$	
E_x	$\sigma(q,\omega)$	$F(q,\omega)$	B(GT)
6.61	2.42 ± 0.12	1.00 ± 0.01	0.00 ± 0.01
0.00	0.12 ± 0.01	1.00 ± 0.00	0.03 ± 0.00
1.36	0.08 ± 0.01	1.01 ± 0.00	0.02 ± 0.00
2.30	0.33 ± 0.02	1.01 ± 0.01	0.08 ± 0.01
2.84	0.50 ± 0.03	1.00 ± 0.01	0.13 ± 0.01
3.24	0.63 ± 0.04	1.00 ± 0.01	0.16 ± 0.01
3.91	0.10 ± 0.01	1.00 ± 0.01	0.02 ± 0.00
4.61	0.68 ± 0.04	1.00 ± 0.01	0.17 ± 0.01
5.11	1.10 ± 0.06	1.00 ± 0.01	0.27 ± 0.02
5.49	1.61 ± 0.08	0.99 ± 0.01	0.40 ± 0.03
5.96	1.70 ± 0.09	0.99 ± 0.01	0.42 ± 0.03
6.44	0.79 ± 0.05	0.99 ± 0.01	0.19 ± 0.02
7.01	1.92 ± 0.10	0.98 ± 0.01	0.47 ± 0.04
7.79	0.47 ± 0.05	0.98 ± 0.01	0.11 ± 0.02
9.07	4.47 ± 0.44	0.96 ± 0.01	1.07 ± 0.12
9.95	0.95 ± 0.38	0.95 ± 0.02	0.23 ± 0.09
11.01	6.16 ± 1.38	0.94 ± 0.02	1.45 ± 0.34
11.96	2.47 ± 1.19	0.93 ± 0.02	0.57 ± 0.28
13.26	12.80 ± 1.08	0.91 ± 0.02	2.90 ± 0.30
14.70	1.10 ± 0.28	0.88 ± 0.02	0.24 ± 0.06
15.48	0.00 ± 0.00	0.87 ± 0.02	0.00 ± 0.00
16.54	5.58 ± 0.30	0.85 ± 0.02	1.18 ± 0.10

^{51}V$(p,n)^{51}$Cr	$E_p = 160$ MeV	$\theta = 0°$	
E_x	$\sigma(q,\omega)$	$F(q,\omega)$	B(GT)
6.61	2.37 ± 0.10	1.00 ± 0.01	0.00 ± 0.00
0.00	0.10 ± 0.01	1.00 ± 0.00	0.03 ± 0.00
1.36	0.07 ± 0.00	1.01 ± 0.00	0.02 ± 0.00
2.30	0.34 ± 0.02	1.01 ± 0.01	0.09 ± 0.01
2.84	0.55 ± 0.03	1.00 ± 0.01	0.14 ± 0.01
3.24	0.72 ± 0.03	1.00 ± 0.01	0.18 ± 0.01
3.91	0.13 ± 0.01	1.00 ± 0.01	0.03 ± 0.00
4.61	0.60 ± 0.03	1.00 ± 0.01	0.15 ± 0.01
5.11	0.73 ± 0.04	1.00 ± 0.01	0.18 ± 0.02
5.49	1.98 ± 0.09	0.99 ± 0.01	0.50 ± 0.03
5.96	1.96 ± 0.08	0.99 ± 0.01	0.49 ± 0.03
6.44	1.03 ± 0.05	0.99 ± 0.01	0.26 ± 0.02
7.01	1.87 ± 0.08	0.98 ± 0.01	0.47 ± 0.03
7.79	1.09 ± 0.09	0.98 ± 0.01	0.27 ± 0.03
9.07	3.34 ± 0.17	0.96 ± 0.01	0.81 ± 0.06
9.95	2.85 ± 0.15	0.95 ± 0.02	0.69 ± 0.05
11.01	3.25 ± 0.34	0.94 ± 0.02	0.78 ± 0.09
11.96	5.56 ± 0.44	0.93 ± 0.02	1.31 ± 0.13
13.26	12.23 ± 0.75	0.91 ± 0.02	2.80 ± 0.23
14.70	1.42 ± 0.31	0.88 ± 0.02	0.32 ± 0.07
15.48	0.00 ± 0.00	0.86 ± 0.02	0.00 ± 0.00
16.54	5.83 ± 0.26	0.85 ± 0.02	1.25 ± 0.09

^{51}V$(p,n)^{51}$Cr	$E_p = 200$ MeV	$\theta = 0°$	
E_x	$\sigma(q,\omega)$	$F(q,\omega)$	B(GT)
6.61	1.33 ± 0.10	1.01 ± 0.01	0.00 ± 0.00
0.00	0.10 ± 0.01	1.01 ± 0.00	0.03 ± 0.00
1.36	0.10 ± 0.01	1.01 ± 0.00	0.03 ± 0.00
2.30	0.48 ± 0.03	1.01 ± 0.01	0.14 ± 0.02
2.84	0.62 ± 0.04	1.01 ± 0.01	0.17 ± 0.02
3.24	0.52 ± 0.04	1.01 ± 0.01	0.15 ± 0.02
3.91	0.12 ± 0.02	1.01 ± 0.01	0.04 ± 0.01
4.61	0.78 ± 0.05	1.01 ± 0.01	0.22 ± 0.03
5.11	1.36 ± 0.09	1.01 ± 0.01	0.38 ± 0.05
5.49	2.16 ± 0.13	1.01 ± 0.01	0.61 ± 0.08
5.96	1.79 ± 0.11	1.01 ± 0.01	0.51 ± 0.06
6.44	1.09 ± 0.10	1.00 ± 0.01	0.31 ± 0.04
7.01	1.83 ± 0.15	1.00 ± 0.01	0.52 ± 0.07
7.79	0.45 ± 0.11	1.00 ± 0.01	0.13 ± 0.04
9.07	3.22 ± 0.41	0.99 ± 0.01	0.90 ± 0.15
9.95	5.55 ± 0.80	0.98 ± 0.02	1.53 ± 0.28
11.01	3.68 ± 0.69	0.97 ± 0.02	1.01 ± 0.22
11.96	7.82 ± 0.97	0.96 ± 0.02	2.12 ± 0.35
13.26	10.16 ± 0.95	0.95 ± 0.02	2.71 ± 0.40
14.70	3.98 ± 0.48	0.93 ± 0.02	1.04 ± 0.17
15.48	0.03 ± 0.02	0.92 ± 0.02	0.01 ± 0.01
16.54	5.67 ± 0.33	0.91 ± 0.03	1.45 ± 0.18

A.3 ^{54}Fe(p,n)^{54}Co

^{54}Fe(p,n)^{54}Co	$E_p = 90$ MeV	$\theta = 0°$	
E_x	$\sigma(q,\omega)$	$F(q,\omega)$	B(GT)
0.00	1.85 ± 0.18	0.93 ± 0.01	0.00 ± 0.00
0.94	1.42 ± 0.14	0.89 ± 0.01	0.54 ± 0.08
1.55	0.07 ± 0.01	0.88 ± 0.01	0.03 ± 0.01
2.31	0.12 ± 0.01	0.85 ± 0.02	0.05 ± 0.01
2.79	0.24 ± 0.02	0.83 ± 0.02	0.09 ± 0.01
3.40	0.37 ± 0.03	0.82 ± 0.02	0.13 ± 0.02
3.99	0.40 ± 0.03	0.80 ± 0.02	0.14 ± 0.02
4.55	0.42 ± 0.04	0.79 ± 0.02	0.14 ± 0.02
4.80	0.30 ± 0.03	0.78 ± 0.02	0.10 ± 0.01
5.31	0.37 ± 0.03	0.77 ± 0.02	0.12 ± 0.02
5.97	0.64 ± 0.04	0.74 ± 0.02	0.20 ± 0.03
6.51	0.44 ± 0.05	0.73 ± 0.02	0.14 ± 0.02
6.99	0.49 ± 0.06	0.71 ± 0.02	0.15 ± 0.02
7.51	0.59 ± 0.10	0.69 ± 0.02	0.17 ± 0.03
8.00	0.69 ± 0.11	0.68 ± 0.02	0.20 ± 0.04
8.39	0.67 ± 0.06	0.66 ± 0.02	0.19 ± 0.03
8.96	1.35 ± 0.14	0.64 ± 0.02	0.37 ± 0.05
9.32	0.77 ± 0.15	0.62 ± 0.02	0.21 ± 0.05
9.69	0.41 ± 0.08	0.61 ± 0.02	0.11 ± 0.02
10.06	1.47 ± 0.15	0.60 ± 0.02	0.38 ± 0.06
10.52	0.87 ± 0.12	0.59 ± 0.02	0.22 ± 0.04
10.96	0.45 ± 0.27	0.57 ± 0.02	0.11 ± 0.07
11.30	0.68 ± 0.09	0.56 ± 0.02	0.16 ± 0.03
11.65	0.56 ± 0.06	0.54 ± 0.02	0.13 ± 0.02
12.03	0.56 ± 0.05	0.53 ± 0.02	0.13 ± 0.02
12.44	0.26 ± 0.05	0.51 ± 0.02	0.06 ± 0.01
12.93	0.47 ± 0.04	0.50 ± 0.02	0.10 ± 0.01
13.40	0.50 ± 0.05	0.48 ± 0.02	0.10 ± 0.02
13.81	0.61 ± 0.05	0.46 ± 0.02	0.12 ± 0.02

^{54}Fe(p,n)^{54}Co	$E_p = 120$ MeV	$\theta = 0°$	
E_x	$\sigma(q,\omega)$	$F(q,\omega)$	B(GT)
0.00	1.65 ± 0.08	0.97 ± 0.01	0.00 ± 0.00
0.94	2.89 ± 0.14	0.94 ± 0.01	0.71 ± 0.05
1.55	0.14 ± 0.01	0.93 ± 0.01	0.03 ± 0.00
2.31	0.13 ± 0.01	0.91 ± 0.02	0.03 ± 0.00
2.79	0.00 ± 0.00	0.90 ± 0.02	0.00 ± 0.00
3.40	0.50 ± 0.02	0.89 ± 0.02	0.12 ± 0.01
3.99	0.74 ± 0.04	0.88 ± 0.02	0.17 ± 0.01
4.55	0.76 ± 0.04	0.87 ± 0.02	0.17 ± 0.01
4.80	0.55 ± 0.03	0.86 ± 0.02	0.12 ± 0.01
5.31	0.16 ± 0.01	0.85 ± 0.02	0.04 ± 0.00
5.97	1.16 ± 0.06	0.83 ± 0.02	0.25 ± 0.02
6.51	0.81 ± 0.04	0.82 ± 0.02	0.17 ± 0.01
6.99	0.57 ± 0.03	0.81 ± 0.02	0.12 ± 0.01
7.51	0.87 ± 0.04	0.80 ± 0.02	0.18 ± 0.01
8.00	1.48 ± 0.07	0.78 ± 0.02	0.30 ± 0.02
8.39	0.71 ± 0.03	0.77 ± 0.02	0.14 ± 0.01
8.96	2.10 ± 0.10	0.76 ± 0.02	0.42 ± 0.03
9.32	2.13 ± 0.10	0.75 ± 0.02	0.42 ± 0.03
9.69	0.84 ± 0.04	0.74 ± 0.02	0.16 ± 0.01
10.06	3.19 ± 0.15	0.73 ± 0.02	0.61 ± 0.05
10.52	1.32 ± 0.06	0.71 ± 0.03	0.25 ± 0.02
10.96	0.66 ± 0.03	0.70 ± 0.03	0.12 ± 0.01
11.30	0.60 ± 0.03	0.69 ± 0.03	0.11 ± 0.01
11.65	0.65 ± 0.03	0.68 ± 0.03	0.12 ± 0.01
12.03	0.35 ± 0.02	0.67 ± 0.03	0.06 ± 0.01
12.44	0.24 ± 0.01	0.66 ± 0.03	0.04 ± 0.00
12.93	0.24 ± 0.01	0.64 ± 0.03	0.04 ± 0.00
13.40	0.25 ± 0.01	0.63 ± 0.03	0.04 ± 0.00
13.81	0.14 ± 0.01	0.61 ± 0.03	0.02 ± 0.00

^{54}Fe$(p,n)^{54}$Co	$E_p = 160$ MeV	$\theta = 0°$	
E_x	$\sigma(q,\omega)$	$F(q,\omega)$	B(GT)
0.00	1.27 ± 0.08	1.00 ± 0.01	0.00 ± 0.00
0.94	4.29 ± 0.25	0.97 ± 0.01	0.80 ± 0.07
1.55	0.22 ± 0.02	0.97 ± 0.02	0.04 ± 0.00
2.31	0.14 ± 0.01	0.96 ± 0.02	0.03 ± 0.00
2.79	0.25 ± 0.02	0.96 ± 0.02	0.05 ± 0.00
3.40	0.77 ± 0.05	0.95 ± 0.02	0.14 ± 0.01
3.99	1.15 ± 0.07	0.94 ± 0.02	0.21 ± 0.02
4.55	1.16 ± 0.09	0.93 ± 0.02	0.21 ± 0.02
4.80	0.79 ± 0.08	0.93 ± 0.02	0.14 ± 0.02
5.31	0.23 ± 0.02	0.92 ± 0.02	0.04 ± 0.00
5.97	1.57 ± 0.10	0.91 ± 0.02	0.27 ± 0.02
6.51	0.96 ± 0.06	0.90 ± 0.02	0.16 ± 0.02
6.99	0.73 ± 0.05	0.89 ± 0.02	0.13 ± 0.01
7.51	1.17 ± 0.07	0.88 ± 0.02	0.20 ± 0.02
8.00	2.21 ± 0.13	0.87 ± 0.02	0.37 ± 0.03
8.39	0.85 ± 0.06	0.86 ± 0.03	0.14 ± 0.01
8.96	2.99 ± 0.19	0.85 ± 0.03	0.49 ± 0.05
9.32	3.03 ± 0.19	0.85 ± 0.03	0.49 ± 0.05
9.69	1.16 ± 0.09	0.84 ± 0.03	0.19 ± 0.02
10.06	4.79 ± 0.29	0.83 ± 0.03	0.76 ± 0.07
10.52	2.04 ± 0.12	0.82 ± 0.03	0.32 ± 0.03
10.96	1.08 ± 0.07	0.81 ± 0.03	0.17 ± 0.02
11.30	0.89 ± 0.07	0.80 ± 0.03	0.14 ± 0.01
11.65	0.83 ± 0.07	0.79 ± 0.03	0.13 ± 0.01
12.03	0.34 ± 0.03	0.78 ± 0.03	0.05 ± 0.01
12.44	0.24 ± 0.03	0.78 ± 0.03	0.04 ± 0.01
12.93	0.25 ± 0.03	0.77 ± 0.03	0.04 ± 0.01
13.40	0.31 ± 0.03	0.75 ± 0.03	0.05 ± 0.01
13.81	0.16 ± 0.02	0.74 ± 0.03	0.02 ± 0.00

^{54}Fe$(p,n)^{54}$Co	$E_p = 160$ MeV	$\theta = 0°$	
E_x	$\sigma(q,\omega)$	$F(q,\omega)$	B(GT)
0.00	1.17 ± 0.06	1.00 ± 0.01	0.00 ± 0.00
0.94	3.99 ± 0.19	0.97 ± 0.01	0.80 ± 0.06
1.55	0.11 ± 0.01	0.97 ± 0.02	0.02 ± 0.00
2.31	0.19 ± 0.01	0.96 ± 0.02	0.04 ± 0.00
2.79	0.00 ± 0.00	0.95 ± 0.02	0.00 ± 0.00
3.40	0.63 ± 0.03	0.95 ± 0.02	0.12 ± 0.01
3.99	0.98 ± 0.05	0.94 ± 0.02	0.19 ± 0.01
4.55	1.03 ± 0.10	0.93 ± 0.02	0.20 ± 0.02
4.80	0.76 ± 0.10	0.93 ± 0.02	0.14 ± 0.02
5.31	0.21 ± 0.02	0.92 ± 0.02	0.04 ± 0.00
5.97	1.48 ± 0.07	0.91 ± 0.02	0.28 ± 0.02
6.51	0.95 ± 0.05	0.90 ± 0.02	0.17 ± 0.01
6.99	0.70 ± 0.04	0.89 ± 0.02	0.13 ± 0.01
7.51	1.09 ± 0.06	0.88 ± 0.02	0.20 ± 0.02
8.00	2.14 ± 0.11	0.87 ± 0.02	0.38 ± 0.03
8.39	1.03 ± 0.06	0.86 ± 0.03	0.18 ± 0.02
8.96	2.67 ± 0.15	0.85 ± 0.03	0.47 ± 0.04
9.32	3.05 ± 0.15	0.85 ± 0.03	0.53 ± 0.04
9.69	1.39 ± 0.09	0.84 ± 0.03	0.24 ± 0.02
10.06	4.29 ± 0.21	0.83 ± 0.03	0.73 ± 0.06
10.52	1.87 ± 0.10	0.82 ± 0.03	0.32 ± 0.03
10.96	0.80 ± 0.09	0.81 ± 0.03	0.13 ± 0.02
11.30	0.83 ± 0.09	0.81 ± 0.03	0.14 ± 0.02
11.65	0.80 ± 0.09	0.80 ± 0.03	0.13 ± 0.02
12.03	0.57 ± 0.08	0.79 ± 0.03	0.09 ± 0.01
12.44	0.34 ± 0.03	0.78 ± 0.03	0.06 ± 0.01
12.93	0.20 ± 0.02	0.77 ± 0.03	0.03 ± 0.00
13.40	0.22 ± 0.02	0.76 ± 0.03	0.04 ± 0.00
13.81	0.21 ± 0.02	0.75 ± 0.03	0.03 ± 0.00

^{54}Fe$(p,n)^{54}$Co		$E_p = 200$ MeV	$\theta = 0°$
E_x	$\sigma(q,\omega)$	$F(q,\omega)$	B(GT)
0.00	0.88 ± 0.03	1.02 ± 0.01	0.00 ± 0.00
0.94	4.70 ± 0.16	1.00 ± 0.01	0.81 ± 0.05
1.55	0.31 ± 0.03	0.99 ± 0.02	0.05 ± 0.01
2.31	0.51 ± 0.03	0.99 ± 0.02	0.09 ± 0.01
2.79	0.01 ± 0.03	0.98 ± 0.02	0.00 ± 0.01
3.40	0.94 ± 0.05	0.98 ± 0.02	0.16 ± 0.01
3.99	1.29 ± 0.07	0.97 ± 0.02	0.22 ± 0.02
4.55	1.18 ± 0.11	0.97 ± 0.02	0.20 ± 0.02
4.80	1.01 ± 0.11	0.97 ± 0.02	0.17 ± 0.02
5.31	0.07 ± 0.05	0.96 ± 0.02	0.01 ± 0.01
5.97	1.61 ± 0.07	0.95 ± 0.02	0.27 ± 0.02
6.51	1.05 ± 0.07	0.95 ± 0.02	0.17 ± 0.01
6.99	0.70 ± 0.07	0.94 ± 0.02	0.11 ± 0.01
7.51	1.00 ± 0.09	0.94 ± 0.02	0.16 ± 0.02
8.00	2.37 ± 0.14	0.93 ± 0.03	0.38 ± 0.03
8.39	1.04 ± 0.16	0.92 ± 0.03	0.17 ± 0.03
8.96	3.16 ± 0.30	0.92 ± 0.03	0.50 ± 0.05
9.32	4.18 ± 0.63	0.91 ± 0.03	0.66 ± 0.10
9.69	0.08 ± 0.64	0.91 ± 0.03	0.01 ± 0.10
10.06	5.75 ± 0.30	0.90 ± 0.03	0.89 ± 0.07
10.52	2.27 ± 0.36	0.89 ± 0.03	0.35 ± 0.06
10.96	0.84 ± 0.24	0.89 ± 0.03	0.13 ± 0.04
11.30	1.10 ± 0.23	0.88 ± 0.03	0.17 ± 0.04
11.65	0.95 ± 0.19	0.87 ± 0.03	0.14 ± 0.03
12.03	0.70 ± 0.14	0.87 ± 0.03	0.11 ± 0.02
12.44	0.18 ± 0.10	0.86 ± 0.03	0.03 ± 0.02
12.93	0.45 ± 0.08	0.85 ± 0.03	0.07 ± 0.01
13.40	0.23 ± 0.07	0.84 ± 0.03	0.03 ± 0.01
13.81	0.58 ± 0.06	0.84 ± 0.03	0.08 ± 0.01

^{54}Fe$(p,n)^{54}$Co		$E_p = 200$ MeV	$\theta = 0°$
E_x	$\sigma(q,\omega)$	$F(q,\omega)$	B(GT)
0.00	0.79 ± 0.04	1.02 ± 0.01	0.00 ± 0.00
0.94	4.41 ± 0.19	1.00 ± 0.01	0.83 ± 0.06
1.55	0.70 ± 0.04	1.00 ± 0.02	0.13 ± 0.01
2.31	0.39 ± 0.03	0.99 ± 0.02	0.07 ± 0.01
2.79	0.17 ± 0.03	0.99 ± 0.02	0.03 ± 0.01
3.40	0.83 ± 0.05	0.98 ± 0.02	0.15 ± 0.01
3.99	1.24 ± 0.07	0.98 ± 0.02	0.23 ± 0.02
4.55	1.05 ± 0.10	0.97 ± 0.02	0.19 ± 0.02
4.80	1.10 ± 0.11	0.97 ± 0.02	0.20 ± 0.02
5.31	0.32 ± 0.06	0.96 ± 0.02	0.06 ± 0.01
5.97	1.49 ± 0.08	0.96 ± 0.02	0.27 ± 0.02
6.51	1.17 ± 0.08	0.95 ± 0.02	0.21 ± 0.02
6.99	0.78 ± 0.07	0.94 ± 0.02	0.14 ± 0.02
7.51	0.92 ± 0.08	0.94 ± 0.03	0.16 ± 0.02
8.00	1.94 ± 0.12	0.93 ± 0.03	0.34 ± 0.03
8.39	1.36 ± 0.12	0.93 ± 0.03	0.24 ± 0.03
8.96	2.31 ± 0.14	0.92 ± 0.03	0.40 ± 0.04
9.32	4.50 ± 0.25	0.91 ± 0.03	0.77 ± 0.06
9.69	0.00 ± 0.01	0.91 ± 0.03	0.00 ± 0.00
10.06	5.00 ± 0.24	0.90 ± 0.03	0.85 ± 0.07
10.52	3.35 ± 0.22	0.90 ± 0.03	0.56 ± 0.05
10.96	1.30 ± 0.15	0.89 ± 0.03	0.22 ± 0.03
11.30	1.09 ± 0.16	0.88 ± 0.03	0.18 ± 0.03
11.65	1.05 ± 0.14	0.88 ± 0.03	0.17 ± 0.03
12.03	0.95 ± 0.11	0.87 ± 0.03	0.16 ± 0.02
12.44	0.42 ± 0.08	0.86 ± 0.03	0.07 ± 0.01
12.93	0.54 ± 0.07	0.85 ± 0.03	0.09 ± 0.01
13.40	0.25 ± 0.07	0.85 ± 0.03	0.04 ± 0.01
13.81	0.52 ± 0.07	0.84 ± 0.03	0.08 ± 0.01

A.4 ^{59}Co(p,n)^{59}Ni

^{59}Co(p,n)^{59}Ni	$E_p = 90$ MeV	$\theta = 0°$	
E_x	$\sigma(q,\omega)$	$F(q,\omega)$	B(GT)
7.18	4.49 ± 0.23	0.94 ± 0.01	0.00 ± 0.00
0.34	0.04 ± 0.00	1.00 ± 0.00	0.00 ± 0.00
1.60	0.07 ± 0.01	0.99 ± 0.01	0.00 ± 0.00
2.58	0.02 ± 0.00	0.99 ± 0.01	0.00 ± 0.00
3.17	0.04 ± 0.01	0.98 ± 0.01	0.00 ± 0.00
3.52	0.12 ± 0.01	0.98 ± 0.01	0.00 ± 0.00
4.07	0.47 ± 0.03	0.97 ± 0.01	0.00 ± 0.00
4.41	0.22 ± 0.02	0.96 ± 0.01	0.00 ± 0.00
4.71	0.17 ± 0.01	0.96 ± 0.01	0.00 ± 0.00
5.08	0.10 ± 0.01	0.95 ± 0.01	0.00 ± 0.00
5.58	0.77 ± 0.04	0.95 ± 0.01	0.00 ± 0.00
5.96	0.47 ± 0.03	0.94 ± 0.01	0.00 ± 0.00
6.30	0.47 ± 0.03	0.93 ± 0.01	0.00 ± 0.00
6.69	0.29 ± 0.02	0.92 ± 0.01	0.00 ± 0.00
7.07	0.35 ± 0.04	0.91 ± 0.01	0.00 ± 0.00
7.64	0.21 ± 0.03	0.91 ± 0.01	0.00 ± 0.00
8.20	0.83 ± 0.06	0.89 ± 0.01	0.00 ± 0.00
9.37	2.35 ± 0.24	0.86 ± 0.02	0.00 ± 0.00
10.56	3.02 ± 0.35	0.82 ± 0.02	0.00 ± 0.00
11.81	0.98 ± 0.19	0.79 ± 0.02	0.00 ± 0.00
12.63	0.79 ± 0.10	0.77 ± 0.02	0.00 ± 0.00
13.49	2.52 ± 0.21	0.74 ± 0.02	0.00 ± 0.00
14.58	2.82 ± 0.21	0.69 ± 0.02	0.00 ± 0.00
15.82	0.57 ± 0.13	0.65 ± 0.02	0.00 ± 0.00
16.74	0.53 ± 0.16	0.62 ± 0.02	0.00 ± 0.00
17.75	0.67 ± 0.12	0.59 ± 0.02	0.00 ± 0.00

^{59}Co(p,n)^{59}Ni	$E_p = 120$ MeV	$\theta = 0°$	
E_x	$\sigma(q,\omega)$	$F(q,\omega)$	B(GT)
7.18	3.67 ± 0.17	0.98 ± 0.01	0.00 ± 0.00
0.34	0.05 ± 0.00	1.00 ± 0.00	0.01 ± 0.00
1.60	0.13 ± 0.01	1.00 ± 0.01	0.03 ± 0.01
2.58	0.03 ± 0.00	1.00 ± 0.01	0.01 ± 0.00
3.17	0.07 ± 0.01	1.00 ± 0.01	0.02 ± 0.01
3.52	0.15 ± 0.01	0.99 ± 0.01	0.04 ± 0.01
4.07	0.74 ± 0.04	0.99 ± 0.01	0.18 ± 0.05
4.41	0.48 ± 0.03	0.99 ± 0.01	0.12 ± 0.04
4.71	0.23 ± 0.02	0.98 ± 0.01	0.06 ± 0.02
5.08	0.22 ± 0.01	0.98 ± 0.01	0.05 ± 0.02
5.58	1.02 ± 0.05	0.98 ± 0.01	0.26 ± 0.08
5.96	0.72 ± 0.04	0.97 ± 0.01	0.18 ± 0.05
6.30	0.77 ± 0.04	0.97 ± 0.01	0.19 ± 0.06
6.69	0.52 ± 0.03	0.96 ± 0.01	0.13 ± 0.04
7.07	0.28 ± 0.03	0.96 ± 0.01	0.07 ± 0.02
7.64	0.68 ± 0.07	0.95 ± 0.01	0.17 ± 0.05
8.20	1.12 ± 0.10	0.94 ± 0.02	0.29 ± 0.09
9.37	5.06 ± 0.28	0.92 ± 0.02	1.35 ± 0.40
10.56	3.82 ± 0.28	0.89 ± 0.02	1.04 ± 0.32
11.81	0.43 ± 0.12	0.87 ± 0.02	0.12 ± 0.05
12.63	4.40 ± 0.35	0.86 ± 0.02	1.25 ± 0.38
13.49	2.41 ± 0.48	0.83 ± 0.02	0.70 ± 0.25
14.58	3.90 ± 0.66	0.80 ± 0.02	1.18 ± 0.40
15.82	2.16 ± 0.47	0.76 ± 0.03	0.69 ± 0.25
16.74	0.30 ± 0.17	0.74 ± 0.03	0.10 ± 0.06
17.75	0.86 ± 0.06	0.72 ± 0.03	0.29 ± 0.09

^{59}Co(p,n)^{59}Ni	$E_p = 160$ MeV	$\theta = 0°$	
E_x	$\sigma(q,\omega)$	$F(q,\omega)$	B(GT)
7.18	2.96 ± 0.11	1.00 ± 0.01	0.00 ± 0.00
0.34	0.06 ± 0.00	1.01 ± 0.00	0.01 ± 0.00
1.60	0.19 ± 0.01	1.01 ± 0.01	0.04 ± 0.01
2.58	0.07 ± 0.00	1.01 ± 0.01	0.01 ± 0.00
3.17	0.09 ± 0.01	1.01 ± 0.01	0.02 ± 0.01
3.52	0.13 ± 0.01	1.01 ± 0.01	0.03 ± 0.01
4.07	1.16 ± 0.05	1.01 ± 0.01	0.23 ± 0.07
4.41	0.48 ± 0.04	1.01 ± 0.01	0.09 ± 0.03
4.71	0.17 ± 0.07	1.00 ± 0.01	0.03 ± 0.02
5.08	0.37 ± 0.02	1.00 ± 0.01	0.07 ± 0.02
5.58	1.70 ± 0.07	1.00 ± 0.01	0.33 ± 0.10
5.96	1.13 ± 0.05	1.00 ± 0.01	0.22 ± 0.07
6.30	0.95 ± 0.04	1.00 ± 0.01	0.19 ± 0.06
6.69	0.58 ± 0.03	0.99 ± 0.01	0.12 ± 0.04
7.07	0.04 ± 0.03	0.99 ± 0.01	0.01 ± 0.01
7.64	0.17 ± 0.02	0.99 ± 0.01	0.03 ± 0.01
8.20	1.98 ± 0.08	0.98 ± 0.02	0.40 ± 0.12
9.37	1.29 ± 0.22	0.97 ± 0.02	0.26 ± 0.09
10.56	11.60 ± 0.65	0.95 ± 0.02	2.38 ± 0.72
11.81	0.91 ± 0.09	0.94 ± 0.02	0.19 ± 0.06
12.63	9.02 ± 0.59	0.92 ± 0.02	1.92 ± 0.58
13.49	0.32 ± 0.10	0.91 ± 0.02	0.07 ± 0.03
14.58	6.03 ± 0.35	0.89 ± 0.03	1.33 ± 0.40
15.82	1.37 ± 0.12	0.87 ± 0.03	0.31 ± 0.10
16.74	2.65 ± 0.11	0.85 ± 0.03	0.61 ± 0.18
17.75	1.06 ± 0.05	0.83 ± 0.03	0.25 ± 0.08

^{59}Co(p,n)^{59}Ni	$E_p = 200$ MeV	$\theta = 0°$	
E_x	$\sigma(q,\omega)$	$F(q,\omega)$	B(GT)
7.18	1.87 ± 0.08	1.02 ± 0.01	0.00 ± 0.00
0.34	0.07 ± 0.00	1.01 ± 0.00	0.01 ± 0.00
1.60	0.18 ± 0.01	1.01 ± 0.01	0.04 ± 0.01
2.58	0.08 ± 0.01	1.02 ± 0.01	0.02 ± 0.01
3.17	0.09 ± 0.01	1.02 ± 0.01	0.02 ± 0.01
3.52	0.35 ± 0.02	1.02 ± 0.01	0.07 ± 0.02
4.07	1.08 ± 0.05	1.02 ± 0.01	0.21 ± 0.07
4.41	0.47 ± 0.04	1.02 ± 0.01	0.09 ± 0.03
4.71	0.34 ± 0.03	1.02 ± 0.01	0.07 ± 0.02
5.08	0.57 ± 0.03	1.02 ± 0.01	0.11 ± 0.03
5.58	1.61 ± 0.06	1.01 ± 0.01	0.32 ± 0.10
5.96	0.94 ± 0.05	1.01 ± 0.01	0.18 ± 0.06
6.30	0.95 ± 0.05	1.01 ± 0.01	0.19 ± 0.06
6.69	1.00 ± 0.06	1.01 ± 0.01	0.20 ± 0.06
7.07	0.89 ± 0.07	1.01 ± 0.01	0.18 ± 0.06
7.64	0.40 ± 0.09	1.01 ± 0.02	0.08 ± 0.03
8.20	3.22 ± 0.12	1.00 ± 0.02	0.64 ± 0.19
9.37	0.71 ± 0.04	1.00 ± 0.02	0.14 ± 0.04
10.56	11.71 ± 0.41	0.99 ± 0.02	2.36 ± 0.72
11.81	3.19 ± 0.80	0.98 ± 0.02	0.65 ± 0.26
12.63	5.82 ± 0.81	0.97 ± 0.02	1.20 ± 0.40
13.49	6.22 ± 0.40	0.96 ± 0.03	1.29 ± 0.40
14.58	5.38 ± 0.49	0.95 ± 0.03	1.13 ± 0.36
15.82	5.12 ± 0.55	0.94 ± 0.03	1.09 ± 0.35
16.74	2.81 ± 0.36	0.92 ± 0.03	0.61 ± 0.20
17.75	3.54 ± 0.44	0.91 ± 0.03	0.78 ± 0.26

^{59}Co$(p,n)^{59}$Ni		$E_p = 200$ MeV	$\theta = 0°$
E_x	$\sigma(q,\omega)$	$F(q,\omega)$	B(GT)
7.18	1.76 ± 0.09	1.02 ± 0.01	0.00 ± 0.00
0.34	0.06 ± 0.01	1.01 ± 0.00	0.01 ± 0.00
1.60	0.17 ± 0.01	1.01 ± 0.01	0.03 ± 0.01
2.58	0.04 ± 0.01	1.02 ± 0.01	0.01 ± 0.00
3.17	0.09 ± 0.02	1.02 ± 0.01	0.02 ± 0.01
3.52	0.32 ± 0.03	1.02 ± 0.01	0.06 ± 0.02
4.07	1.27 ± 0.07	1.02 ± 0.01	0.25 ± 0.08
4.41	0.30 ± 0.06	1.02 ± 0.01	0.06 ± 0.02
4.71	0.41 ± 0.05	1.02 ± 0.01	0.08 ± 0.03
5.08	0.47 ± 0.05	1.02 ± 0.01	0.09 ± 0.03
5.58	1.76 ± 0.09	1.02 ± 0.01	0.35 ± 0.11
5.96	0.90 ± 0.08	1.01 ± 0.01	0.18 ± 0.06
6.30	1.03 ± 0.09	1.01 ± 0.01	0.20 ± 0.06
6.69	0.64 ± 0.15	1.01 ± 0.01	0.13 ± 0.05
7.07	0.88 ± 0.11	1.01 ± 0.01	0.17 ± 0.06
7.64	0.57 ± 0.16	1.01 ± 0.02	0.11 ± 0.05
8.20	3.19 ± 0.15	1.00 ± 0.02	0.64 ± 0.19
9.37	0.56 ± 0.06	1.00 ± 0.02	0.11 ± 0.04
10.56	11.01 ± 0.47	0.99 ± 0.02	2.22 ± 0.68
11.81	2.54 ± 0.62	0.98 ± 0.02	0.52 ± 0.20
12.63	6.80 ± 1.39	0.97 ± 0.02	1.40 ± 0.51
13.49	6.79 ± 1.17	0.96 ± 0.03	1.41 ± 0.49
14.58	6.69 ± 1.03	0.95 ± 0.03	1.41 ± 0.48
15.82	2.93 ± 0.70	0.93 ± 0.03	0.63 ± 0.24
16.74	1.94 ± 0.50	0.92 ± 0.03	0.42 ± 0.17
17.75	3.52 ± 0.84	0.91 ± 0.03	0.78 ± 0.30

A.5 ^{59}Co(p,n)^{59}Ni assuming $f_{GT} = 0$

^{59}Co(p,n)^{59}Ni	$E_p = 90$ MeV	$\theta = 0°$	
E_x	$\sigma(q,\omega)$	$F(q,\omega)$	B(GT)
7.18	4.49 ± 0.23	0.94 ± 0.01	0.00 ± 0.02
0.34	0.04 ± 0.00	1.00 ± 0.00	0.02 ± 0.00
1.60	0.07 ± 0.01	0.99 ± 0.01	0.03 ± 0.00
2.58	0.02 ± 0.00	0.99 ± 0.01	0.01 ± 0.00
3.17	0.04 ± 0.01	0.98 ± 0.01	0.02 ± 0.00
3.52	0.12 ± 0.01	0.98 ± 0.01	0.05 ± 0.01
4.07	0.47 ± 0.03	0.97 ± 0.01	0.20 ± 0.02
4.41	0.22 ± 0.02	0.96 ± 0.01	0.09 ± 0.01
4.71	0.17 ± 0.01	0.96 ± 0.01	0.07 ± 0.01
5.08	0.10 ± 0.01	0.95 ± 0.01	0.04 ± 0.01
5.58	0.77 ± 0.04	0.95 ± 0.01	0.32 ± 0.03
5.96	0.47 ± 0.03	0.94 ± 0.01	0.20 ± 0.02
6.30	0.47 ± 0.03	0.93 ± 0.01	0.19 ± 0.02
6.69	0.29 ± 0.02	0.92 ± 0.01	0.12 ± 0.01
7.07	0.35 ± 0.04	0.91 ± 0.01	0.14 ± 0.02
7.64	0.21 ± 0.03	0.91 ± 0.01	0.09 ± 0.01
8.20	0.83 ± 0.06	0.89 ± 0.01	0.33 ± 0.03
9.37	2.35 ± 0.24	0.86 ± 0.02	0.89 ± 0.10
10.56	3.02 ± 0.35	0.82 ± 0.02	1.09 ± 0.14
11.81	0.98 ± 0.19	0.79 ± 0.02	0.34 ± 0.07
12.63	0.79 ± 0.10	0.77 ± 0.02	0.27 ± 0.04
13.49	2.52 ± 0.21	0.74 ± 0.02	0.83 ± 0.09
14.58	2.82 ± 0.21	0.69 ± 0.02	0.87 ± 0.09
15.82	0.57 ± 0.13	0.65 ± 0.02	0.17 ± 0.04
16.74	0.53 ± 0.16	0.62 ± 0.02	0.14 ± 0.04
17.75	0.67 ± 0.12	0.59 ± 0.02	0.17 ± 0.03

^{59}Co(p,n)^{59}Ni	$E_p = 120$ MeV	$\theta = 0°$	
E_x	$\sigma(q,\omega)$	$F(q,\omega)$	B(GT)
7.18	3.67 ± 0.17	0.98 ± 0.01	0.00 ± 0.01
0.34	0.05 ± 0.00	1.00 ± 0.00	0.01 ± 0.00
1.60	0.13 ± 0.01	1.00 ± 0.01	0.04 ± 0.00
2.58	0.03 ± 0.00	1.00 ± 0.01	0.01 ± 0.00
3.17	0.07 ± 0.01	1.00 ± 0.01	0.02 ± 0.00
3.52	0.15 ± 0.01	0.99 ± 0.01	0.04 ± 0.00
4.07	0.74 ± 0.04	0.99 ± 0.01	0.22 ± 0.02
4.41	0.48 ± 0.03	0.99 ± 0.01	0.14 ± 0.01
4.71	0.23 ± 0.02	0.98 ± 0.01	0.07 ± 0.01
5.08	0.22 ± 0.01	0.98 ± 0.01	0.06 ± 0.01
5.58	1.02 ± 0.05	0.98 ± 0.01	0.29 ± 0.02
5.96	0.72 ± 0.04	0.97 ± 0.01	0.21 ± 0.02
6.30	0.77 ± 0.04	0.97 ± 0.01	0.22 ± 0.02
6.69	0.52 ± 0.03	0.96 ± 0.01	0.15 ± 0.01
7.07	0.28 ± 0.03	0.96 ± 0.01	0.08 ± 0.01
7.64	0.68 ± 0.07	0.95 ± 0.01	0.19 ± 0.02
8.20	1.12 ± 0.10	0.94 ± 0.02	0.31 ± 0.03
9.37	5.06 ± 0.28	0.92 ± 0.02	1.36 ± 0.11
10.56	3.82 ± 0.28	0.89 ± 0.02	1.00 ± 0.09
11.81	0.43 ± 0.12	0.87 ± 0.02	0.11 ± 0.03
12.63	4.40 ± 0.35	0.86 ± 0.02	1.11 ± 0.11
13.49	2.41 ± 0.48	0.83 ± 0.02	0.59 ± 0.12
14.58	3.90 ± 0.66	0.80 ± 0.02	0.92 ± 0.17
15.82	2.16 ± 0.47	0.76 ± 0.03	0.49 ± 0.11
16.74	0.30 ± 0.17	0.74 ± 0.03	0.07 ± 0.04
17.75	0.86 ± 0.06	0.72 ± 0.03	0.18 ± 0.02

^{59}Co(p,n)^{59}Ni	$E_p = 160$ MeV	$\theta = 0°$	
E_x	$\sigma(q,\omega)$	$F(q,\omega)$	B(GT)
7.18	2.96 ± 0.11	1.00 ± 0.01	0.00 ± 0.00
0.34	0.06 ± 0.00	1.01 ± 0.00	0.01 ± 0.00
1.60	0.19 ± 0.01	1.01 ± 0.01	0.04 ± 0.00
2.58	0.07 ± 0.00	1.01 ± 0.01	0.01 ± 0.00
3.17	0.09 ± 0.01	1.01 ± 0.01	0.02 ± 0.00
3.52	0.13 ± 0.01	1.01 ± 0.01	0.03 ± 0.00
4.07	1.16 ± 0.05	1.01 ± 0.01	0.23 ± 0.02
4.41	0.48 ± 0.04	1.01 ± 0.01	0.10 ± 0.01
4.71	0.17 ± 0.07	1.00 ± 0.01	0.03 ± 0.01
5.08	0.37 ± 0.02	1.00 ± 0.01	0.08 ± 0.01
5.58	1.70 ± 0.07	1.00 ± 0.01	0.34 ± 0.02
5.96	1.13 ± 0.05	1.00 ± 0.01	0.23 ± 0.01
6.30	0.95 ± 0.04	1.00 ± 0.01	0.19 ± 0.01
6.69	0.58 ± 0.03	0.99 ± 0.01	0.12 ± 0.01
7.07	0.04 ± 0.03	0.99 ± 0.01	0.01 ± 0.01
7.64	0.17 ± 0.02	0.99 ± 0.01	0.03 ± 0.01
8.20	1.98 ± 0.08	0.98 ± 0.02	0.39 ± 0.03
9.37	1.29 ± 0.22	0.97 ± 0.02	0.25 ± 0.04
10.56	11.60 ± 0.65	0.95 ± 0.02	2.23 ± 0.17
11.81	0.91 ± 0.09	0.94 ± 0.02	0.17 ± 0.02
12.63	9.02 ± 0.59	0.92 ± 0.02	1.68 ± 0.14
13.49	0.32 ± 0.10	0.91 ± 0.02	0.06 ± 0.02
14.58	6.03 ± 0.35	0.89 ± 0.03	1.08 ± 0.09
15.82	1.37 ± 0.12	0.87 ± 0.03	0.24 ± 0.03
16.74	2.65 ± 0.11	0.85 ± 0.03	0.46 ± 0.03
17.75	1.06 ± 0.05	0.83 ± 0.03	0.18 ± 0.01

^{59}Co(p,n)^{59}Ni	$E_p = 200$ MeV	$\theta = 0°$	
E_x	$\sigma(q,\omega)$	$F(q,\omega)$	B(GT)
7.18	1.87 ± 0.08	1.02 ± 0.01	0.00 ± 0.00
0.34	0.07 ± 0.00	1.01 ± 0.00	0.01 ± 0.00
1.60	0.18 ± 0.01	1.01 ± 0.01	0.04 ± 0.00
2.58	0.08 ± 0.01	1.02 ± 0.01	0.02 ± 0.00
3.17	0.09 ± 0.01	1.02 ± 0.01	0.02 ± 0.00
3.52	0.35 ± 0.02	1.02 ± 0.01	0.07 ± 0.01
4.07	1.08 ± 0.05	1.02 ± 0.01	0.22 ± 0.02
4.41	0.47 ± 0.04	1.02 ± 0.01	0.10 ± 0.01
4.71	0.34 ± 0.03	1.02 ± 0.01	0.07 ± 0.01
5.08	0.57 ± 0.03	1.02 ± 0.01	0.12 ± 0.01
5.58	1.61 ± 0.06	1.01 ± 0.01	0.33 ± 0.02
5.96	0.94 ± 0.05	1.01 ± 0.01	0.19 ± 0.02
6.30	0.95 ± 0.05	1.01 ± 0.01	0.20 ± 0.02
6.69	1.00 ± 0.06	1.01 ± 0.01	0.21 ± 0.02
7.07	0.89 ± 0.07	1.01 ± 0.01	0.18 ± 0.02
7.64	0.40 ± 0.09	1.01 ± 0.02	0.08 ± 0.02
8.20	3.22 ± 0.12	1.00 ± 0.02	0.66 ± 0.05
9.37	0.71 ± 0.04	1.00 ± 0.02	0.14 ± 0.01
10.56	11.71 ± 0.41	0.99 ± 0.02	2.36 ± 0.17
11.81	3.19 ± 0.80	0.98 ± 0.02	0.64 ± 0.16
12.63	5.82 ± 0.81	0.97 ± 0.02	1.15 ± 0.18
13.49	6.22 ± 0.40	0.96 ± 0.03	1.22 ± 0.11
14.58	5.38 ± 0.49	0.95 ± 0.03	1.04 ± 0.12
15.82	5.12 ± 0.55	0.94 ± 0.03	0.97 ± 0.13
16.74	2.81 ± 0.36	0.92 ± 0.03	0.53 ± 0.08
17.75	3.54 ± 0.44	0.91 ± 0.03	0.65 ± 0.09

^{59}Co$(p,n)^{59}$Ni	$E_p = 200$ MeV	$\theta = 0°$	
E_x	$\sigma(q,\omega)$	$F(q,\omega)$	B(GT)
7.18	1.76 ± 0.09	1.02 ± 0.01	0.00 ± 0.00
0.34	0.06 ± 0.01	1.01 ± 0.00	0.01 ± 0.00
1.60	0.17 ± 0.01	1.01 ± 0.01	0.04 ± 0.00
2.58	0.04 ± 0.01	1.02 ± 0.01	0.01 ± 0.00
3.17	0.09 ± 0.02	1.02 ± 0.01	0.02 ± 0.00
3.52	0.32 ± 0.03	1.02 ± 0.01	0.07 ± 0.01
4.07	1.27 ± 0.07	1.02 ± 0.01	0.27 ± 0.03
4.41	0.30 ± 0.06	1.02 ± 0.01	0.07 ± 0.01
4.71	0.41 ± 0.05	1.02 ± 0.01	0.09 ± 0.01
5.08	0.47 ± 0.05	1.02 ± 0.01	0.10 ± 0.01
5.58	1.76 ± 0.09	1.02 ± 0.01	0.38 ± 0.03
5.96	0.90 ± 0.08	1.01 ± 0.01	0.19 ± 0.02
6.30	1.03 ± 0.09	1.01 ± 0.01	0.22 ± 0.03
6.69	0.64 ± 0.15	1.01 ± 0.01	0.14 ± 0.03
7.07	0.88 ± 0.11	1.01 ± 0.01	0.19 ± 0.03
7.64	0.57 ± 0.16	1.01 ± 0.02	0.12 ± 0.04
8.20	3.19 ± 0.15	1.00 ± 0.02	0.68 ± 0.06
9.37	0.56 ± 0.06	1.00 ± 0.02	0.12 ± 0.02
10.56	11.01 ± 0.47	0.99 ± 0.02	2.32 ± 0.20
11.81	2.54 ± 0.62	0.98 ± 0.02	0.53 ± 0.14
12.63	6.80 ± 1.39	0.97 ± 0.02	1.40 ± 0.30
13.49	6.79 ± 1.17	0.96 ± 0.03	1.39 ± 0.26
14.58	6.69 ± 1.03	0.95 ± 0.03	1.35 ± 0.23
15.82	2.93 ± 0.70	0.93 ± 0.03	0.58 ± 0.15
16.74	1.94 ± 0.50	0.92 ± 0.03	0.38 ± 0.10
17.75	3.52 ± 0.84	0.91 ± 0.03	0.68 ± 0.17

Bibliography

[1] A. deShalit, H. Feshbach, *Theoretical Nuclear Physics, Vol. 1* (Wiley, New York, 1974)

[2] C. D. Goodman, Prog. in Part. and Nucl. Phys. **11** (1983) 475

[3] B. A. Brown, B. H. Wildenthal, At. Data Nucl. Data Tables **33** (1985) 347

[4] C. D. Goodman, S. D. Bloom, In *Spin Excitations in Nuclei*, Edited by F. Petrovich, G. E. Brown, G. T. Garvey, C. D. Goodman, R. A. Lindgren, W. G. Love (Plenum Press, New York, 1984) p. 143

[5] C. D. Goodman, In *The (p,n) Reaction and the Nucleon-Nucleon Force*, Edited by C. D. Goodman, S. M. Austin, S. D. Bloom, J. Rapaport, G. R. Satchler (Plenum Press, New York, 1980) p. 149

[6] T. N. Taddeucci, C. A. Goulding, T. A. Carey, R. C. Byrd, C. D. Goodman, C. Gaarde, J. Larsen, D. J. Horen, J. Rapaport, E. Sugarbaker, Nucl. Phys. **A469** (1987) 125

[7] C. D. Zafiratos, In *The (p,n) Reaction and the Nucleon-Nucleon Force*, Edited by C. D. Goodman, S. M. Austin, S. D. Bloom, J. Rapaport, G. R. Satchler (Plenum Press, New York, 1980) p. 313

[8] K. Ikeda, S. Fujii, J. I. Fujita, Phys. Lett. **3** (1963) 271

[9] F. Osterfeld, Rev. Mod. Phys. **64** (1992) 491

[10] C. D. Goodman, Can. J. Phys. **65** (1987) 549

[11] G. F. Bertsch, H. Esbensen, Rep. Prog. Phys. **50** (1987) 607

[12] J. Rapaport, Can. J. Phys. **65** (1987) 574

[13] J. D. Anderson, C. Wong, J. W. McClure, Phys. Rev. **126** (1962) 2170

[14] J. D. Anderson, C. Wong, Phys. Rev. Lett. **7** (1961) 250

[15] A. Langsford, P. H. Bowen, G. C. Cox, M. J. M. Saltmarsh, Nucl. Phys. **A113** (1968) 433

[16] R. K. Jolly, T. M. Amos, A. Galonsky, R. Hinrichs, R. St. Onge, Phys. Rev. C **7** (1973) 1903

[17] J. Rapaport, R. Alarcon, B. A. Brown, C. Gaarde, J. Larsen, C. D. Goodman, C. C. Foster, D. Horen, T. Masterson, E. Sugarbaker, T. N. Taddeucci, Nucl. Phys. **A427** (1984) 332

[18] Z. Chunmei, Z. Enchen, L. Xiane, Nucl. Data Sheets **48** (1986) 111

[19] Y. Wang, C. Goodman, W. Huang, G. C. Kiang, T. N. Taddeucci, R. C. Byrd, T. A. Carey, B. Sailor, L. J. Rybarcyk, C. A. Gaarde, D. J. Horen, J. Rapaport, E. R. Sugarbaker, D. Marchlenski, J. Wagner, IUCF Sci. and Tech. Report (1989) 48

[20] Y. Wang, C. Goodman, W. Huang, G. C. Kiang, R. C. Byrd, L. J. Rybarcyk, T. N. Taddeucci, J. Rapaport, D. Marchlenski, E. R. Sugarbaker, IUCF Sci. and Tech. Report (1990) 49

[21] W. Huang, Ph.D Thesis, Indiana University (1991)

[22] H. Orihara, T. Murakami, S. Nishihara, T. Nakagawa, K. Maeda, K. Miura, H. Ohnuma, Phys. Rev. Lett. **47** (1981) 301

[23] J. Rapaport, T. Taddeucci, T. P. Welch, C. Gaarde, J. Larsen, D. J. Horen, E. Sugarbaker, P. Koncz, C. C. Foster, C. D. Goodman, C. A. Goulding, T. Masterson, Nucl. Phys. **A410** (1983) 371

[24] M. C. Vetterli, O. Häusser, R. Abegg, W. P. Alford, A. Celler, D. Frekers, R. Helmer, R. Henderson, K. H. Hicks, K. P. Jackson, R. G. Jeppesen, C. A. Miller, K. Raywood, S. Yen, Phys. Rev. C **40** (1989) 559

[25] B. D. Anderson, C. Lebo, A. R. Baldwin, T. Chittrakarn, R. Madey, J. W. Watson, Phys. Rev. C **41** (1990) 1474

[26] T. N. Taddeucci, J. Rapaport, D. E. Bainum, C. D. Goodman, C. C. Foster, C. Gaarde, J. Larsen, C. A. Goulding, D. J. Horen, T. Masterson, E. Sugarbaker, Phys. Rev. C **25** (1982) 1094

[27] C. D. Goodman, R. C. Byrd, I. J. van Heerden, T. A. Carey, D. J. Horen, J. S. Larsen, C. Gaarde, J. Rapaport, T. P. Welch, E. Sugarbaker, T. N. Taddeucci, Phys. Rev. Lett. **54** (1985) 877

[28] H. Nakada, T. Sebe, J. Phys. G **22** (1996) 1349

[29] T. Rönnqvist, H. Condé, N. Olsson, E. Ramström, R. Zorro, J. Blomgren, A. Håkansson, A. Ringbom, G. Tibell, O. Jonsson, L. Nilsson, P.-U. Renberg, S. Y. van der Werf, W. Unkelbach, F. P. Brady, Nucl. Phys. **A563** (1993) 225

[30] E. Caurier, G. Martínez-Pinedo, A. Poves, A. P. Zuker, Phys. Rev. C **52** (1995) R1736

[31] M. Aufderheide, S. D. Bloom, D. A. Resler, G. J. Mathews, Phys. Rev. C **48** (1993) 1677

[32] Samuel S. M. Wong, *Introductory Nuclear Physics* (Prentice-Hall International, 1990) pp. 216–220

[33] J. Rapaport and E. Sugarbaker, Ann. Rev. Nucl. Part. Sci. (1994) 109

[34] A. Bohr and B. R. Mottelson, *Nuclear Structure* (Benjamin, New York, 1969) I:345,349,411

[35] J. C. Hardy, I. S. Towner, V. T. Koslowsky, E. Hagberg, H. Schmeing, Nucl. Phys. **A509** (1990) 429

[36] D. Dubbers, Nucl. Phys. **A527** (1991) 239c

[37] G. R. Satchler, *Direct Nuclear Reactions* (Oxford University Press, New York, 1983)

[38] N. K. Glendenning, *Direct Nuclear Reactions* (Academic Press, London, 1983) pp. 175–222

[39] A. K. Kerman, H. McManus, R. M. Thaler, Ann. Phys. **8** (1959) 551

[40] W. G. Love, M. A. Franey, Phys. Rev. C **24** (1981) 1073

[41] M. A. Franey, W. G. Love, Phys. Rev. C **31** (1985) 488

[42] R. R. Doering, A. Galonsky, D. M. Patterson, G. F. Bertsch, Phys. Rev. Lett. **35** (1975) 1691

[43] C. D. Goodman, C. A. Goulding, M. B. Greenfield, J. Rapaport, D. E. Bainum, C. C. Foster, W. G. Love, F. Petrovich, Phys. Rev. Lett. **44** (1980) 1755

[44] Program DWBA70, R. Schaeffer and J. Raynal (unpublished); extended version DW81 by J. R. Comfort (unpublished)

[45] C. D. Goodman, private communication; data being prepared for publication.

[46] B. D. Anderson, T. Chittrakarn, A. R. Baldwin, C. Lebo, R. Madey, R. J. McCarthy, J. W. Watson, B. A. Brown, C. C. Foster, Phys. Rev. C **31** (1985) 1147

[47] H. V. Klapdor, Prog. Part. Nucl. Phys. **10** (1983) 131

[48] B. D. Anderson, T. Chittrakarn, A. R. Baldwin, C. Lebo, R. Madey, P. C. Tandy, J. W. Watson, C. C. Foster, B. A. Brown, B. H. Wildenthal, Phys. Rev. C **36** (1987) 2195

[49] B. D. Anderson, N. Tamimi, A. R. Baldwin, M. Elaasar, R. Madey, D. M. Manley, M. Mostajabodda'vati, J. W. Watson, W. M. Zhang, C. C. Foster, Phys. Rev. C **43** (1991) 50

[50] C. D. Goodman, J. Rapaport, S. D. Bloom, Phys. Rev. C **42** (1990) 1150

[51] M. C. Vetterli, K. P. Jackson, S. Yen, Phys. Rev. C **42** (1990) 1153

[52] F. Osterfeld, Phys. Rev. C **26** (1982) 762

[53] F. Osterfeld, In *Spin Excitations in Nuclei*, Edited by F. Petrovich, G. E. Brown, G. T. Garvey, C. D. Goodman, R. A. Lindgren, W. G. Love (Plenum Press, New York, 1984) p. 403

[54] G. F. Bertsch, I. Hamamoto, Phys. Rev. C **26** (1982) 1323

[55] C. D. Goodman, C. C. Foster, D. E. Bainum, S. D. Bloom, C. Gaarde, J. Larsen, C. A. Goulding, D. J. Horen, T. Masterson, S. Grimes, J. Rapaport, T. N. Taddeucci, E. Sugarbaker, Phys. Lett. **107B** (1981) 406

[56] L. W. Alvarez, Phys. Rev. **54** (1938) 609

[57] R. T. Kabutz, M.Sc Thesis, University of Cape Town (1992)

[58] XSYS Data Acquisition and Analysis Program, Originally developed at Triangle Universities Nuclear Laboratory (TUNL) and extensively modified at the Indiana University Cyclotron Facility (IUCF)

[59] R. T. Newman, M.Sc Thesis, University of Cape Town (1991)

[60] J. W. Watson, R. Pourang, R. Abegg, W. P. Alford, A. Celler, S. El-Kateb, D. Frekers, O. Hausser, R. Helmer, R. Henderson, K. Hicks, K. P. Jackson, R. G. Jeppesen, C. A. Miller, M. Vetterli, S. Yen, C. D. Zafiratos, Phys. Rev. C **40** (1989) 22

[61] J. Rapaport, C. D. Goodman, E. R. Sugarbaker, private communications.

[62] R. A. Cecil, B. D. Anderson, R. Madey, Nucl. Instr. and Meth. **161** (1979) 439

[63] V. McLane, C. L. Dunford, P. F. Rose, *Neutron Cross Sections, Vol. 2* (Academic Press, San Diego, 1988)

[64] Z. Chunmei, Nucl. Data Sheets **63** (1991) 229

[65] W. P. Alford, B. A. Brown, S. Burzynski, A. Celler, D. Frekers, R. Helmer, R. Henderson, K. P. Jackson, K. Lee, A. Rahav, A. Trudel, M. C. Vetterli, Phys. Rev. C **48** (1993) 2818

[66] H. Junde, S. Huibin, Z. Weizhong, Z. Qing, Nucl. Data Sheets **68** (1993) 887

[67] G. Wang, J. Zhu, J. Zhang, Nucl. Data Sheets **50** (1987) 255

[68] B. D. Anderson, T. Chittrakarn, A. R. Baldwin, C. Lebo, R. Madey, P. C. Tandy, J. W. Watson, B. A. Brown, C. C. Foster, Phys. Rev. C **31** (1985) 1161

[69] P. J. Bester, M.Sc Thesis, University of the Western Cape (1992)

[70] C. M. Baglin, Nucl. Data Sheets **69** (1993) 733

[71] T. N. Taddeucci, T. A. Carey, C. Gaarde, J. Larsen, C. D. Goodman, D. J. Horen, T. Masterson, J. Rapaport, T. P. Welch, E. Sugarbaker, Phys. Rev. Lett. **52** (1984) 1960

[72] W. D. Cornelius, J. M. Moss, T. Yamaya, Phys. Rev. C **23** (1981) 1364

[73] J. M. Moss, Phys. Rev. C **26** (1982) 727

[74] E. Sugarbaker, D. Marchlenski, T. N. Taddeucci, L. J. Rybarcyk, J. B. McClelland, T. A. Carey, R. C. Byrd, C. D. Goodman, W. Huang, J. Rapaport, D. Mercer, D. Prout, W. P. Alford, E. Gülmez, A. A. Witten, D. Ciskowski, Phys. Rev. Lett. **65** (1990) 551